Universitat Politècnica de Catalunya

Programa de Doctorat de Matemàtica Aplicada

Departament d'Enginyeria Civil i Ambiental

The variational approach to brittle fracture in materials with anisotropic surface energy and in thin sheets

by Bin Li

Doctoral Thesis

Advisors: Marino Arroyo and Irene Arias

Barcelona, January 2016

<div align="center">

ABSTRACT

</div>

<div align="center">

The variational approach to brittle fracture in materials with anisotropic surface energy and in thin sheets

Bin Li

</div>

Fracture mechanics of brittle materials has focused on bulk materials with isotropic surface energy. In this situation different physical principles for crack path selection are very similar or even equivalent. The situation is radically different when considering crack propagation in brittle materials with anisotropic surface energy. Such materials are important in applications involving single crystals, extruded polymers, or geological and organic materials. When this anisotropy is strong, the phenomenology of crack propagation becomes very rich, with forbidden crack propagation directions or complex sawtooth crack patterns. Thus, this situation interrogates fundamental issues in fracture mechanics, including the principles behind the selection of crack direction. Similarly, tearing of brittle thin elastic sheets, ubiquitous in nature, technology and daily life, challenges our understanding of fracture. Since tearing typically involves large geometric nonlinearity, it is not clear whether the stress intensity factors are meaningful or if and how they determine crack propagation. Geometry, together with the interplay between stretching and bending deformation, leads to complex behaviors, restricting analytical approximate solutions to very simplified settings and specific parameter regimes.

In both situations, a rich and nontrivial experimental record has been successfully understood in terms of simple energetic models. However, general modeling approaches to either fracture in the presence of strong surface energy anisotropy or to tearing, capable of exploring new physics, have been lacking. The success of energetic simple models suggests that variational theories of brittle fracture may provide a unifying and general framework capable of dealing with the more general situations considered here.

To address fracture in materials with strongly anisotropic surface energy, we pro-

<div align="center">

iii

</div>

pose a variational phase-field model resorting to the extended Cahn-Hilliard framework, originally proposed in the context of crystal growth. Previous phase-field models for anisotropic fracture were formulated in a framework restricted to weak anisotropy. We implement numerically our higher-order phase-field model with smooth local maximum entropy approximants in a direct Galerkin method. The numerical results exhibit all the features of strongly anisotropic fracture, and reproduce strikingly well recent experimental observations. To explore tearing of thin films, we develop a geometrically exact model and a computational framework coupling elasticity (stretching and bending), fracture, and adhesion to a substrate. We numerically implement the model with subdivision surface finite elements. Our simulations qualitatively and quantitatively reproduced the crack patterns observed in tearing experiments.

Finally, we examine how shell geometry affects fracture. As suggested by previous results and our own phase-field simulations, shell shape dramatically affects crack evolution and the effective toughness of the shell structure. To gain insight and eventually develop new concepts for optimizing the design of thin shell structures, we derive the configurational force conjugate to crack extension for Koiter's linear thin shell theory. We identify the conservative contribution to this force through an Eshelby tensor, as well as non-conservative contributions arising from curvature.

Acknowledgments

I would like to acknowledge the help, support and guidance of my thesis advisors, Professor Marino Arroyo and Professor Irene Arias, with the most sincere gratitude. They offered me the freedom to work on the research subject I like and explore it, always encouraged me to keep trying when I wanted to give up. I could not have imagined having a better advisors and mentors.

I am very grateful to my officemates in the group of Laboratori de Càlcul Numèric (LaCàN): Dr. Amir Abdollahi, Dr. Daniel Millán, Dr. Christian Peco, Dr. Mohammad Rahimi, Dr. Juan Vanegas, Dr. Kuan Zhang, Fatemeh Amiri, Ceren Gürkan, Raquel García, Raúl Hospital, Omid Javadzadeh, Albert Oliver, Flaviu Simon, Alejandro Torres-Sánchez, Aditya Vasudevan, for the help and support in all the time of research. I really enjoy the collaboration with Dr. Daniel Milln, Dr. Christian Peco and Alejandro Torres-Sánchez, and will never forget the helpful and valuable advices of Daniel Millán, the never-ending funny conversations with Dr. Kuan Zhang and the sense of humor of Alejandro Torres-Sánchez.

I am indebted to my parents, my brother and my loving wife,Yue Lang, for their always unconditional support and encouragement. Their love has provided me with the enthusiasm to rise to the challenges and conquer them.

I acknowledge indispensable assistance of administrative staff of LaCàN, Imma Rius and Susanna Algarra, faculty of mathematics and statistics, Raquel Caparrs and Carme Capdevilla and staff of International and Corporate Relations Bureau of UPC, Anna Maria Fabregas. I also wish to acknowledge the IT support of David Ortin and David Prat. Finally, I want to thank the finance support from the Joint China Scholarship Council (CSC)-Universitat Politècnica de Catalunya (UPC) Scholarship.

Contents

List of Figures

Chapter 1

Introduction and Overview

1.1 Classical brittle fracture mechanics

A material is called brittle if it remains linear elastic up to the initiation of fracture. If the characteristic linear dimension of the region around the crack front where the material undergoes inelastic deformation is much smaller than the crack length or some other characteristic dimension of the specimen, the so called small-scale yielding assumption (Dugdale, 1960), the material is called quasi-brittle. Classical brittle fracture mechanics is concerned with the study of the growth of pre-existing cracks in brittle and quasi-brittle materials (Cherepanov, 1979).

Towards understanding the conditions under which cracks will propagate and how they will propagate, a major goal of classical brittle fracture mechanics is to determine the local stress and deformation fields in the vicinity of the crack tip. In the case of two dimensional problems (anti-plane shear, plain strain and plane stress), it is possible to derive closed-form expressions for the stresses in a cracked body, under the assumption of homogeneous linear elastic material behaviour and infinitesimal strain. The asymptotic stress distribution around a quasi-static crack tip, in polar coordinates (r, θ) with origin at the crack tip as shown in Figure 1.1, are given by (Anderson, 2005; Zehnder, 2012)
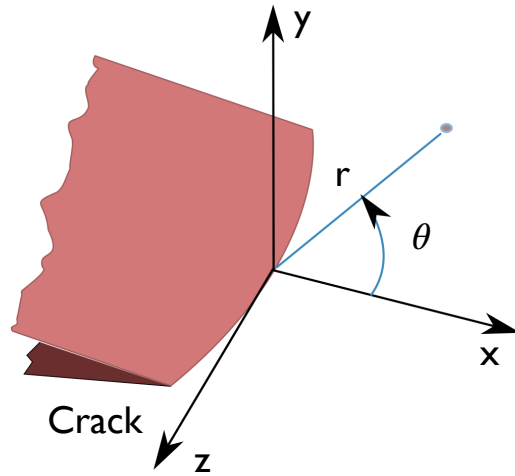
Figure 1.1: Definition of the local frame at any point on the crack front.

Mode I:
Opening

Mode II:
In-plane shear

Mode III:
Out-of-plane shear
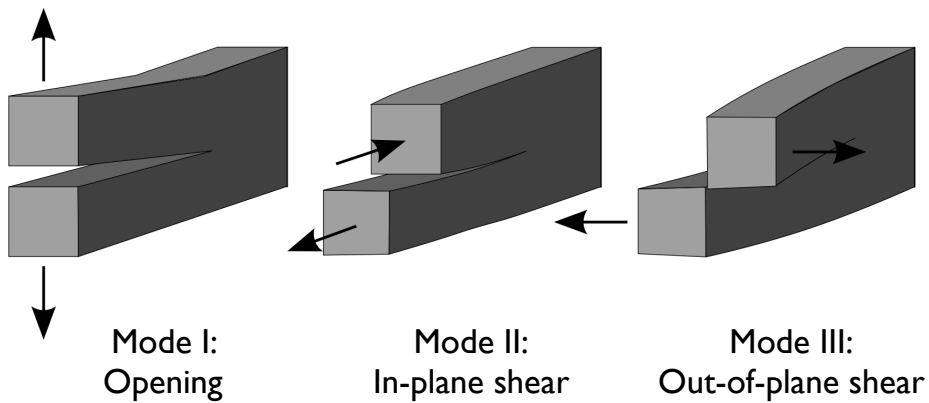
Figure 1.2: Schematic of three modes of loading. Mode I, an opening mode normal to the plane of crack. Mode II, a shear mode acting parallel to the plane of crack and perpendicular to the crack front. Mode III, a shear mode acting parallel to the plane of the crack and parallel to the crack front. The actual crack may experiences mixed Mode-I, II, III loadings and this mixed mode may vary along the crack front.

$$\sigma_{ij}^m(r,\theta) = \frac{K_m}{\sqrt{2\pi r}} f_{ij}^m(\theta) + O(\sqrt{r}), \tag{1.1}$$

where K_m are the stress intensity factors (SIFs) corresponding to the three fundamental modes of loading. See Figure 1.2 for a graphical illustration of K_I, K_{II} and K_{III}. These factors can be formally defined as

$$K_I = \lim_{r\to 0} \sqrt{2\pi r}\sigma_{yy}(r,0),\ K_{II} = \lim_{r\to 0} \sqrt{2\pi r}\sigma_{yx}(r,0),\ K_{III} = \lim_{r\to 0} \sqrt{2\pi r}\sigma_{yz}(r,0), \tag{1.2}$$

and play a central role in the characterization of the energy flux during the fracture process and in the prediction of crack onset and evolution path (Anderson, 2005; Zehnder, 2012). The stress diverges to infinity at the crack tip, regardless of the geometrical configuration of the cracked body.

The analysis of quasi-static crack propagation, in general, consists of two steps. The first step is to decide if the crack will propagate for given loading conditions. In Griffith's (Griffith, 1921) or Irwin's (Irwin, 1957) theory, crack propagation arises as a balance between the surface energy and the release of elastic energy; a crack will propagate in a direction given by the angle θ when the relation

$$G(\theta) = G_c \tag{1.3}$$

holds, where $G(\theta)$ is the elastic energy release rate for a crack along θ and G_c is the surface energy of the newly created crack faces. The second step is to decide in which direction the crack will propagate. Although Griffith's theory has proved to be very useful to describe the various features of cracks (Freund, 1998), it does not address the important question of how to determine the crack path, that is the angle θ. For this a number of crack path selection criteria have been proposed, including (1) the maximum hoop stress (MHS) criterion (Erdogan and Sih, 1963), (2) the principle of local symmetry (PLS) criterion (Cotterell, 1965; Goldstein and Salganik, 1974), (3) the minimum strain energy density (MSED) criterion (Sih, 1974), or (4) maximum energy release rate (MERR) criterion (Wu, 1978; Palaniswamy and Knauss, 1978).

The MHS criterion (Erdogan and Sih, 1963) postulates that a crack will grow in the direction for which the hoop stress $\sigma_{\theta\theta}$ is maximum. In the PLS criterion (Cotterell, 1965; Goldstein and Salganik, 1974), the crack advances in the direction such that the $K_{II} = 0$ at new crack tip. This implies that the crack only propagates in a pure opening mode with a symmetrical stress distribution about its local coordinate axis. The MSED criterion (Sih, 1974) states that the crack will grow in the direction for which the strain energy density factor $S = rU$ around the crack tip is minimum, where r is the distance to the crack tip and U is the strain energy density. The MERR criterion (Wu, 1978; Palaniswamy and Knauss, 1978) dictates the crack propagates along the direction that maximizes the energy release rate $G = -\partial\Pi/\partial A$, where Π is the potential of the system and A is the area of the crack surface (crack length for two-dimensional problems). For isotropic and homogeneous materials under in-plane load, all these criterion are capable of predicting the crack path with good accuracy and in general, predict very similar crack paths (Kuna, 2013); in fact, PLS and MERR are identical under certain conditions (Amestoy and Leblond, 1992; Chambolle et al., 2009; Hakim and Karma, 2009)). In addition to these criteria, the configurational forces approach has also been applied to crack propagation (Cherepanov, 1979; Gurtin and Podio-Guidugli, 1996; Gurtin, 2000). It postulates that the crack will advance in the direction of the configurational force vector $\boldsymbol{J}$. This criterion predicts results very close to the MEER criterion if $K_{II}/K_I \leqslant 1$, but significantly deviates from this criterion and from experimental observations when $K_{II}/K_I > 1$, i.e., for large transverse shear load (Cherepanov, 1979; Kuna, 2013).

1.2 Challenges of classical brittle fracture mechanics and goal of this thesis

The above two-step analysis procedure for quasi-static crack propagation has been successfully applied to understand and predict crack propagation in brittle and quasi-brittle materials with isotropic surface energy under in-plane load (mode I, mode II

and mixed-mode I+II). However, there are significant and fundamental challenges in dealing with brittle fracture in materials with anisotropic surface energy, thin sheets under out-of-plane loading and three dimensional curved crack propagation. As argued below, these more general situations oblige us to reconsider our physical understanding of brittle fracture, particularly with regards to the path selection criterion. These more general situations provide an opportunity to discriminate between the different crack path criteria, which no longer produce nearly identical results or are not even applicable.

Let us focus first on materials with anisotropic surface energy. For the sake of discussion, suppose that the material under consideration is elastically isotropic. Its is physically clear that the existence of surface orientations with lower surface energy will bias the direction of crack propagation. However, a stress-based criterion such as that based on the maximum hoop stress is not capable of detecting this fact since our material is elastically isotropic; therefore, this criterion is not physically reasonable in this setting. Some pioneering works have examined the problem of crack path selection in materials with anisotropic surface energy. The maximum energy release rate criterion had been generalized to materials with orientation dependent surface energy $G_c(\theta)$ (Palaniswamy and Knauss, 1978; Gurtin and Podio-Guidugli, 1998; Gurtin, 2000; Chambolle et al., 2009), by noticing that the Griffith's criterion is first met along a direction θ such that $G(\theta)/G_c(\theta)$ is maximized. If these functions are smooth, the optimality necessary condition results in $dG/d\theta = dG_c/d\theta$, which can be identified as a configurational torque balance (Hakim and Karma, 2005, 2009). In addition, the PLS criterion has also been extended to materials with anisotropic surface energy recently (Hakim and Karma, 2005, 2009), but not yet widely accepted. For two-dimensional smooth crack propagation, the two criteria coincide, yet, they predict very different crack direction for non-smooth cracks (Hakim and Karma, 2005, 2009). Recent experiments (Takei et al., 2013) on thin anisotropic films have interrogated the variational principle for path selection based on maximization of $G(\theta)/G_c(\theta)$, suggesting that crack path is governed by its local maximization. When the surface energy of the materials is isotropic, the symmetry of loading dictates that the crack

5
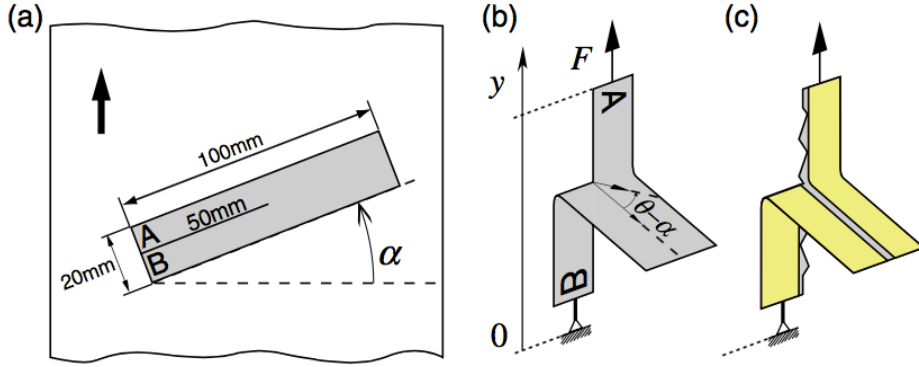
Figure 1.3: Tearing of thin anisotropic sheets experiments (Takei et al., 2013). When the anisotropy is strong, the phenomenology of crack propagation becomes very rich, with forbidden crack propagation directions or complex sawtooth crack patterns.

propagation will be in the direction of tearing $\theta = \alpha$, see the Figure 1.3. In the case of the anisotropic surface energy, this symmetry is broken. For a material with weak anisotropy, small deviations $\theta - \alpha$ are observed in the experiments. When this anisotropy is strong, the phenomenology of crack propagation becomes very rich, with forbidden crack propagation directions or complex sawtooth crack patterns, see the Figure 1.3.

For thin plates (Williams, 1961; Sih et al., 1962; Zehnder and Viz, 2005) or shells (Folias, 1977) under the Kirchhoff assumption, in addition to the usual in-plane stress intensity factors K_I and K_{II}, there are two other stress intensity factors k_1 and k_2, which correspond to a symmetric bending mode and antisymmetric twisting and shearing mode. The inherent kinematic assumption of Kirchhoff plate theory results in $r^{-3/2}$ singularity rather than $r^{-1/2}$ in the out-of-plane shear stresses, which can be rectified using Reissner plate theory (Hui and Zehnder, 1993). These effects only matters around the crack tip in a region in the order of the plate thickness. However, large geometric non-linearities are often involved in the tearing thin sheets (Hamm et al., 2008; Bayart et al., 2010, 2011; Kruglova et al., 2011; Romero et al., 2013; Takei et al., 2013), see the Figure 1.3 and Figure 1.4, and it is not fully clear whether the near crack tip fields still have the same universal divergent forms as in the linear plate or shell theory analysis (Hui et al., 1998). In this case, whether the crack path

(a)

(b)

(c)

(d)
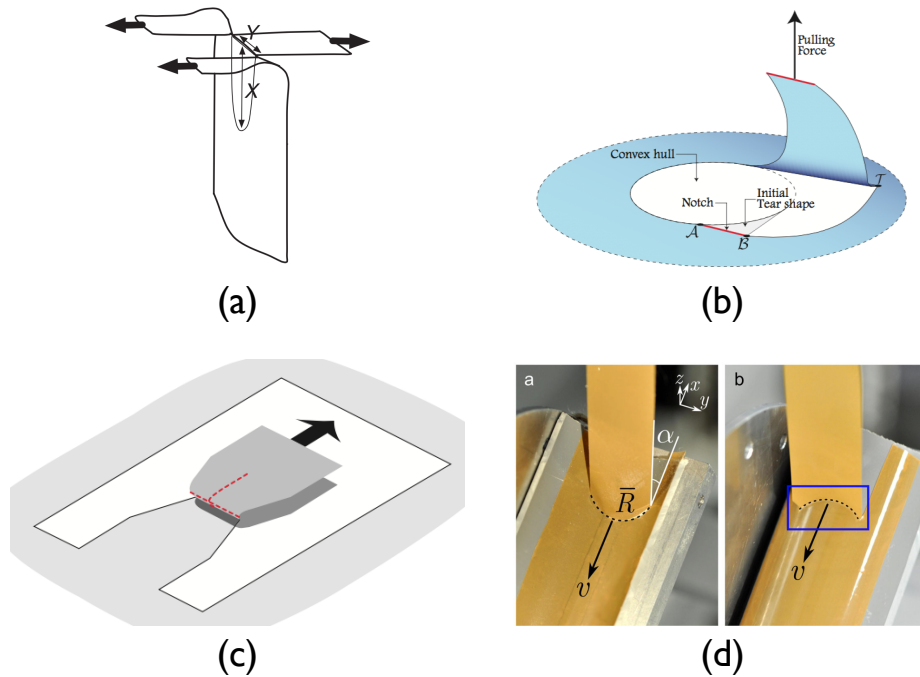
Figure 1.4: Fracture of brittle thin sheets by tearing with or without adhesion to substrates. (a) three flaps experimental configuration (Bayart et al., 2011); (b) spiral tearing experimental configuration (Romero et al., 2013); (c) thin sheet adhered to flat substrate (Hamm et al., 2008); (d) thin sheet adhered to cylinder substrate (Kruglova et al., 2011).

selection criteria of bulk materials can be generalized or make physical sense is not yet understood.

The goal of this thesis is to examine computationally brittle fracture in two situations where the classical view based on bulk isotropic brittle fracture is challenged: materials with strongly anisotropic surface energy and thin elastic sheets. As illustrated above, there is ample and rich experimental literature on these phenomena. Interestingly, many of these observations have been explained by simplified models based on energy minimization.

Based on this observation, the major hypothesis motivating this thesis is that a variational/energetic theory of brittle fracture should be capable of modeling crack propagation in general situations including materials with anisotropic surface energy or thin sheets. To test this hypothesis, we will resort to phase-field models of fracture, reviewed next, which will need to be generalized.

1.3   The variational approach to brittle fracture

Computational approaches to brittle fracture mechanics require criteria to predict the onset of crack extension, the direction of crack propagation and possibly crack branching. Moreover, specialized techniques are necessary to numerically represent and track sharp cracks, such as sophisticated adaptive remeshing schemes that introduce new boundaries when the crack propagates (Ingraffea and Saouma, 1985; Rangarajan et al., 2015), or local enrichment of the approximation space to account for discontinuities and asymptotic fields in the extended finite element method (Moës et al., 1999). Some of the challenges of sharp interface approaches to fracture with regards to crack nucleation or branching can be addressed by combining them with damage models, see (Tamayo-Mas and Rodríguez-Ferran, 2015) for a recent example, or by efficient diffuse damage models such as the thick level set method (Cazes and Moës, 2015).

In recent years, phase-field models of fracture have emerged as a promising approach to computational fracture mechanics. In these models, the complexity of

tracking and evolving cracks is addressed by introducing an additional field describing cracks in a smeared way, which needs to be solved for using a partial differential equation coupled to the equations of elasticity. These models are founded on the variational approach to brittle fracture proposed by Francfort and Marigo (1998), which formulates the crack initiation and quasi-static evolution in terms of the minimization of a Griffith-like energy functional consisting of the elastic energy and surface energy of a cracked body. This theory was subsequently regularized into a phase-field or gradient damage model suitable for numerical calculations (Bourdin et al., 2000; Bourdin, 2007), and which converges to the sharp variational theory of brittle fracture (Bourdin et al., 2008). Subsequently, Pham et al. (2011); Pham and Marigo (2013) interpreted it as a non-local gradient damage model and proposed a general class of variational gradient damage models that Gamma-converge to Griffith brittle fracture theory (Braides, 1998) and have some advantages from numerical and theoretical standpoints (Pham et al., 2011). These works have prompted further developments extending the original approach to account for fracture in piezoelectric and ferroelectric materials (Abdollahi and Arias, 2012), fracture in rubbery polymers (Miehe and Schänzel, 2014), complex crack patterns induced by thermal shocks (Maurini et al., 2013; Bourdin et al., 2014; Sicsic et al., 2014), thin film fracture and delamination (Mesgarnejad et al., 2013; Baldelli et al., 2013, 2014), pressurized fractures (Wheeler et al., 2014), or fracture in linear thin shells (Amiri et al., 2014). Phase-field models have been formalized into a thermodynamic framework by Miehe et al. (2010a,b).

Independently from the variational approach to brittle fracture based on Griffith's theory, a series of alternative phase-field descriptions of crack growth in brittle materials have been proposed by Aranson et al. (2000); Karma et al. (2001); Eastgate et al. (2002); Marconi and Jagla (2005); Spatschek et al. (2006). Various numerical simulations have demonstrated their ability to reproduce the onset of crack propagation at Griffith's threshold as well as dynamical branching and oscillatory instabilities (Henry and Levine, 2004; Karma and Lobkovsky, 2004), helical crack-front instability in mixed mode I and III fracture (Pons and Karma, 2010) and thermal fracture (Corson et al., 2009). These alternative phase-field models typically involve some form of

viscous dynamics, as in the phase-model developed by Miehe et al. (2010b); Kuhn and Müller (2010), and can only describe the propagation of a preexisting crack (Bourdin et al., 2014).

Hakim and Karma (2005, 2009) have pointed out that in a quasi-static setting the PLS and MERR criteria are embedded in phase-field fracture models. Moreover, simplified theoretical models based on a variational/energetic approach combining Griffith's theory with the MERR criterion have successfully explained crack paths observed in experiments of tearing thin sheets with adhesion (Hamm et al., 2008; Sen et al., 2010), without adhesion (Roman, 2013; Brau, 2014) and in anisotropic thin sheets (Takei et al., 2013). There have been attempts to develop theories that explain tearing in thin sheets including geometric nonlinearity (Cohen and Procaccia, 2010), which have focused on characterizing the stress state in the vicinity of the crack tip and have invoked a generalized the PLS criterion. This reference captures some qualitative features of crack propagation such as convergent cracks in three-flap tearing tests, but fails to describe the power-law geometry of the crack path (Bayart et al., 2010, 2011). These previous results suggest that the variational approach could provide a general description of fracture, applicable in a variety of non-standard crack propagation problems.

1.4   Organization of the thesis

The rest of this thesis is organized as follows. In Chapter 2, we propose a variational phase-field model for anisotropic fracture, which resorts to the extended Cahn-Hilliard framework proposed in the context of crystal growth. We implement numerically our higher-order phase-field model with smooth local maximum entropy approximants in a direct Galerkin method. The numerical results exhibit all the features of strongly anisotropic fracture, and reproduce strikingly well recent experimental observations. In Chapter 3, we develop a variational phase-field model and a computational framework coupling elasticity (stretching and bending), fracture, and adhesion to a substrate. We numerically implement the model with subdivision surface finite elements.

The simulations reproduce the crack patterns observed in tearing experiments remarkably well. In Chapter 4, based on our phase-field computational model, we find a striking influence of shell shape on crack propagation, suggesting that geometric features could be used to control crack propagation and path. To shed light on this phenomenon, we derive an expression for the configurational force conjugate to crack extension for Koiter's linear theory of thin shells. In Chapter 5, we present some concluding remarks and discuss future research directions.

Chapter 2

Fracture in brittle materials with anisotropic surface energy

2.1 Introduction

Most materials are anisotropic, also with regards to their fracture behavior. While most theoretical and computational studies have focused on elastic anisotropy (Stroh, 1958; Barnett and Asaro, 1972; Gao and Chiu, 1992), the anisotropy of the fracture toughness influences more strongly the crack propagation of a wide variety of materials including single crystals (Argon and Qiao, 2002; Pérez and Gumbsch, 2000; Riedle et al., 1996), extruded polymers (Takei et al., 2013), geological materials (Donath, 1961; Duveau et al., 1998), including sedimentary (Niandou et al., 1997) and granitic rocks (Nasseri and Mohanty, 2008), or apple flesh (Khan and Vincent, 1993). The issue of brittle crack propagation in materials with anisotropic surface energy deeply interrogates our understanding of fracture, and is receiving increasing attention from a variety of points of view, such as molecular dynamics (Marder, 2004), continuum mechanics (Gurtin and Podio-Guidugli, 1998; Chambolle et al., 2009), phase-field modeling (Hakim and Karma, 2005, 2009), and experiments (Takei et al., 2013; Azhdari et al., 1998). Here, by exploiting the analogy with crystal growth, we develop and implement numerically a phase-field model for brittle fracture of materials with strongly anisotropic surface energy, and interpret our numerical results in the light of

recent theories and experiments.

As reviewed in Chapter 1, different popular crack path selection criteria, in general, provide similar predictions for homogeneous isotropic materials. However, a stress-based criterion such as that based on the maximum hoop stress is not physically reasonable when the material is elastically isotropic but its surface energy is anisotropic. The PLS and MERR criteria greatly differ when generalized to materials with anisotropic surface energy, in which the fracture toughness $G_c(\theta)$ is orientation dependent.

Recent experiments on thin anisotropic films have interrogated the MERR criterion in materials with anisotropic fracture toughness, examining the global maximization of $G(\theta)/G_c(\theta)$ as a crack path principle (Takei et al., 2013). By examining strongly anisotropic materials, these experiments established a close analogy with crystal growth and the Wulff construction for the equilibrium shape of a crystal in materials with strongly anisotropic surface energy, which exhibit forbidden orientations and faceted surfaces. This analogy had been previously pointed out theoretically in Gurtin and Podio-Guidugli (1998). Furthermore, these experiments report crack propagation along metastable directions, suggesting a principle based on local maximization rather than global maximization of $G(\theta)/G_c(\theta)$.

Phase-field models have been used previously to examining crack propagation in materials with anisotropic surface energy (Hakim and Karma, 2005, 2009). However, they have been developed within a framework that only allows for weakly two-fold anisotropic surface energies (elliptic polar energy graphs). Yet, many of the interesting features of fracture in anisotropic materials, such as sawtooth crack patterns or forbidden crack directions, are directly related to the non-convexity of strongly anisotropic surface energies (Takei et al., 2013). Here, we start from a regularized variational theory of brittle fracture (Bourdin et al., 2000), and modify it by formulating a strongly anisotropic surface energy inspired by phase-field models of crystal growth. This results in a fourth-order system of partial differential equations (PDE) for the displacement and for the phase-field representing the cracks. The variational nature of this model suggests that the underlying crack-path selection principle is re-

lated to the MERR criterion, and in fact it has been shown through asymptotic analysis that cracks propagate obeying the configurational equilibrium $dG/d\theta = dG_c/d\theta$ in a weakly anisotropic phase-field model (Hakim and Karma, 2009). We implement numerically the proposed model with local maximum entropy meshfree approximants (Arroyo and Ortiz, 2006), which allow us to directly deal with the high-order nature of the PDE (Rosolen et al., 2013a,b), and explore the fracture behavior of the model in the light of the experiments by Takei et al. (2013).

In Section 2.2 we summarize previous variational phase-field models for fracture, introduce the notion of the extended Cahn-Hilliard model to define anisotropic surface energies, and show how to integrate it in a model for fracture. Section 2.3 succinctly describes the numerical implementation of the model, and Section 2.4 presents representative simulations, showing the fundamental features of fracture in materials with strongly anisotropic surface energy. Section 2.5 collects our final remarks and conclusions.

2.2 Phase-field model for materials with anisotropic surface energy

2.2.1 Background

A variational free-discontinuity generalization of Griffith's theory of brittle fracture was proposed by Francfort and Marigo (1998), addressing issues such as crack nucleation, path selection, and discontinuous crack propagation. In this theory, the total energy, including bulk elastic and crack surface contributions, is simultaneously minimized with respect to any admissible crack set and displacement field. This theory was subsequently regularized into a phase-field model, suitable for numerical calculations (Bourdin et al., 2000), and which converges to the sharp variational theory of brittle fracture (Bourdin et al., 2008). These works have prompted a large body of literature in mathematics, mechanics, and computational mechanics that we do not attempt to

review here. In the regularized model, cracks are represented by a phase-field variable (scalar order parameter) ϕ, which is 0 inside a cracked zone, 1 away from the crack, and changes from 0 to 1 smoothly. The total free energy of a possibly cracked elastic body Ω is modeled by

$$E[\mathbf{u}, \phi] = \int_\Omega (\phi^2 + \eta_k) W(\boldsymbol{\varepsilon}) \, d\Omega + \int_\Omega G_c \left[\frac{(\phi - 1)^2}{4\kappa} + \kappa |\nabla \phi|^2 \right] d\Omega, \qquad (2.1)$$

where $\mathbf{u}$ is the displacement field, W is the elastic strain energy depending on the strain tensor $\boldsymbol{\varepsilon} = 1/2 \left(\nabla \mathbf{u} + \nabla \mathbf{u}^T \right)$, and G_c is the energy release rate (fracture surface energy). This family of functionals is parametrized by $\kappa > 0$, a regularization parameter with units of length dictating the width of the smeared crack. When it goes to zero, the regularized model converges to the Griffith-like model studied in Francfort and Marigo (1998), but numerical simulations require a finite value of κ, which needs to be resolved by the grid. The parameter η_k is such that $0 < \eta_k << 1$ and can be seen as a vanishing residual stiffness of the cracks. Although it is not technically necessary from a mathematical standpoint (Bourdin et al., 2011), it is used to prevent ill-conditioning of stiffness matrix in the numerical implementation. For simplicity, we do not consider here body forces or surface tractions. The first integral of the functional is the elastic energy of a possibly damaged material, while the second integral approximates the surface energy. The minimization of the functional in Eq. (2.1) with respect to both $\mathbf{u}$ and ϕ, subject to Dirichlet data and to irreversibility of cracks provides a computable approximation of the generalized Griffith's fracture theory.

Since the Euler-Lagrange equations resulting from Eq. (2.1) is a system of second order PDE, it has been referred to as a *second order phase-field theory* of fracture (Borden et al., 2014). The profile of the phase-field perpendicular to the crack can be analyzed by neglecting the elastic energy and looking for a one dimensional stationary solution. As shown in Figure 2.1(a), the second order phase-field model leads to a C^0 solution, exhibiting a discontinuous derivative at the crack. Since greater regularity of the exact solution provides better accuracy and convergence rates for numerical solutions, a higher order phase-field model was introduced (Borden et al., 2014),
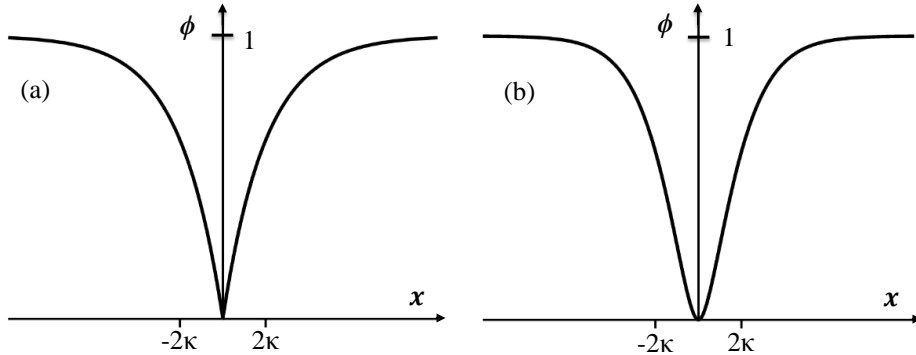
Figure 2.1: One dimensional phase-field approximation of crack at $x = 0$: (a) second order phase-field theory, (b) fourth order phase-field theory.

where total free energy is given by

$$E[\mathbf{u}, \phi] = \int_\Omega (\phi^2 + \eta_k) W(\mathbf{u}) \, d\Omega + \int_\Omega G_c \left[\frac{(\phi - 1)^2}{4\kappa} + \frac{1}{2}\kappa |\nabla \phi|^2 + \frac{1}{4}\kappa^3 (\Delta\phi)^2 \right] d\Omega. \quad (2.2)$$

This *fourth order phase-field theory* leads to C^1 continuous solutions, as shown in Figure 2.1(b).

When turning to materials with anisotropic surface energy, the parameter G_c in the model can no longer be a scalar since it needs to be orientation-dependent. Anisotropic surface energy is also very important in crystal growth or solidification, extensively studied in the materials science literature. Anisotropic surface energy has been specifically studied in the context of phase-field models for crystal growth/solidification. In a classical model (Kobayashi, 1993), the coefficient pre-multiplying $|\nabla\phi|^2$ in the surface energy is made dependent on the phase-field approximation of the outer normal vector $\mathbf{n} = \frac{\nabla\phi}{|\nabla\phi|}$ to the interface. In this way, such models introduce explicitly an orientation-dependent surface energy, $G_c(\mathbf{n})$ in our context. This approach is very appealing because it allows one to freely choose the functional form of this dependence. For strongly anisotropic surface energy, i.e. when the polar plot of the reciprocal surface energy, $1/G_c(\mathbf{n})$, is non-convex, is has been shown that the corresponding phase-field equations become ill-posed (Taylor and Cahn, 1998). An expedite and homogenized approach to deal with strongly anisotropic surface energies is to convexify the surface

16

energy (Eggleston et al., 2001), at the expense of missing interesting details of the geometric structure of the free-surface. Since strongly anisotropic surface energies are important in applications and the details about the free-surface matter, researchers have developed other remedies to this difficulty, for instance regularizing the phase-field functional by adding the square of the Laplacian or a phase-field approximation to the Willmore curvature energy, see (Torabi et al., 2009) and references therein. This method works well for models with phase-field variations across the interface approximating smoothly step functions, such as hyperbolic tangent profiles, but unfortunately cannot be used for phase field model of fracture. The higher-order terms required to regularize the model result in a C^1 continuous phase-field for the crack as in Figure 2.1(b). At the center of the crack, $\nabla \phi = \mathbf{0}$, which renders the formula $\mathbf{n} = \frac{\nabla \phi}{|\nabla \phi|}$ inapplicable. One can try to remedy this problem by defining the outer normal vector $\mathbf{n}$ using eigenvectors of the Hessian matrix $\nabla^2 \phi$, but this definition becomes problematic at other regions, particularly at the crack tip.

A different and natural way to take anisotropy into account is to follow the approach presented in the original work by Cahn and Hilliard (1958), and write the Taylor series expansion of the free energy including higher order terms. In the context of crystal growth, this idea has been shown to provide a satisfactory way of describing systems with anisotropic surface energy and are intrinsically regularized (Abinandanan and Haider, 2001; Torabi and Lowengrub, 2012). However, as shown later, this method imposes constraints on the kinds of orientation dependence of $G_c(\mathbf{n})$. In this paper, we adapt this approach to fracture.

2.2.2 Extended Cahn-Hilliard interface model

The classical phase-field model for isotropic systems was developed in Cahn and Hilliard (1958). In this diffuse interface description, the behavior of a nonuniform system is characterized by the interfacial free energy F, and expressed as an integral of the local free energy density f that is a function of the phase-field ϕ. It can be expanded in a Taylor series about a given phase-field, provided that f is a continuously

differentiable function of its variables:

$$f(\phi, \nabla\phi, \nabla^2\phi, \dots) = f_0(\phi) + \sum_i L_i \frac{\partial\phi}{\partial x_i} + \sum_{ij} \kappa_{ij}^{(1)} \frac{\partial^2\phi}{\partial x_i \partial x_j}$$
$$+ \frac{1}{2}\sum_{ij} \kappa_{ij}^{(2)} \frac{\partial\phi}{\partial x_i}\frac{\partial\phi}{\partial x_j} + \dots, \tag{2.3}$$

where ∇ and ∇^2 are the gradient and the Hessian operators, and

$$L_i = \left(\frac{\partial f}{\partial p_i}\right)\bigg|_0, \qquad p_i = \frac{\partial\phi}{\partial x_i}, \tag{2.4}$$

$$\kappa_{ij}^{(1)} = \left(\frac{\partial f}{\partial q_{ij}}\right)\bigg|_0, \qquad q_{ij} = \frac{\partial^2\phi}{\partial x_i \partial x_j}, \tag{2.5}$$

$$\kappa_{ij}^{(2)} = \left(\frac{\partial^2 f}{\partial p_i \partial p_j}\right)\bigg|_0. \tag{2.6}$$

The subscript 0 indicates evaluation at a given phase-field. By applying the divergence theorem, the two second-rank tensor $\kappa_{ij}^{(1)}$ and $\kappa_{ij}^{(2)}$ can be reduce to only one (Cahn and Hilliard, 1958). Therefore, the interfacial free energy is given by

$$F[\phi] = \int_\Omega \left(f_0(\phi) + \sum_i L_i \frac{\partial\phi}{\partial x_i} + \sum_{ij} \kappa_{ij} \frac{\partial\phi}{\partial x_i}\frac{\partial\phi}{\partial x_j} \right) d\Omega, \tag{2.7}$$

where $\kappa_{ij} = -\frac{d\kappa_{ij}^{(1)}}{d\phi} + \frac{1}{2}\kappa_{ij}^{(2)}$. This model for the interfacial energy involves a second-rank tensor, κ_{ij}. Therefore, it can describe up to orthorhombic weak anisotropy, as exploited in previous phase-field models of anisotropic fracture (Hakim and Karma, 2009). But this anisotropy is too restrictive; for instance, it cannot describe the common cubic symmetry and cannot model strongly anisotropic effects (Taylor and Cahn, 1998). Since higher-rank tensors can produce more general anisotropy, we extend the Taylor series expansion of local free energy density to higher order, here up to fourth order. This leads to extended Cahn-Hilliard-type equations (Abinandanan and Haider, 2001; Torabi and Lowengrub, 2012; McKenna et al., 2009).

Following this approach, we expand the local free energy density f to higher order

$$
\begin{aligned}
f(\phi, \nabla\phi, \nabla^2\phi, \ldots) = {} & f_0(\phi) + \sum_{ij} \kappa_{ij}^{(1)} \frac{\partial^2 \phi}{\partial x_i \partial x_j} + \frac{1}{2} \sum_{ij} \kappa_{ij}^{(2)} \frac{\partial \phi}{\partial x_i} \frac{\partial \phi}{\partial x_j} \\
& + \frac{1}{24} \sum_{ijkl} \lambda_{ijkl}^{(1)} \frac{\partial \phi}{\partial x_i} \frac{\partial \phi}{\partial x_j} \frac{\partial \phi}{\partial x_k} \frac{\partial \phi}{\partial x_l} + \frac{1}{6} \sum_{ijkl} \lambda_{ijkl}^{(2)} \frac{\partial^2 \phi}{\partial x_i \partial x_j} \frac{\partial \phi}{\partial x_k} \frac{\partial \phi}{\partial x_l} \\
& + \frac{1}{2} \sum_{ijkl} \lambda_{ijkl}^{(3)} \frac{\partial^2 \phi}{\partial x_i \partial x_j} \frac{\partial^2 \phi}{\partial x_k \partial x_l} + \frac{1}{2} \sum_{ijkl} \lambda_{ijkl}^{(4)} \frac{\partial^3 \phi}{\partial x_i \partial x_j \partial x_k} \frac{\partial \phi}{\partial x_l} \\
& + \sum_{ijkl} \lambda_{ijkl}^{(5)} \frac{\partial^4 \phi}{\partial x_i \partial x_j \partial x_k \partial x_l} + \ldots
\end{aligned}
\tag{2.8}
$$

The tensorial Taylor series coefficients must reflect the underlying symmetry of material. We omit odd-ranked tensors, since they are zero for the centrosymmetric materials of interest in the present study. As in Cahn and Hilliard (1958), we present below a formal definition of the remaining even-ranked tensors:

$$
\lambda_{ijkl}^{(1)} = \left. \left(\frac{\partial^4 f}{\partial p_i \partial p_j \partial p_k \partial p_l} \right) \right|_0 , \tag{2.9}
$$

$$
\lambda_{ijkl}^{(2)} = \left. \left(\frac{\partial^3 f}{\partial q_{ij} \partial p_k \partial p_l} \right) \right|_0 , \tag{2.10}
$$

$$
\lambda_{ijkl}^{(3)} = \left. \left(\frac{\partial^2 f}{\partial q_{ij} \partial q_{kl}} \right) \right|_0 , \tag{2.11}
$$

$$
\lambda_{ijkl}^{(4)} = \left. \left(\frac{\partial^2 f}{\partial r_{ijk} \partial p_l} \right) \right|_0 , \quad r_{ijk} = \frac{\partial^3 \phi}{\partial x_i \partial x_j \partial x_k} , \tag{2.12}
$$

$$
\lambda_{ijkl}^{(5)} = \left. \left(\frac{\partial f}{\partial s_{ijkl}} \right) \right|_0 , \quad s_{ijkl} = \frac{\partial^4 \phi}{\partial x_i \partial x_j \partial x_k \partial x_l} . \tag{2.13}
$$

From these definitions and since the order of differentiation can be exchanged for sufficiently smooth functions, these tensors possess various symmetries. Following similar arguments as before, the number of fourth-rank tensors can be reduced from five to three (Abinandanan and Haider, 2001), and hence the local free energy density

f can be written as:

$$f(\phi, \nabla\phi, \nabla^2\phi) = f_0(\phi) + \sum_{ij} \kappa_{ij} \frac{\partial\phi}{\partial x_i} \frac{\partial\phi}{\partial x_j} + \sum_{ijkl} \tilde{\alpha}_{ijkl} \frac{\partial\phi}{\partial x_i} \frac{\partial\phi}{\partial x_j} \frac{\partial\phi}{\partial x_k} \frac{\partial\phi}{\partial x_l}$$
$$+ \sum_{ijkl} \tilde{\beta}_{ijkl} \frac{\partial^2\phi}{\partial x_i \partial x_j} \frac{\partial\phi}{\partial x_k} \frac{\partial\phi}{\partial x_l} + \sum_{ijkl} \tilde{\gamma}_{ijkl} \frac{\partial^2\phi}{\partial x_i \partial x_j} \frac{\partial^2\phi}{\partial x_k \partial x_l}. \tag{2.14}$$

2.2.3 Anisotropic phase field fracture model

Here, we only consider cubic symmetry, and therefore the second-rank tensor κ_{ij} should be isotropic, i.e. a scalar coefficient κ, which as discussed earlier has units of length in the present context, see Eq. (2.1). Under cubic symmetry, any given fourth-rank tensor C_{ijkl} expressed in the material principal axes has only three independent parameters. Resorting to Voigt notation, such tensors in 3D take the form

$$\begin{bmatrix} C_{11} & C_{12} & C_{12} & & & \\ C_{12} & C_{11} & C_{12} & & 0 & \\ C_{12} & C_{12} & C_{11} & & & \\ & & & C_{44} & & \\ & 0 & & & C_{44} & \\ & & & & & C_{44} \end{bmatrix}, \tag{2.15}$$

while in 2D the tensor C_{ijkl} can be written as

$$\begin{bmatrix} C_{11} & C_{12} & 0 \\ C_{12} & C_{11} & 0 \\ 0 & 0 & C_{44} \end{bmatrix}. \tag{2.16}$$

See Appendix A for the expression of these tensors when the principal material axes are not aligned with the coordinate axes.

By using this rule for $\tilde{\alpha}_{ijkl}, \tilde{\beta}_{ijkl}$ and $\tilde{\gamma}_{ijkl}$, and rescaling these tensors as $(\alpha, \beta, \gamma) =$

$(\tilde{\alpha}, \tilde{\beta}, \tilde{\gamma})/\kappa^3$ to make them non-dimensional, the surface energy F in 2D becomes

$$
\begin{aligned}
F[\phi] = \bar{G}_c \int_\Omega \Bigg\{ & f_0(\phi) + \kappa|\nabla\phi|^2 + \kappa^3 \Bigg[2\left(\alpha_{12} + 2\alpha_{44} - \alpha_{11}\right)\left(\frac{\partial\phi}{\partial x}\right)^2 \left(\frac{\partial\phi}{\partial y}\right)^2 \\
& + \alpha_{11}|\nabla\phi|^4 + (\beta_{12} - \beta_{11})\left(\frac{\partial^2\phi}{\partial x^2}\left(\frac{\partial\phi}{\partial y}\right)^2 + \frac{\partial^2\phi}{\partial y^2}\left(\frac{\partial\phi}{\partial x}\right)^2\right) \\
& + 4\beta_{44}\frac{\partial^2\phi}{\partial x\partial y}\frac{\partial\phi}{\partial x}\frac{\partial\phi}{\partial y} + \beta_{11}|\nabla\phi|^2\Delta\phi + 2(\gamma_{12} - \gamma_{11})\frac{\partial^2\phi}{\partial x^2}\frac{\partial^2\phi}{\partial y^2} \\
& + 4\gamma_{44}\left(\frac{\partial^2\phi}{\partial x\partial y}\right)^2 + \gamma_{11}\left(\Delta\phi\right)^2 \Bigg] \Bigg\} d\Omega,
\end{aligned}
\tag{2.17}
$$

where $\bar{G}_c$ is an energy per unit area scale for the surface energy. As discussed below, the actual surface energy $G_c(\theta)$ in this model is orientation dependent, and therefore $\bar{G}_c$ does not have a direct mechanical interpretation. The 3D interfacial free energy can be written analogously.

Having the above anisotropic interfacial free energy F, we can formulate the anisotropic phase field model for fracture as

$$
E[\mathbf{u}, \phi] = \int_\Omega (g(\phi) + \eta_k)W(\boldsymbol{\varepsilon})\, d\Omega + F[\phi],
\tag{2.18}
$$

where there are different choices for the functions $f_0(\phi)$ and $g(\phi)$ consistent with the variational theory of brittle fracture, see, for example, (Pham et al., 2011; Pham and Marigo, 2013) for a discussion. Here we adopt the standard choices $f_0 = (1 - \phi)^2/(4\kappa)$ and $g(\phi) = \phi^2$, although it has been suggested that $g(\phi) = \phi^3$ prevents the emergence of spurious damage away from the crack tip and better mimics a linear elastic-brittle behavior for finite κ (Borden, 2012), at the expense of nonlinearity in the model.

2.2.4   Resulting anisotropic surface energy

To gain insight about the resulting anisotropic surface energy, we consider a planar crack interface with a normal vector $\mathbf{n}$ forming an angle θ with the x-axis, and in-

troduce a coordinate perpendicular to the crack $z = \mathbf{x} \cdot \mathbf{n}$. We neglect the elastic energy and rewrite the free energy in Eq. (2.17) assuming that $\phi = \phi(z)$. We have $\frac{\partial \phi}{\partial x} = \frac{\partial \phi}{\partial z} \cos \theta$ and $\frac{\partial \phi}{\partial y} = \frac{\partial \phi}{\partial z} \sin \theta$, and consequently the surface energy becomes

$$
\begin{aligned}
F[\phi] = \bar{G}_c \int_{\Omega} \Bigg\{ & f_0(\phi) + \kappa \left(\frac{\partial \phi}{\partial z} \right)^2 + \kappa^3 \Bigg[\left(\alpha_{11} + \frac{1}{2}(\alpha_{12} - \alpha_{11} + 2\alpha_{44}) \sin^2(2\theta) \right) \left(\frac{\partial \phi}{\partial z} \right)^4 \\
& + \left(\beta_{11} + \frac{1}{2}(\beta_{12} - \beta_{11} + 2\beta_{44}) \sin^2(2\theta) \right) \frac{\partial^2 \phi}{\partial z^2} \left(\frac{\partial \phi}{\partial z} \right)^2 \\
& + \left(\gamma_{11} + \frac{1}{2}(\gamma_{12} - \gamma_{11} + 2\gamma_{44}) \sin^2(2\theta) \right) \left(\frac{\partial^2 \phi}{\partial z^2} \right)^2 \Bigg] \Bigg\} d\Omega.
\end{aligned}
\tag{2.19}
$$

The tensor β_{ijkl} has no contribution to the surface energy, since

$$
\begin{aligned}
\int_{\Omega} \left(\beta_{11} + \frac{1}{2}(\beta_{12} - \beta_{11} + 2\beta_{44}) \sin^2(2\theta) \right) \frac{\partial^2 \phi}{\partial z^2} \left(\frac{\partial \phi}{\partial z} \right)^2 d\Omega \\
= \frac{1}{3} \left(\beta_{11} + \frac{1}{2}(\beta_{12} - \beta_{11} + 2\beta_{44}) \sin^2(2\theta) \right) \left(\frac{\partial \phi}{\partial z} \right)^3 \Bigg|_{-\infty}^{+\infty},
\end{aligned}
\tag{2.20}
$$

and $\partial \phi / \partial z$ vanishes away from the crack. Consequently, this term does not enter into the Euler-Lagrange equation in this idealized planar crack setting. Accordingly the energy in Eq. (2.19) simplifies to

$$
F[\phi] = \bar{G}_c \int_{\Omega} \left\{ f_0(\phi) + \kappa \left(\frac{\partial \phi}{\partial z} \right)^2 + \kappa^3 \left[\alpha \left(\frac{\partial \phi}{\partial z} \right)^4 + \gamma \left(\frac{\partial^2 \phi}{\partial z^2} \right)^2 \right] \right\} d\Omega,
\tag{2.21}
$$

where γ is given by

$$
\gamma = \gamma_0 \left(1 + \gamma_4 \cos(4\theta) \right),
\tag{2.22}
$$

$$
\gamma_0 = \frac{3\gamma_{11} + \gamma_{12} + 2\gamma_{44}}{4}, \gamma_4 = \frac{\gamma_{11} - \gamma_{12} - 2\gamma_{44}}{3\gamma_{11} + \gamma_{12} + 2\gamma_{44}},
\tag{2.23}
$$

and α can be written similarly.
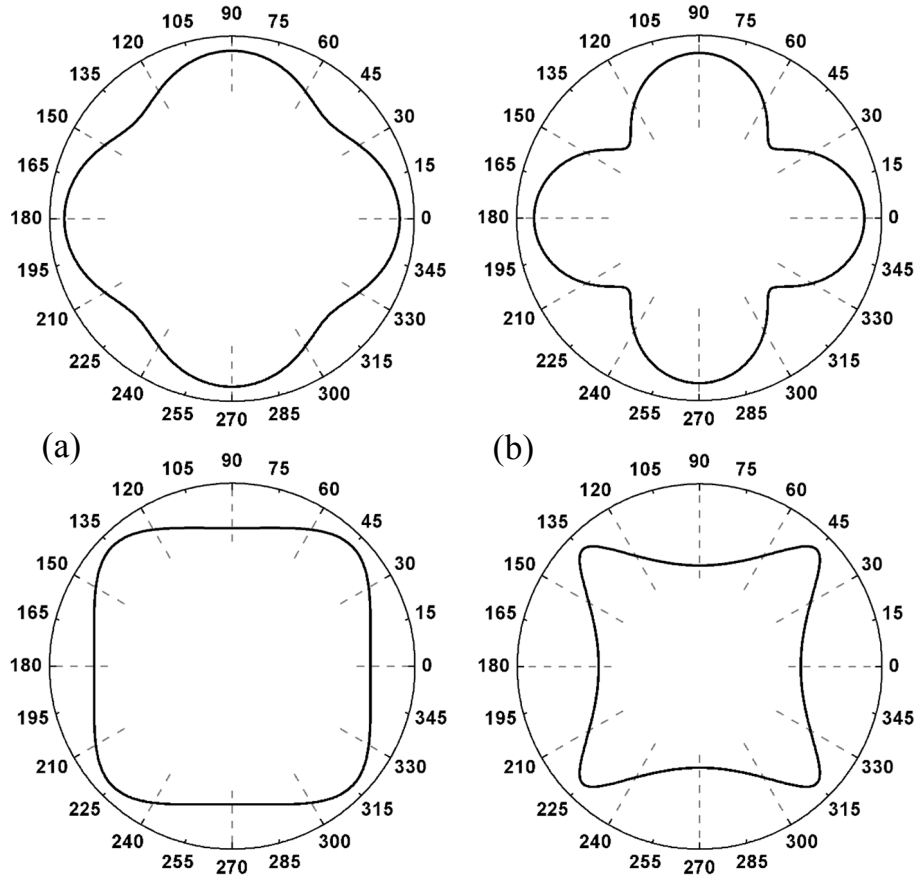
Figure 2.2: Polar representation of the surface energy (top) and its reciprocal (bottom) only considering the tensor γ_{ijkl} (α and β are set to zero). (a) shows a weakly anisotropic energy (convex reciprocal energy plot) with $\gamma_0 = 10.0$ and $\gamma_4 = 0.5$. (b) shows a strongly anisotropic energy with $\gamma_0 = 10.0$ and $\gamma_4 = 0.9$.

In absence of an analytical solution to the Euler-Lagrange equation of this functional, the crack profile and interface energy can be calculated numerically. To compute the surface energy as a function of orientation, $G_c(\theta)$, we fix θ and solve the Euler-Lagrange equation of the functional in Eq. (2.21), a 4th order ordinary differential equation, subject to the following boundary conditions: $\phi(0) = \phi'(0) = \phi'(+\infty) = 0$ and $\phi(+\infty) = 1$. In practice, one of the boundaries is taken sufficiently far away from $z = 0$, e.g. 50 κ, and the differential equation is approximated with MATLAB's $bvp4c$ function, implementing an adaptive collocation method. For each θ, we evaluate the functional in Eq. (2.21) at corresponding optimal profile to obtain a polar plot of the surface energy and its reciprocal, as shown in Figure 2.2 for several parameter values. It is clear that, consistently with the assumed cubic symmetry of the model, the polar plots exhibit four-fold symmetry. The figure shows that the tensor γ_{ijkl} can produce both weakly and strongly anisotropic energies, as indicated by the convexity of the polar plots of $1/G_c(\theta)$. Since the tensors α_{ijkl} and β_{ijkl} introduce nonlinearity in the surface energy, that becomes non-quadratic, here we focus on models including only the tensor γ_{ijkl}. It is interesting to note that models with only the tensor α_{ijkl} can produce strongly anisotropic surface energies (not shown here), but result in nonlinear second order partial differential equations. This makes the numerical discretization simpler, as C^0 finite elements could be directly used, but as previously discussed, other second-order strongly anisotropic models have been shown to be ill-posed because the energy of kinks is not stabilized (Taylor and Cahn, 1998).

With Figure 2.2 at hand, we can further discuss the notion of strong surface energy anisotropy. The classical Wulff construction for the equilibrium shape of crystals (Herring, 1951) naturally distinguishes between energies with convex and non-convex reciprocal energy plot. Non-convex plots lead to forbidden free surface directions and faceting. In the crystal growth literature, there is another local notion of surface stability, given in 2D by the surface stiffness

$$S(\theta) = G_c''(\theta) + G_c(\theta), \tag{2.24}$$

which has the sign of the curvature of the polar plot of the reciprocal surface energy (Müller and Métois, 2008). This local characterization of convexity, and of strong/weak anisotropy, does not coincide with the global characterization in terms of the convexity of the polar plot of $1/G_c(\theta)$ for non-smooth energies. Furthermore, as illustrated in the examples and in Takei et al. (2013), the local characterization of free surface (crack) stability is less restrictive than the global characterization, in that it allows for metastable orientations. The local characterization of surface stability in 3D is discussed in Sekerka (2005).

We note that in the present phase-field model, the thickness of the interface depends on the orientation. Identifying the smallest thickness is important to set the parameter κ, with units of length, relative to the grid spacing. In the isotropic limit, this model gives rise to a family of higher order phase-field models. In particular, if all terms α_{ij}, β_{ij} and γ_{ij} are zero except for $\gamma_{11} = \gamma_{12}$, we recover the fourth-order model proposed in Borden et al. (2014).

2.3   Numerical implementation

Since the free energy involves second order derivatives of ϕ, a direct Galerkin approach requires C^1 continuous approximations. We resort here to the local maximum entropy (LME) approximants (Arroyo and Ortiz, 2006), a meshfree method with non-negative and smooth basis functions. In this method, the support size of the basis functions can be modified through a non-dimensional aspect ratio parameter, which we take equal to 1.0 in all examples (Rosolen et al., 2010). LME approximants have been successfully applied to fourth-order phase-field models, e.g. in the simulation of biomembranes (Rosolen et al., 2013b; Peco et al., 2013). Adaptive local refinement is straightforward, and leads to very efficient phase-field solutions as elaborated in the references above, although we do not fully exploit this feature here. Adaptive refinement can be cumbersome in other techniques delivering smooth approximants, such as isogeometric methods. However, recent advances in T-Splines (Scott et al., 2012) and hierarchical B-Splines (Vuong et al., 2011) alleviate the rigidity of these

methods, and may soon become accessible in 3D (Wang et al., 2013). These adaptive spline techniques have been exploited in the numerical approximation of higher-order phase-field models of fracture (Borden et al., 2014). To combine the highly accurate boundary representation of isogeometric methods with the flexibility of LME in the bulk, we have recently proposed a blending method (Rosolen and Arroyo, 2013).

We make sure that the phase-field profile is sufficiently resolved by the grid, by requiring that the regularization length κ is large enough compared to the grid spacing h, i.e. $\kappa > 2h$. Since the crack path is not known a priori, we consider uniform grids, except in the regions where cracks cannot propagate, see Examples 2 and 3 below. All the simulations consider an elastically isotropic material with Young's modulus $E = 10^9$ N/m^2 and Poisson's ratio $\nu = 0.3$.

We minimize the total energy in Eq. (2.18) with respect to the displacement field and the phase-field following the alternate minimization algorithm described in (Bourdin, 2007). At each load step, the energy is first minimized with respect to $\mathbf{u}$ holding ϕ fixed, and then minimized with respect to ϕ holding $\mathbf{u}$ fixed. This procedure is iterated until convergence. This algorithm is particularly convenient in our examples. Since we only consider the extended Cahn-Hilliard model with the tensor γ_{ijkl}, each one of the minimization steps involves a quadratic functional, and hence the solution of a linear system. The minimization of the total energy can be performed with a variety of methods, including a monolithic Newton-type method. It is important to bear in mind that the staggered minimization process, as most optimization algorithms, leads in general to local minimizers, and could even lead to saddle points of the total energy.

2.4 Results

We now demonstrate through representative numerical simulations the ability of the proposed model to capture nontrivial crack patterns in brittle materials with strongly anisotropic surface energy.
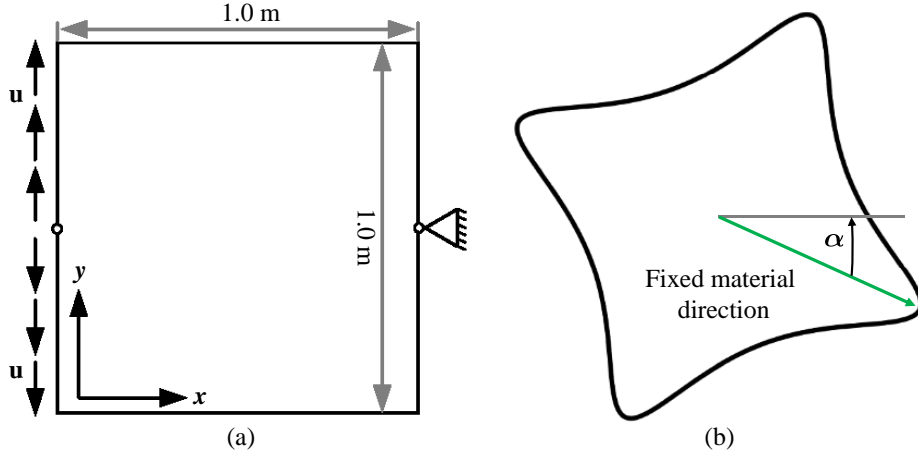
Figure 2.3: Example 1: geometry and boundary condition (a) and polar plot of the reciprocal surface energy (b), exhibiting strong anisotropy. The green arrow indicates a fixed material direction (one of the weakest directions) and α denotes the angle between the fixed material direction and the x axis.

2.4.1 Example 1: crack propagation direction as a function of material orientation

We consider first a square domain with boundary conditions that promote the nucleation of a crack at the center of the left side of the domain, as depicted in Figure 2.3 (a). The material used for the simulations has cubic symmetry and strongly anisotropic fracture surface energy. The surface energy parameters ($\bar{G}_c = 500.0$ N/m, $\gamma_{11} = 19.0$, $\gamma_{12} = -18.0$, $\gamma_{44} = 0.5$) are chosen so that the maximum and minimum of $G_c(\theta)$ are 1157.5 N/m and 707.1 N/m. The model is discretized with 200×200 uniformly distributed control points and the regularized length scale parameter κ is set to 0.01 m. Fixing $\kappa = 0.01$ m, we observe no dependence of the results when the mesh is refined. The polar plot of the reciprocal surface energy is shown in Figure 2.3 (b), where α denotes the angle between a fixed material direction and the x axis. For materials with isotropic surface energy, the symmetry of the surface energy and of the boundary conditions imposes a crack propagation along the x axis. In contrast, for a material with anisotropic surface energy, the crack path will emerge from a competition between elastic energy release rate maximization and surface energy

| Phase field | Material orientation polar plot of $1/G_c$ | Schematic representation of material and crack orientation |
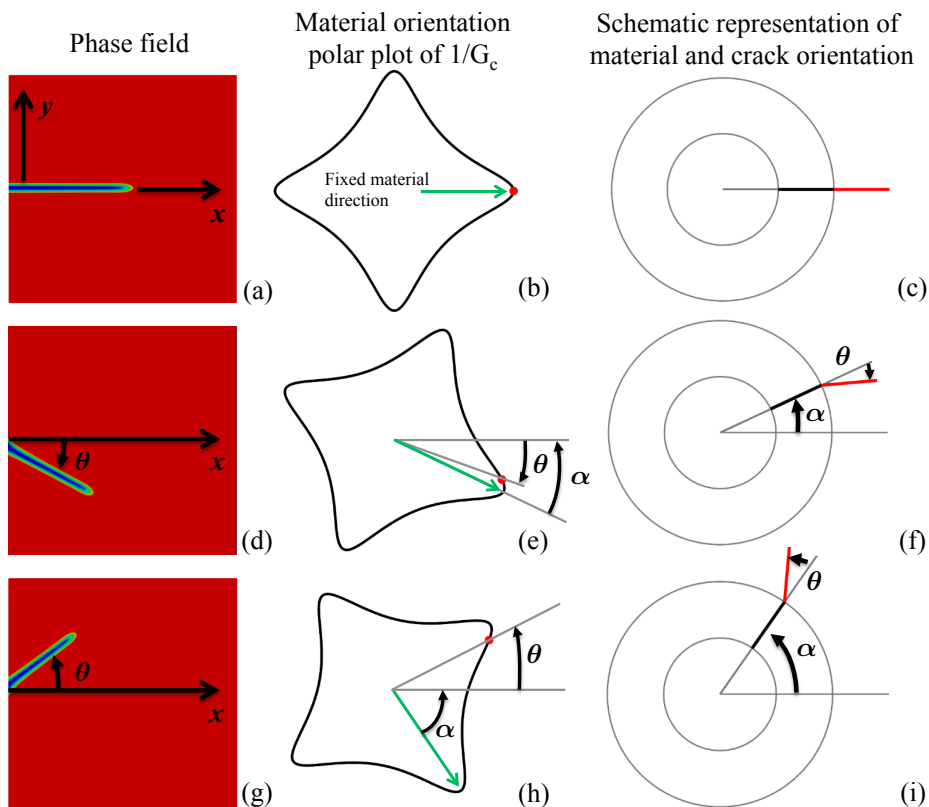
Figure 2.4: Example 1, as the material orientation is rotated relative to the sample geometry (top to bottom). α denotes the material orientation and θ the crack orientation, both relative to the x axis aligned with the specimen. The first column shows the phase field for a material oriented as shown in the second column, representing the polar plot of the reciprocal surface energy. The right column shows a schematic polar representation of the crack orientation (red segments, weak directions are vertical and horizontal) and the material orientation (black segment).

minimization, and therefore will in general deviate from the x direction.

We analyze next how the crack direction changes as we change the material orientation. When the fixed material direction represented by the green arrow, a weak direction, coincides with the x axis, the crack will propagate along this axis, see Figure 2.4 (a) and (b). This situation is schematically shown in Figure 2.4 (c), where the black line, representing material orientation, and red line, representing the crack propagation direction, are collinear. When the fixed material direction is rotated clockwise by an angle α ($\alpha \leq 45°$) with respect to the x axis, the crack orientation
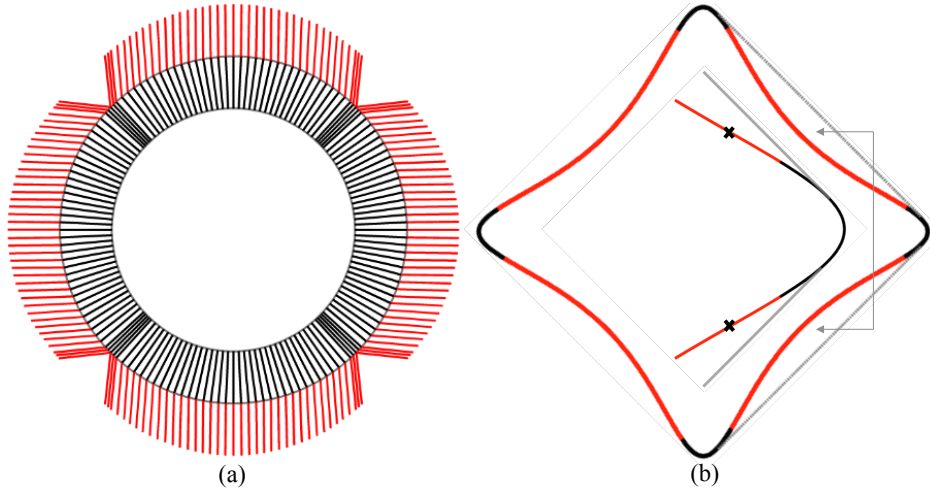
Figure 2.5: Systematic dependence of crack propagation (red segments) with material orientation (black segments), represented as a rosace with the convention of the previous figure (a). The polar plot of the reciprocal surface energy is represented in (b), and color coded depending on whether a given orientation is ever observed (black) or not (red) as we continuously rotate the material orientation. The inset shows that there are observed crack directions within the convex hull of the polar plot. The region of observed cracks appears to correspond with the region of positive surface energy stiffness $S(\theta)$ (positive curvature of the polar plot), see Eq. (2.24).

also rotates clockwise by an angle θ relative to the x axis, see Figure 2.4 (d) and (e). The schematic representation of this situation is shown in Figure 2.4 (f). The sum of these signed angles $\alpha + \theta$, i.e. the deviation of the red segment from the horizontal, quantifies the crack deviation from the weakest material direction. When the fixed material direction is further rotated clockwise ($\alpha \geq 45°$), the crack no longer follows the clockwise rotation of the material, but rather finds an energetically favorable configuration by rotating counter-clockwise by a smaller amount, see Figure 2.4 (g), (h), and (i). Following the analogy of Wulff's construction (Takei et al., 2013), this behavior can be understood by noting that the preferred crack direction is given by the first tangency point of the polar plots in Figure 2.4 (b,e,h) with a vertical line moving leftwards towards the polar plot. Since this analogy is only an approximation in the present setting, the red points denoting the actual crack orientations slightly deviate from the tangency points just described.

We analyze next the systematic dependence of the crack propagation direction as a function of material orientation, and visualize it with the previously introduced schematic representation as a rosace plot in Figure 2.5 (a). This figure clearly highlights the four sectors of forbidden crack directions, as in the experiments in (Takei et al., 2013). The polar plot of the reciprocal surface energy is shown in Figure 2.5 (b), where the black line indicates the directions of observed cracks and the red line indicates the crack directions never observed as we continuously rotate the material orientation. The grey line is the double-tangent construction forming the convex hull of the plot, as in the classical Maxwell construction (Huang, 2005). The inset shows that there are observed crack directions inside of the convex-hull of the polar plot, suggesting that a mere convexification of the energy may yield a poor effective model. The regions where cracks are observed seem to agree well with the local stability condition given by the stiffness in Eq. (2.24), and graphically determined by the regions of the polar plot with positive curvature. The experiments in Takei et al. (2013) are consistent with this behavior suggesting a local MERR principle as discussed in the introduction, which in the simulations may be related to the trapping of the algorithm at local minima. However, we find that the point separating observed and forbidden directions, i.e. separating the black from the red portions of the curve, does not coincide with the point where the stiffness of the surface energy, see Eq. (2.24), changes sign. The point where $S(\theta) = 0$ is marked with a cross in the inset of Figure. 2.5 (b). This difference may be due to inaccuracies in the numerical estimation of the crack direction, or to the effect of boundary conditions. In any case, it deserves further scrutiny.

2.4.2 Example 2: Zigzag crack paths

In the presence of strong surface energy anisotropy, we analyze now how a crack propagates when the boundary conditions constrain the crack propagation along a forbidden direction. In the present example, we fully constrain the displacement field in the upper and lower bands of the domain as shown in Figure 2.6 (a) to guide the
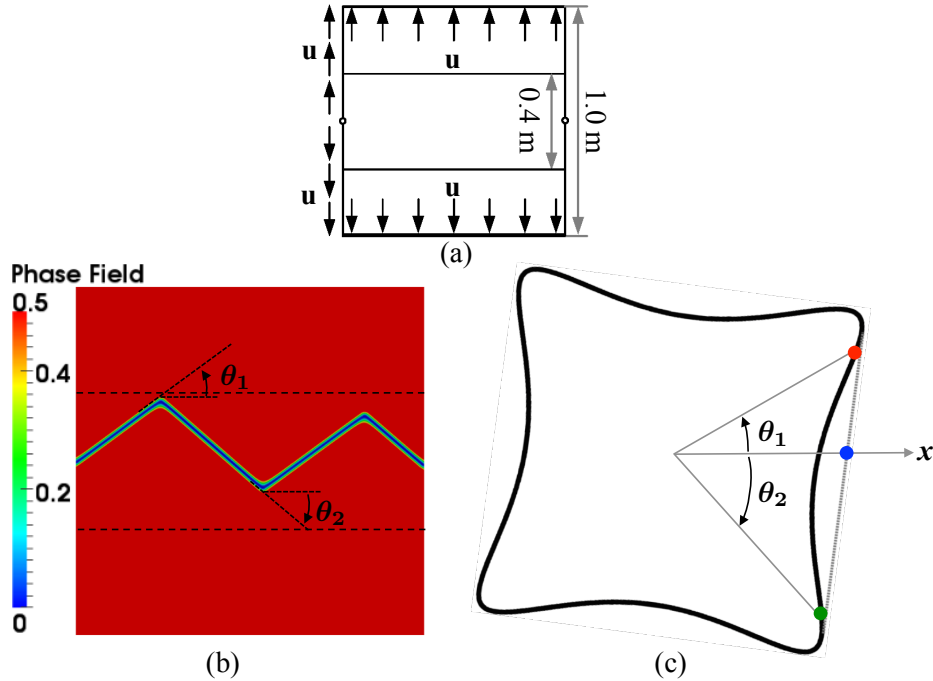
Figure 2.6: Example 2: crack propagation guided along a forbidden direction. (a) Computational model with boundary conditions. The displacement field at top and bottom bands is fully constrained. (b) Zigzag crack path obtained when the crack is guided along a forbidden direction. (c) The polar plot of the reciprocal surface energy and the double-tangent construction

crack as in the groove of a double cantilever beam crack propagation experiment (Wu et al., 1995). A similar crack-guiding device has been implemented in Takei et al. (2013) with tougher adhesive tapes. The surface energy parameters are the same as in Example 1, and κ is set to 0.005 m. The domain is discretized with a spacing of 1/400 m in a central band of 0.5 m height, while the grid is coarser in the upper and lower parts of the domain.

Figure 2.6 (b) shows that, as in Example 1, the system initially chooses crack direction close to a weak direction. However, as the crack feels the presence of the constrained region but before touching it, it sharply turns to adopt a distant weak orientation that drives it apart from the obstacle. Interestingly, this new crack segment with angle θ_2 turns upwards further apart from the constrained band in the lower part of the domain. Analogously, the third and last kinking event occurs before the crack

reaches the upper constrained band. The kinking events are presumably the result of a more favorable elastic energy release rate as the crack deviates from the straight horizontal trajectory and approaches a mechanically constrained region. There is probably an energy cost associated to crack bending, here sharp kinking, implicit in the model and due to the second derivatives in the phase-field in the surface energy. Therefore, the elastic energy release rate incentive to kinking presumably needs to overcome this energetic penalty to sharply turning crack direction. Figure 2.6 (c) shows the representation of the two crack orientations in the polar plot. In an effective model with a convexified surface energy there are no forbidden directions and, if guided, the crack will propagate along the x axis (blue point) with an energy cost given by the double-tangent construction, here 972.5 N/m. We compare this energy with the average surface energy per projected length along x, 1008.5 N/m to find a reasonable agreement. One of the factors that may explain the difference is, again, the energetic cost of kinks implicit in the model, which we have not explored so far.

2.4.3 Example 3

Inspired by the experiments in Takei et al. (2013), we consider now a longer domain with similar boundary conditions to Example 2, as shown in Figure 2.7 (a). We consider here a slightly different surface energy ($\bar{G}_c = 500.0\text{N/m}$, $\gamma_{11} = 17.0$, $\gamma_{12} = -15.0$, $\gamma_{44} = 2.0$) so that the maximum and minimum of $G_c(\theta)$ are 1131.7 N/m and 826.4 N/m. As before, a central strip 0.15 m high has uniformly distributed points with a small node spacing of 1/400 m, while the remainder of the domain has a coarser grid. The regularized length scale parameter κ is set to 0.005 m. As before, we expect that the crack will initially deflect away from the x axis towards a weak direction. However, as shown in Figure 2.7 (b), if the boundary of the guide (here parallel to x) is not a forbidden direction, see Figure 2.7 (c), rather than kinking to adopt a weak direction, the crack runs along a direction of relatively large surface energy. In contrast, if the direction of the guide is a forbidden direction, as in Figure 2.7 (d,e), the crack adopts a sawtooth configuration as in Example 2. Now, the upper kinking
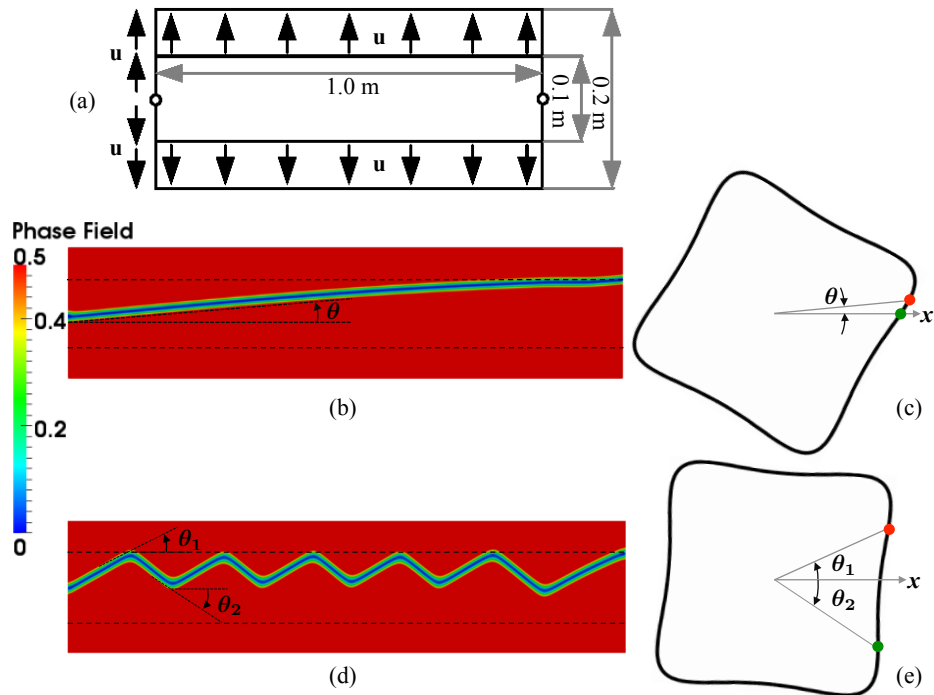
Figure 2.7: Example 3: crack propagation guided along an allowed but high energy direction (b,c) or along a forbidden direction (d,e). The red and green dots in (c) represent the initial and final crack orientation, while in (e) represent the two orientations of the sawtooth pattern.

points are precisely at the upper boundary of the crack guide, while the lower kinks are very far apart from the lower boundary of the guide. As before, the location of these kinks emerges from the competition of elastic energy release rate, surface energy, and possibly kinking energy. The essential phenomenology of these two calculations has been reported experimentally in Takei et al. (2013).

2.5 Conclusions

The fracture behavior of materials with strongly anisotropic surface energy is very important in many applications, and leads to very interesting physics, including forbidden crack propagation directions, the possibility of guiding cracks along relatively high-energy directions, and sawtooth crack patterns. However, strongly anisotropic fracture had not been simulated computationally before to the best of our knowledge. This problem of fracture mechanics forces us to deeply interrogate fundamental questions such as the criteria to select the crack path. Recent theoretical (Chambolle et al., 2009) and experimental (Takei et al., 2013) studies favor a natural generalization of the maximum energy release rate (MERR) criterion. Previous phase-field models for weak anisotropy of the surface energy are consistent with this view, and support a configurational torque balance (Hakim and Karma, 2009) equivalent to MERR under certain conditions. The current work, presenting a variational phase-field model for materials with strongly anisotropic surface energy, provides a new tool to analyze this problem from the computational side, and may be a starting point for the mathematical analysis of this problem. From a computational viewpoint, phase-field models appear as the best approach to investigate this complex problem where the crack orientation selection is so crucial. The variational nature of the model suggests that it obeys a MERR principle to select crack paths, and since we obtain crack propagation directions within the convex-hull of the polar plot of the reciprocal surface energy, the MERR principle appears to rely on local maximization, as also suggested in Takei et al. (2013). We are planning further studies to closely examine these issues.

To formulate the phase-field model for strongly anisotropic fracture, we have com-

bined the classical variational phase-field model of brittle fracture (Bourdin et al., 2000) with the extended Cahn-Hilliard (ECH) framework (Abinandanan and Haider, 2001; Torabi and Lowengrub, 2012), proposed in the context of phase-field models of crystal growth. The result is a fourth-order model, since the energy functional involves the Hessian of the phase-field. Consequently, its numerical implementation by direct Galerkin methods requires smooth basis functions. Here, we resort to local maximum entropy approximants, a family of smooth meshfree basis functions. We present a selected set of numerical examples that illustrate the main features of strongly anisotropic crack propagations. Our results reproduce many of the experimental observations in Takei et al. (2013).

Chapter 3

Tearing of brittle thin sheets

3.1 Introduction

Thin elastic sheets are very common in nature and technology. Tearing refers to the situation in which cracks propagate in a thin sheet driven by out-of-plane loading (mode III). Tearing a thin sheet is a very common experience in our daily life as we peel a piece of fruit or open a package. Classical fracture mechanics has been successful in predicting crack propagation in bulk brittle materials invoking various crack path selection criteria reviewed in Chapter 1. However, this theory is challenged by the tearing of thin sheets (Takei et al., 2013; Roman, 2013).

There have been previous studies examining the stress field around linear elastic thin plates (Williams, 1961; Sih et al., 1962; Zehnder and Viz, 2005), identifying two additional stress intensity factors (SIFs) and stronger $r^{-3/2}$ singularities in the out-of-plane shear. However, since tearing typically involves large geometric nonlinearity (Hamm et al., 2008; Bayart et al., 2010, 2011; Kruglova et al., 2011; Takei et al., 2013; Roman, 2013), it is not clear whether the crack tip fields of the linear theory, and hence the SIFs, are meaningful (Hui et al., 1998) or if and how they determine crack propagation (Cohen and Procaccia, 2010). For instance, the proper generalization of the principle of local symmetry is not clear in a setting with four SIFs (Roman, 2013).

The interplay between geometry, surface energy, stretching and bending deformation leads to non-trivial and rich behaviors (Bayart et al., 2010, 2011; Takei et al.,

2013; Brau, 2014), particularly when the thin film is adhesively coupled to a flat (Hamm et al., 2008) or curved (Kruglova et al., 2011) substrate. The complexity of these problems restricts analytical approximate solutions to very simplified settings and specific parameter regimes (Hamm et al., 2008; Roman, 2013; Brau, 2014). Simple energetic models in these references have been remarkably successful in explaining almost quantitatively nontrivial observations such as the dependence of crack path on interfacial adhesion (Hamm et al., 2008; Roman, 2013) or on peeling angle (Bayart et al., 2011; Roman, 2013; Brau, 2014). However, a general modeling approach to tearing, capable of examining in detail the mechanics of tearing as probed in experiments or of exploring new physics has been lacking.

The success of energetic simple models suggests that variational theories of brittle fracture may provide a unifying and general framework extending from bulk brittle fracture to materials with strongly anisotropic surface energy (Chapter 2) or to thin elastic sheets.

To explore tearing of thin films, we develop next a model and a computational framework coupling elasticity (stretching and bending), fracture, and adhesion to a substrate. We consider a geometrically exact model, see Section 3.2. The fracture of brittle thin sheets is modeled using the variational approach to fracture (Bourdin et al., 2008). The delamination of thin sheets adhered to substrates is modeled with a cohesive model (Xu and Needleman, 1994). We numerically implement the model with subdivision surface finite elements (Cirak et al., 2000), see Section 3.3, show a gallery of representative simulations capturing nontrivial observations in Section 3.4, and collect our final remarks and conclusions in Section 3.5.

3.2 Theoretical model

3.2.1 Nonlinearly elastic model of thin sheets

We model thin elastic sheets with a geometrically exact nonlinear thin shell formulation sometimes referred to as the nonlinear Koiter shell model (Ciarlet, 2005). This

model is based on the Kirchhoff–Love kinematical assumption, which states that the material line orthogonal to the middle surface in the undeformed configuration remains straight, unstretched and orthogonal to the middle surface during deformation. We provide below a succinct description of this theory. More details can be found in Ciarlet (2005) or in Millán et al. (2011, 2013) and references therein.

We follow the usual convention for Latin and Greek indices, referring to Cartesian and curvilinear coordinates, respectively (i.e. $i = 1, 2, 3$; $\alpha = 1, 2$). A comma before an index denotes partialial differentiation, subscripts refer to covariant components, and superscripts denote contravariant components. We parametrize the middle surface of a shell Ω using $\boldsymbol{\varphi}$, a mapping from the parametric space $\mathscr{A} \subset \mathbb{R}^2$ into $\mathbb{R}^3$. Let $\boldsymbol{t}$ be a field of unit vectors (a field of directors). The pair $(\boldsymbol{\varphi}, \boldsymbol{t})$ then describes a configuration of the shell as a three dimensional object through the mapping

$$\boldsymbol{\Phi}(\boldsymbol{\xi}) = \boldsymbol{\varphi}\left(\xi^1, \xi^2\right) + \xi\, \boldsymbol{t}\left(\xi^1, \xi^2\right), \tag{3.1}$$

where $\boldsymbol{\xi} = \{\xi^1, \xi^2, \xi^3\}$ and $\xi = \xi^3$. See Figure 3.1 for an illustration. Assuming that the thickness is uniform, this mapping takes values in the referential body $\mathscr{A} \times [-t/2, t/2]$ and defines the current configuration of the shell

$$\mathscr{S} = \left\{ \boldsymbol{x} \in \mathbb{R}^3 |\ \boldsymbol{x} = \boldsymbol{\Phi}(\boldsymbol{\xi}),\ \ -\frac{t}{2} \leq \xi \leq \frac{t}{2},\ \ \left(\xi^1, \xi^2\right) \in \mathscr{A} \right\}. \tag{3.2}$$

The area element of the middle surface can be computed as $d\Omega = \bar{j}\ d\xi^1 d\xi^2$, where $\bar{j} = |\boldsymbol{\varphi}_{,1} \times \boldsymbol{\varphi}_{,2}|$.

Denoting by $\{\boldsymbol{E}_k\}$ the basis vectors of the Cartesian coordinates $\{\xi^1, \xi^2, \xi^3\}$ in the reference configuration, the derivative of the configuration mapping can be written as

$$D\Phi = \frac{\partial \boldsymbol{\Phi}}{\partial \xi^i} \otimes \boldsymbol{E}^i = \boldsymbol{g}_i \otimes \boldsymbol{E}^i, \tag{3.3}$$

where $\boldsymbol{g}_\alpha = \frac{\partial \boldsymbol{\Phi}}{\partial \xi^\alpha} = \boldsymbol{\varphi}_{,\alpha} + \xi\, \boldsymbol{t}_{,\alpha}$ and $\boldsymbol{g}_3 = \frac{\partial \boldsymbol{\Phi}}{\partial \xi} = \boldsymbol{t}$ are sometimes referred to as the convective basis vectors of the deformed configuration. The covariant components of
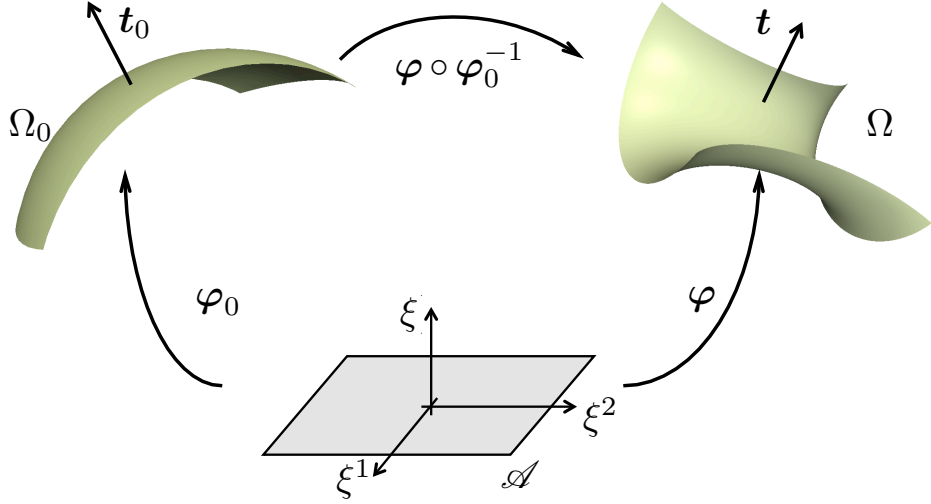
Figure 3.1: Reference, deformed and parametric configurations of the middle surface of thin shell.

the metric tensor in convected coordinates are given by $g_{ij} = \boldsymbol{g}_i \cdot \boldsymbol{g}_j$.

We have described so far a general deformed configuration using a mapping from a reference body. To define deformation we compare a deformed configuration with a specific configuration, called undeformed configuration. The subscript 0 denotes quantities in this undeformed configuration of the thin object; for instance $\boldsymbol{\varphi}_0$ parametrizes the undeformed middle surface. Local deformation measured by the Green–Lagrange strain tensor is then expressed in terms of the difference between the metric tensors of the undeformed and deformed configurations of the shell, i.e.

$$E_{ij} = \frac{1}{2}\left(g_{ij} - g_{0ij}\right) = \frac{1}{2}(\boldsymbol{\Phi}_{,i} \cdot \boldsymbol{\Phi}_{,j} - \boldsymbol{\Phi}_{0,i} \cdot \boldsymbol{\Phi}_{0,j}). \tag{3.4}$$

According to the Kirchhoff–Love kinematical assumptions of thin shells, we constrain the deformed director $\boldsymbol{t}$ to coincide with the unit normal of the deformed middle surface of the shell, i.e.

$$\boldsymbol{t} = \frac{\boldsymbol{\varphi}_{,1} \times \boldsymbol{\varphi}_{,2}}{\bar{\jmath}}, \quad \boldsymbol{\varphi}_{,\alpha} \cdot \boldsymbol{t} = 0, \quad |\boldsymbol{t}| = 1, \quad \boldsymbol{t} \cdot \boldsymbol{t}_{,\alpha} = 0. \tag{3.5}$$

With the Kirchhoff–Love kinematic assumption, which is well suited when the ratio

39

between the shell thickness and its characteristic lateral dimension is $\ll 1$, the only non-zero contributions to the Green–Lagrange strain tensor retained up to first order in t are

$$E_{\alpha\beta} \;= \varepsilon_{\alpha\beta} + \xi\; \rho_{\alpha\beta}, \tag{3.6}$$

where $\varepsilon_{\alpha\beta} = \frac{1}{2}(\boldsymbol{\varphi}_{,\alpha} \cdot \boldsymbol{\varphi}_{,\beta} - \boldsymbol{\varphi}_{0,\alpha} \cdot \boldsymbol{\varphi}_{0,\beta})$ is the membrane strain tensor and $\rho_{\alpha\beta} = \boldsymbol{\varphi}_{,\alpha} \cdot \boldsymbol{t}_{,\beta} - \boldsymbol{\varphi}_{0,\alpha} \cdot \boldsymbol{t}_{0,\beta}$ is the bending strain tensor. It is clear that $\varepsilon_{\alpha\beta}$ measures changes in the in-plane metric tensor or first fundamental form. Similarly, $\rho_{\alpha\beta}$ measures changes in second fundamental form (Do Carmo, 1976).

Thus, Kirchhoff–Love kinematical assumption leads to a thin shell model where strain is expressed exclusively in terms of the kinematics of the middle surface. Therefore, for an elastic shell the strain energy is a functional of the deformed configuration mapping $\boldsymbol{\varphi}$ only, and can be written in terms of the strain energy density per unit undeformed W as

$$\Pi_{\texttt{ela}}[\boldsymbol{\varphi}] = \int_{\Omega_0} W(\boldsymbol{\varepsilon}, \boldsymbol{\rho}) \; d\Omega_0, \tag{3.7}$$

where Ω_0 is the reference middle surface of the thin shell. Generally, geometric non-linearity is much more important than material nonlinearity in the mechanics of thin shells. For this reason, we consider a simple isotropic Kirchhoff–St. Venant elastic material model, whose strain energy density is

$$W(\boldsymbol{\varepsilon}, \boldsymbol{\rho}) = \frac{1}{2}\mathbb{C}^{\alpha\beta\gamma\delta}\left(t\, \varepsilon_{\alpha\beta}\varepsilon_{\gamma\delta} + \frac{t^3}{12}\rho_{\alpha\beta}\rho_{\gamma\delta} \right), \tag{3.8}$$

with

$$\mathbb{C}^{\alpha\beta\gamma\delta} = \frac{E}{(1-\nu^2)}\left[\nu a_0^{\alpha\beta} a_0^{\gamma\delta} + \frac{1}{2}(1-\nu)\left(a_0^{\alpha\gamma} a_0^{\beta\delta} + a_0^{\alpha\delta} a_0^{\beta\gamma} \right) \right], \tag{3.9}$$

where $(a_0)_{\alpha\beta} = \boldsymbol{\varphi}_{0,\alpha} \cdot \boldsymbol{\varphi}_{0,\beta}$ are the convected components of the metric tensor, $a_0^{\alpha\gamma}(a_0)_{\gamma\beta} = \delta^\alpha_\beta$, E is the Young's modulus and ν is the Poisson's ratio.

The membrane and bending stress resultants in this theory are given by

$$
\begin{aligned}
n^{\alpha\beta} &= \frac{\partial W}{\partial \varepsilon_{\alpha\beta}} = t\, \mathbb{C}^{\alpha\beta\gamma\delta}\varepsilon_{\gamma\delta}, \\
m^{\alpha\beta} &= \frac{\partial W}{\partial \rho_{\alpha\beta}} = \frac{t^3}{12}\mathbb{C}^{\alpha\beta\gamma\delta}\rho_{\gamma\delta},
\end{aligned}
\tag{3.10}
$$

In the numerical implementation, it is convenient to resort to Voigt's notation, denoted by $\{\cdot\}$, which exploits the symmetry of the tensors involved in the theory. With this notation, we have

$$
\{\boldsymbol{n}\} = \begin{pmatrix} n^{11} \\ n^{22} \\ n^{12} \end{pmatrix} = t\{\mathbb{C}\}\{\boldsymbol{\varepsilon}\}, \quad \{\boldsymbol{m}\} = \begin{pmatrix} m^{11} \\ m^{22} \\ m^{12} \end{pmatrix} = \frac{t^3}{12}\{\mathbb{C}\}\{\boldsymbol{\rho}\},
\tag{3.11}
$$

$$
\{\boldsymbol{\varepsilon}\} = \begin{pmatrix} \varepsilon_{11} \\ \varepsilon_{22} \\ 2\varepsilon_{12} \end{pmatrix}, \quad \{\boldsymbol{\rho}\} = \begin{pmatrix} \rho_{11} \\ \rho_{22} \\ 2\rho_{12} \end{pmatrix},
\tag{3.12}
$$

and

$$
\{\mathbb{C}\} = \frac{E}{1-\nu^2} \begin{pmatrix} (a_0^{11})^2 & \nu a_0^{11} a_0^{22} + (1-\nu)(a_0^{12})^2 & a_0^{11} a_0^{12} \\ & (a_0^{22})^2 & a_0^{22} a_0^{12} \\ symm & & \frac{1}{2}\left[(1-\nu)a_0^{11} a_0^{22} + (1+\nu)(a_0^{12})^2\right] \end{pmatrix}.
\tag{3.13}
$$

Using this notation and referring the integral to the referential domain, the elastic energy can be written as

$$
\Pi_{\mathtt{ela}}[\boldsymbol{\varphi}] = \int_{\mathscr{A}} \frac{1}{2}\left(t\{\boldsymbol{\varepsilon}\}^T\{\mathbb{C}\}\{\boldsymbol{\varepsilon}\} + \frac{t^3}{12}\{\boldsymbol{\rho}\}^T\{\mathbb{C}\}\{\boldsymbol{\rho}\}\right)\bar{j}_0\ d\xi^1 d\xi^2.
\tag{3.14}
$$

3.2.2 Phase-field approximation of brittle fracture

In the variational approach to brittle fracture proposed by Francfort and Marigo (1998), the crack initiation and quasi-static evolution are the natural results of the minimization of a Griffith-like energy functional defined as the sum of the elastic energy and the surface energy of the cracked body. The minimization has to be taken among all the kinematically admissible displacements and admissible crack sets, and subjects to Dirichlet boundary conditions and an irreversibility condition to avoid unphysical healing of cracks. This theory has been subsequently regularized into a phase-field or gradient damage models, suitable for numerical calculations (Bourdin et al., 2000; Bourdin, 2007; Bourdin et al., 2008), and which converge to the sharp variational theory of brittle fracture (Bourdin et al., 2008). These and related models (Pham et al., 2011; Pham and Marigo, 2013) have been studied in detail in bulk materials and only barely explored in thin shells (Amiri et al., 2014).

In the regularized approximation of brittle fracture, cracks are represented by a phase-field variable (scalar order parameter) ϕ, which is 0 inside a cracked zone, 1 away from the crack, and changes from 0 to 1 smoothly. In the present setting, we choose to describe ϕ as a field on the middle surface of the undeformed shell Ω_0 only, implicitly assuming that the phase-field is constant across the thickness of thin sheet. Physically, this means that our model rules out partial cracking through the thickness, which is reasonable to model very thin shells, but may not be adequate for thicker shells progressively cracking under bending. The model cannot resolve effects that may depend on the structure of the crack front though-the-thickness. Despite these potential limitations, we will explore such a model, where the phase-field couples to the elastic energy through the modified elastic energy functional

$$\Pi_{\texttt{ela}}[\boldsymbol{\varphi}, \phi] = \int_{\Omega_0} \phi^2 W(\boldsymbol{\varepsilon}, \boldsymbol{\rho}) \, d\Omega_0. \tag{3.15}$$

The other ingredient in a phase-field model of brittle fracture is a functional depending on ϕ approximating the crack length. In a finite deformation setting, it is natural to consider the length of the crack in the undeformed configuration. We consider here

a recently proposed higher-order phase-field model (Borden et al., 2014), which here needs to be formulated in the curved two-dimensional middle surface of the thin shell in its undeformed configuration as

$$\Pi_{\mathtt{frac}}[\phi] = \int_{\Omega_0} G_{\mathtt{c}} t \left[\frac{(\phi - 1)^2}{4\kappa} + \frac{\kappa}{2} |\nabla_{\mathtt{s}}\phi|^2 + \frac{\kappa^3}{4} (\Delta_{\mathtt{s}}\phi)^2 \right] \ d\Omega_0, \qquad (3.16)$$

where $G_{\mathtt{c}}$ is the critical energy release rate and $\nabla_{\mathtt{s}}$ and $\Delta_{\mathtt{s}}$ are the surface gradient and Laplacian operators in the undeformed middle surface. The metric tensor of this surface is given by $a_{\alpha\beta} = \boldsymbol{\varphi}_{0,\alpha} \cdot \boldsymbol{\varphi}_{0,\beta}$ and its contravariant components are given by the relation $a^{\alpha\gamma} a_{\gamma\beta} = \delta_\beta^\alpha$. Then, the expressions involving surface operators can be computed from

$$|\nabla_{\mathtt{s}}\phi|^2 = a^{\alpha\beta} \phi_{,\alpha} \phi_{,\beta}, \qquad (3.17)$$

and

$$\Delta_{\mathtt{s}}\phi = a^{\alpha\beta} \phi_{,\alpha\beta} - a^{\alpha\beta} \phi_{,\gamma} \Gamma_{\alpha\beta}^\gamma, \qquad (3.18)$$

where the comma denotes partial differentiation and

$$\Gamma_{\alpha\beta}^\gamma = \frac{a^{\gamma\mu}}{2} \left(\frac{\partial a_{\alpha\mu}}{\partial \xi^\beta} + \frac{\partial a_{\beta\mu}}{\partial \xi^\alpha} - \frac{\partial a_{\alpha\beta}}{\partial \xi^\mu} \right), \qquad (3.19)$$

are the Christoffel symbols of the second kind (Marsden and Hughes, 1983).

The regularization parameter κ has units of length and dictates the width of the smeared crack. A finite value of κ is necessary for the numerical simulations and needs to be resolved by the mesh. Although the convergence of this higher-order model to Griffith's fracture theory has not yet been established, numerical investigations have provided evidence that the fourth-order model possesses better accuracy and convergence rates for computationally practical choices of κ (Amiri et al., 2015). It is noteworthy that this fourth-order model is a particular instance of the extended Cahn-Hilliard model for fracture developed in Chapter 2 (Li et al., 2015).

Besides the advantages of the fourth-order phase-field model of fracture mentioned above, our main motivation is computational. Since we rely on the Kirchhoff-Love

theory of shells, the governing equations are fourth-oder in the deformation of the shell, which we address with smooth subdivision spline-like approximants. As shown in Borden et al. (2014); Amiri et al. (2015), discretizing the second-order phase-field model of fracture with smooth approximants leads to poor convergence. Thus, to treat both the phase-field and the thin shell parts of the model with subdivision approximants on an equal footing, a natural choice is to resort to the fourth-order phase-field model of fracture.

3.2.3   Adhesion energy between a thin sheet and a substrate

We model the adhesive interaction between thin shells and rigid substrates by cohesive zone model based on an exponential potential (Xu and Needleman, 1994). In this model, the adhesion energy is expressed as

$$\Pi_{\text{adh}}[\boldsymbol{\varphi}] = \int_{\Omega_0} \Phi_{\text{n}} \left[1 - \left(1 + \frac{\Delta_{\text{n}}}{\delta_{\text{n}}} \right) \exp \left(-\frac{\Delta_{\text{n}}}{\delta_{\text{n}}} - \frac{\Delta_{\text{t}}^2}{\delta_{\text{t}}^2} \right) \right] \, d\Omega_0, \qquad (3.20)$$

where the Φ_{n} is interfacial adhesion energy per unit area, and δ_{n} and δ_{t} are characteristic length-scales. The Δ_{n} and Δ_{t} are the normal and tangential components of the displacement jump across the interface. In this model, the total interfacial adhesion energy is independent of the decohesion mode. For a thin sheet adhered to a curved surface, Δ_{n} and Δ_{t} are computed by projecting the displacement of the middle surface $\boldsymbol{u} = \boldsymbol{\varphi} - \boldsymbol{\varphi}_0$ along the normal and tangential directions, $\Delta_{\text{n}} = \boldsymbol{u} \cdot \boldsymbol{n}$ and $\Delta_{\text{t}} = |\boldsymbol{u} - (\boldsymbol{u} \cdot \boldsymbol{n}) \, \boldsymbol{n}|$.

3.2.4 Phase-field model of fracture in brittle adhesive thin sheets

Collecting all the ingredients in the previous sections, the total energy of a possibly fractured adhesive thin sheets is

$$\Pi_{\texttt{tot}}[\boldsymbol{\varphi}, \phi] = \Pi_{\texttt{frac}}[\phi] + \Pi_{\texttt{ela}}[\boldsymbol{\varphi}, \phi] + \Pi_{\texttt{adh}}[\boldsymbol{\varphi}]. \tag{3.21}$$

The minimization of functional Eq.(3.21) with respect to both $\boldsymbol{\varphi}$ and ϕ, subject to Dirichlet boundary condition and to irreversibility of cracks provides a computable approximation of the generalized Griffith's brittle fracture model for geometrically nonlinear thin and adhesive shells.

3.3 Numerical implementation

Because the total energy involves second-order derivative of both the shell deformation $\boldsymbol{\varphi}$ and of the phase-field ϕ, a C^1 continuous approximation scheme is necessary to apply a straightforward Galerkin discretization approach. In Chapter 2, we resorted to smooth meshfree basis functions. Here, we use subdivision surface finite elements (Cirak et al., 2000; Cirak and Ortiz, 2001; Cirak and Long, 2011) to approximate the deformation $\boldsymbol{\varphi}$ and the phase-field ϕ. We follow a total Lagrangian approach, with the same parameter space and basis functions for the undeformed and deformed configurations. Let $\boldsymbol{\varphi}_0$ be the undeformed configuration mapping of the middle surface, defined over the parametric space $\mathcal{A}$. It is numerically represented as

$$\boldsymbol{\varphi}_0(\xi^1, \xi^2) = \sum_{a=1}^{\mathcal{N}} B_a(\xi^1, \xi^2) \, \boldsymbol{\varphi}_{0a}, \tag{3.22}$$

where $B_a(\xi^1, \xi^2)$ are subdivision surfaces basis functions, $\mathcal{N}$ is the number of nodes in the mesh, and $\boldsymbol{\varphi}_{0a}$ is the position in three-dimensional space of the $a-$th control point

defining the undeformed shell middle surface. Similarly, the deformed configuration and the phase field are discretized as

$$\boldsymbol{\varphi}(\xi^1, \xi^2) = \sum_{a=1}^{\mathcal{N}} B_a(\xi^1, \xi^2) \, \boldsymbol{\varphi}_a, \tag{3.23}$$

and

$$\phi(\xi^1, \xi^2) = \sum_{a=1}^{\mathcal{N}} B_a(\xi^1, \xi^2) \, \phi_a. \tag{3.24}$$

Inserting Eqs. (3.23,3.24) into Eq. (3.21), we obtain a total energy function depending on nodal variables $\boldsymbol{\varphi}_a$ and ϕ_a, $a = 1, 2, \ldots, \mathcal{N}$. We minimize this energy with respect to deformation and phase field degrees of freedom following the alternate minimization algorithm developed in (Bourdin, 2007; Bourdin et al., 2008). At each load increment, the energy is first minimized with respect to $\boldsymbol{\varphi}_a$ freezing the phase-field using Newton's method combined with line-search (Millán et al., 2013), and then minimized with respect to ϕ_a freezing the deformation, which results in a linear algebraic system. This procedure is iterated until convergence reached. We introduce the strain-history field following Miehe et al. (2010a) to enforce the irreversibility condition. We make sure that the phase-field profile is sufficiently resolved by the mesh, by requiring that the regularization length κ is large enough compared to the mesh size h (at least where cracks are expected to propagate). From extensive numerical test, we enforce the condition $\kappa \geqslant 2h$. Similarly, the discretization needs to resolve the cohesive lengths, which requires that $\delta_{\mathtt{n}} \geqslant 2h$ and $\delta_{\mathtt{t}} \geqslant 2h$.

3.4   Numerical Experiments

In this section, we consider numerical experiments split in two groups, depending on whether or not the brittle thin sheet is adhered to a substrate.
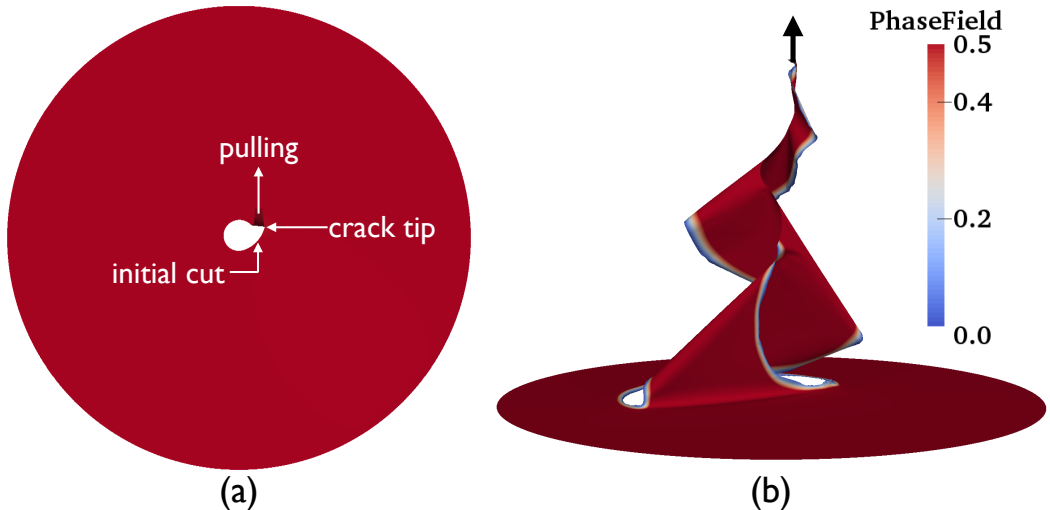
Figure 3.2: Spiral crack produced by pulling a flap of thin sheet.(a) The initial cut is tangent to the circular hole in the thin sheet and the flap is pulled vertically. (b) Deformed configuration obtained by the numerical simulation.

3.4.1 Tearing of thin sheet without adhesion

We first consider a setup by which a spiral crack is produced by pulling a flap perpendicularly to the thin sheet (Romero et al., 2013). We consider a annular thin sheet with traction-free boundary conditions in the circular hole located at the centre and clamped boundary conditions at the outer boundary of the annulus. A small flap is formed by an initial cut tangent to the circular hole. The flap is pulled vertically to propagate the crack, see Figure 3.2(a). The final deformation resulting from the spiral crack propagation is shown in Figure 3.2(b). The parameter space of the problem is characterized by four non-dimensional groups: ν, $R_{\mathrm{inn}}/R_{\mathrm{out}}$, t/R_{inn}, and Et/G_c, the latter two bearing more physical significance. In the calculations shown here, we considered $\nu = 0.4$, $R_{\mathrm{inn}}/R_{\mathrm{out}} = 0.1$, $t/R_{\mathrm{inn}} = 10^{-3}$, and $Et/G_c = 10^2$.

The fracture process is dictated by the competition between the elastic energy (bending and stretching) concentrated at the fold connecting the flap with the thin sheet and the fracture energy. The experiments performed by Romero et al. (2013) argued that the crack trajectories approximate a logarithmic spiral $r = r_0 \exp(\theta \cot \theta_0)$, r_0 being the distance between the origin and the crack tip of the initial cut, θ the angle
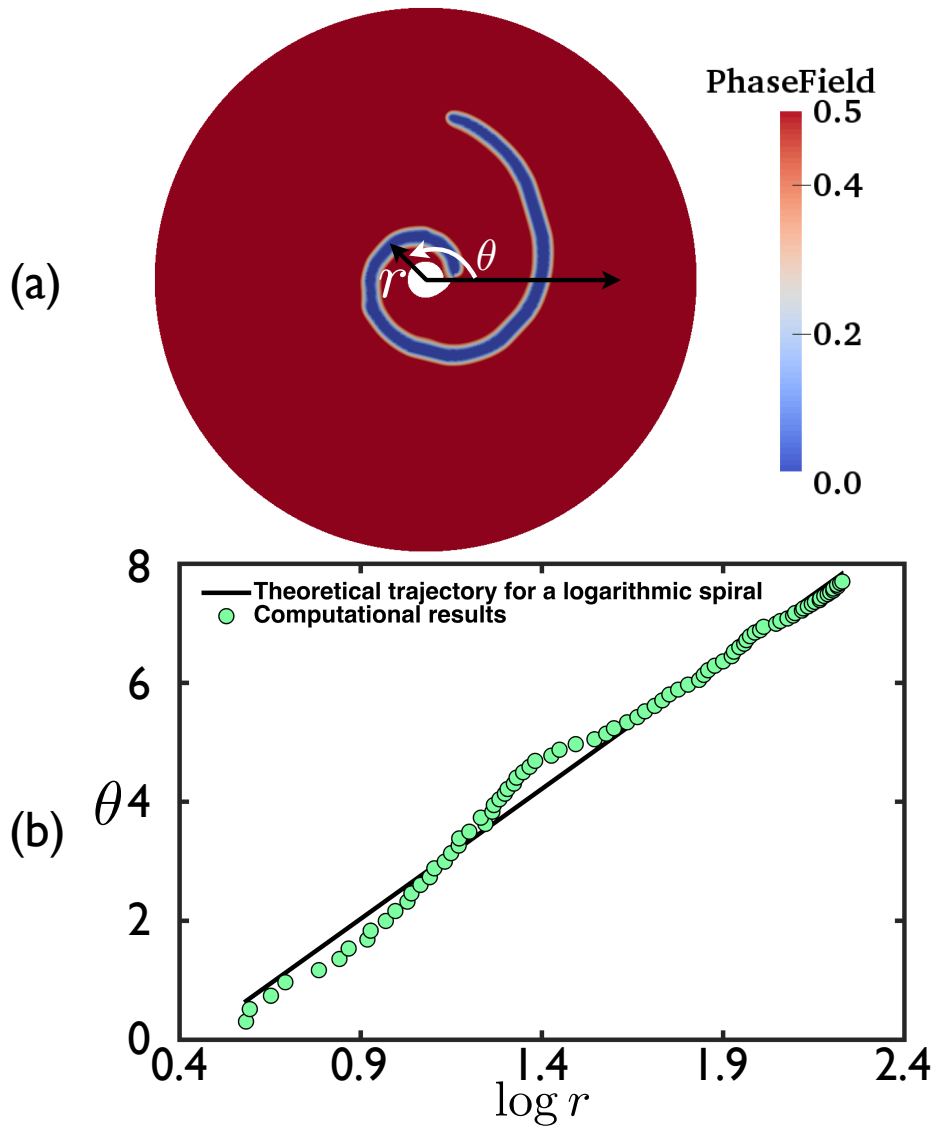
Figure 3.3: Spiral crack trajectory in the reference configuration. (a) Rotation angle θ of the spiral as a function of the radius r. (b) Semi-logarithmic plot of the crack trajectories.
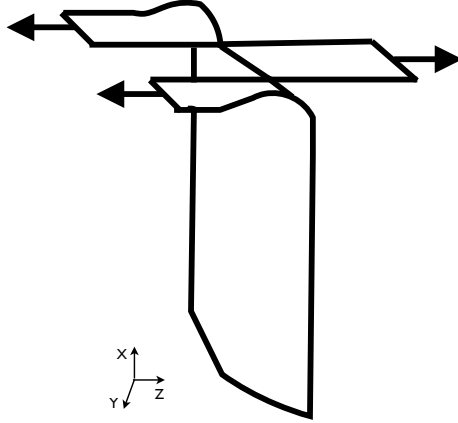
Figure 3.4: The schematic of trouser-like configuration, examined experimentally by Bayart et al. (2010, 2011). The thin sheet is pulled from the three flaps as shown by the arrows.

between the tangent and radial line at the point (r, θ), and θ_0 this angle at the initial cut. To test our theoretical model, we measure the spiral crack trajectories in polar co-ordinate (r, θ), see Figure 3.3(a), and plot $\theta(r)$ in Figure 3.3(b). The semi-logarithmic plot of Figure 3.3(b) shows that the crack path can be approximately described by a logarithmic spiral, consistent with the experiments. We believe that the deviation could be alleviated by numerical simulations with a finer mesh and smaller parameter κ. Furthermore, in the experiments reported in Romero et al. (2013) the parameters are such that $t/R_{\text{inn}} \approx 10^{-2}$ and $Et/G_c \approx 10$.

In the second numerical experiment we consider a long elastic thin sheet with two cracks positioned symmetrically and parallel to the centre axis of the sheet, thus creating three flaps at one end of the sheet. Then the flaps are torn apart as shown in Figure 3.4. The length and width of the thin sheet are denoted by L and W, while the initial width of the central flap is w_0. In the simulations, we consider $\nu = 0.3$, $L/W = 2.6$, $w_0/W = 0.3$, $t/w_0 = 6 \times 10^{-3}$ and $Ew_0/G_c = 10^3$. To prepare the initial configuration, we deform the three flaps to form a 90° angle with the rest of the sheet, and connect these flaps through cylindrical segments, see Figure 3.4. Then, the system is relaxed while the ends of the three flaps are fully constrained and the other end of the strip is constrained in the z direction. Then, to induce crack propagation,
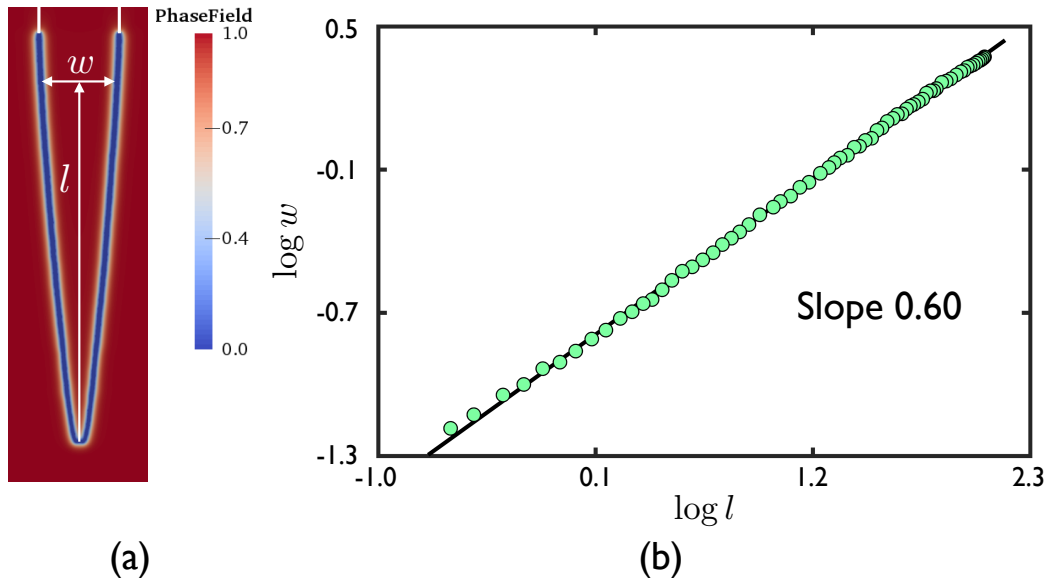
Figure 3.5: (a) As the convergent cracks develop, the inner flap develops a tongue-like shape. The crack is represented by phase-field. (b) Log-log plot of the width w of the centre flap as a function of the distance l to the tip defined by the merging point of the two crack.

the outer flaps are incrementally displaced in the $-z$ direction while the inner flap is displaced in the z direction. During this loading, all other degrees of freedom are constrained and the ends of the flaps and the z degrees of freedom are constrained along the bottom end of the strip.

Similarly to experimental observations, in our simulations the cracks converge as they propagate, eventually meeting and splitting the sheet into two parts. The inner flap detached from the rest of the sheet adopts a characteristic tongue-like shape as shown in Figure 3.5(a). We analyze the crack trajectory by measuring the width w of the inner flap as a function of the distance l to the tip of the tongue. We find that $w(l)$ follows a power law with exponent 0.60 as shown in the Figure 3.5(b). The exponent 0.60 is in very good agreement with the exponent 0.64 ± 0.06 measured experimentally (Bayart et al., 2010, 2011) and with the exponent $2/3$ predicted by a theoretical model by Brau (2014), which combines Griffith's criterion, the maximum energy release rate, and Euler's elastica to estimate the elastic energy.

In the third numerical experiment, we consider a peel-like experimental configura-
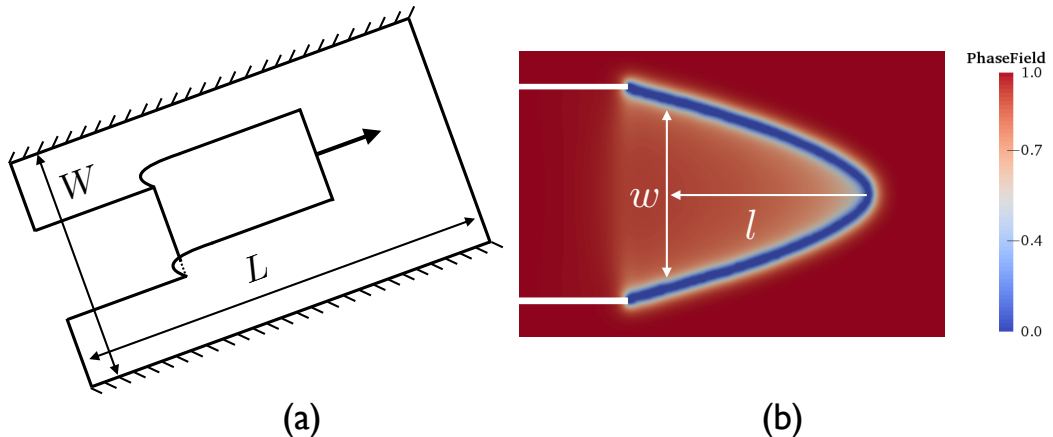
Figure 3.6: The schematic of peel-like experimental configuration and simulation result. (a) The rectangular thin sheet is clamped along its lateral boundary, the flap is pulled horizontally at constant displacement until it detached from the thin sheet. (b) The flap detaches from the thin sheet with a tongue-like shape (the crack is represented by the phase-field).

tion, with the same material and geometric parameters as in the previous experiment. A thin sheet is laterally clamped. Two parallel edge cracks are initially created parallel to the center axis of the sheet, creating a flap. Then, the flap is lifted and pulled as shown in Figure 3.6(a) to propagate the cracks. The material and geometrical parameters of thin sheet are exactly same as the second simulation. Similarly to the previous example, we prepare the initial configuration by displacing and rotating the flap so that it remains parallel to the undeformed sheet and by connecting the displaced flap to the rest of the sheet through a half-cylinder fold. Then this configuration is relaxed keeping the lateral boundaries and the end of the flap constrained. As the flap is pulled, the distance between the end of the flap and the planar sheet is kept constant.

Similarly to the previous example, the width of the flap decreases as the cracks propagate, eventually vanishing as the flap detaches from the thin sheet, see Figure 3.6(b). The final shape of the flap is qualitatively similar to the first simulation and can also be described by a power law of exponent 0.62 as shown in Figure 3.7(a). However, the exponent measured in experiments is 0.77±0.05 (Bayart et al., 2011; Roman, 2013) and is theoretically predicted to be 8/11 by Brau (2014) in the unstretchable limit,
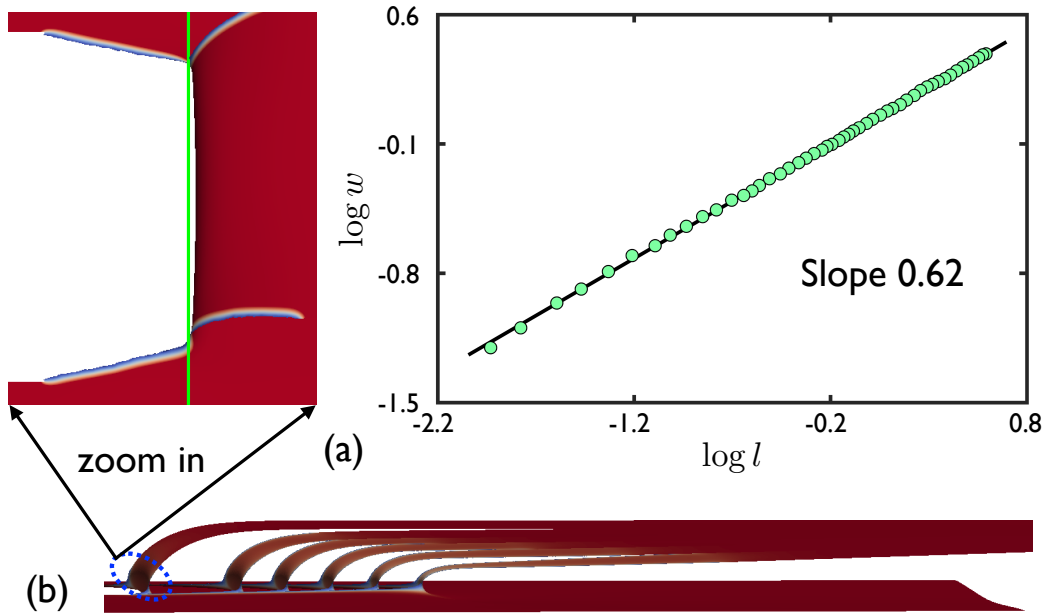
Figure 3.7: Log-log plot of the width w of the flap as a function of the distance l to the tip defined by the merging point of the two cracks (a). The snapshots from the simulation show that the pulling angle changes during crack propagation (b).

$Ew_0/G_c \gg 1$.

We attribute the large discrepancy between our results and the experiments to the pulling angle variation during our simulations, as illustrated in Figure 3.7(b). As clear from the figure, our simulation protocol did not precisely control the pulling angle to 180° during crack propagation. Closely examining the geometry of the ridge joining the flap to the sheet, we observe that at the onset and during crack propagation this ridge is doubly curved. This effect can be seen in the zoom-in inset in Figure 3.7(b). Thus, this ridge is necessarily stretched and resembles the stretching ridges characteristic of crumpling (Witten, 2007). Because the elastic energy of the stretching ridge, which determines the crack trajectory, is quite sensitive to the angle it subtends (Brau, 2014), our failure to control the pulling angle can result in significantly different crack paths. Furthermore, the parameter ranges in the experiments ($t/w_0 \approx 1.5 \cdot 10^{-3}$, $Ew_0/G_c \approx 2 \cdot 10^4$) differ from those used in the simulations.
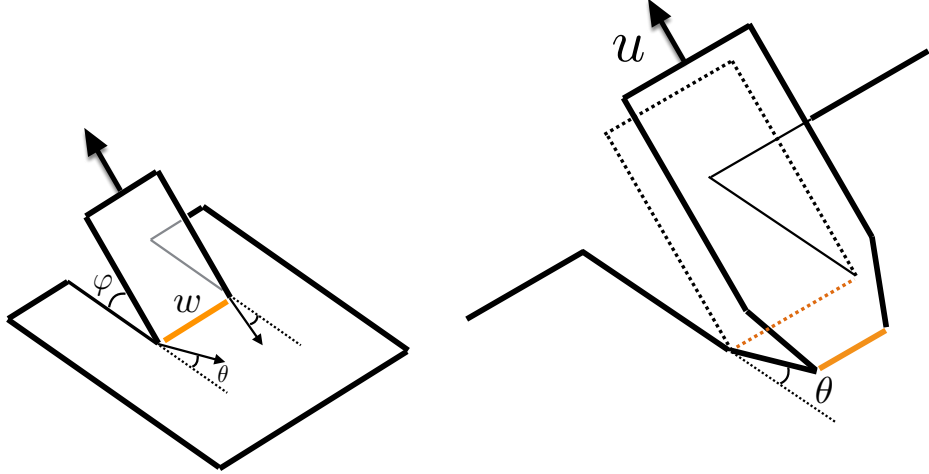
Figure 3.8: Schematic diagram of the tearing experiments of adhesive thin sheets on a flat substrate and of the geometrical parameters necessary to describe the shape of the tear.

3.4.2 Tearing thin sheets adhered to substrate

We consider now an elastic thin sheet adhered to a flat substrate, in which a rectangular flap is created by cutting two paralleled cracks on one end of its edges. Before launching the simulation, we first prescribe a cylindrical segment connecting the substrate to the flap, which form an angle of φ (see the Figure 3.8). The radius of curvature of the cylindrical segment is estimated as in Kruglova et al. (2011). Then, fixing the hight of the end of the flap, we relax the system. The initial length of the flap is long compared to the radius of curvature, minimizing any boundary effect. The flap is then pulled with fixed peeling angle φ, causing the initially parallel cracks to propagate inwards and the flap to progressively detach from the substrate. As in experiments, the two crack tips merge into a point, completely detaching the flap and leaving a perfectly triangular tear characterized by the angle θ.

In the limit $\Phi_{\mathtt{n}} w \gg G_c t$, the fold connecting the the flap and the adhered sheet is singly curved, its energy is purely due to bending, and can be modeled by the classical Euler elastica theory (Hamm et al., 2008; Roman, 2013). In this limit, following an energy method combining Griffith's theory with the maximum energy release rate path selection criterion, an analytical expression can be obtained for the crack path

53
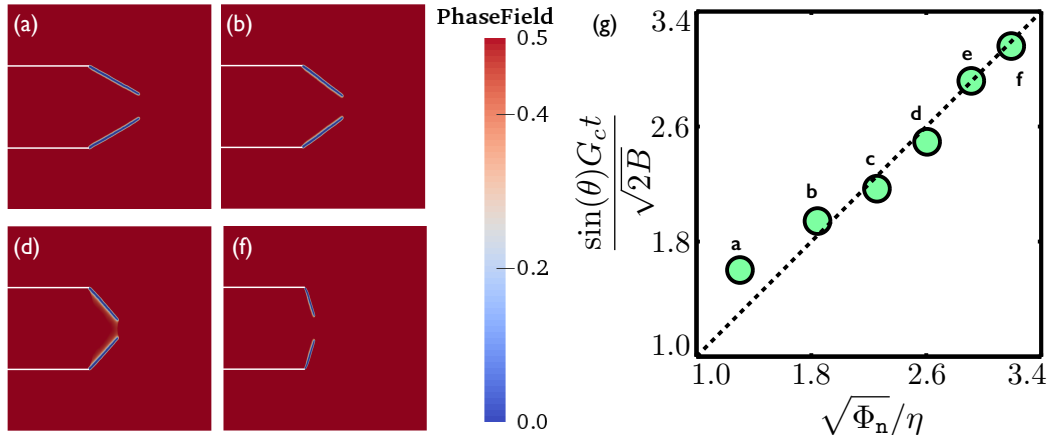
Figure 3.9: Crack paths for numerical experiments with different adhesion energy: (a) $\Phi_n = 0.5$, (b) $\Phi_n = 1.0$, (c) $\Phi_n = 1.5$, (d) $\Phi_n = 2.0$, (e). $\Phi_n = 2.5$, (f) $\Phi_n = 3.0$. The crack angle $\sin(\theta)G_c t/\sqrt{2B}$ versus $\sqrt{\Phi_n}/\eta$, with $\eta = 0.54$ (g).

angle as (Roman, 2013)

$$\sin\theta = \frac{\sqrt{2\Phi_n B}}{G_c t}\left[\frac{1 - \cos(\varphi/2)}{\sin(\varphi/2)}\right], \tag{3.25}$$

where $B = \frac{Et^3}{12(1-\nu^2)}$ is the bending rigidity of the elastic sheet. This equation shows that the triangular shape of the tear is determined by the material constants B, Φ_n and $G_c t$, and by the peeling angle φ. The case $\varphi = 180°$ was carefully studied experimentally and theoretically in Hamm et al. (2008), where B and $G_c t$ were varied. With our computational tool at hand, we can examine this relationship through numerical simulations. We chose in the simulations $E = 2 \cdot 10^5$, $\nu = 0.3$, $t = 10^{-3}$ and $w = 0.4$ in a square domain of unit lateral size.

Fixing peeling angle $\varphi = 180°$, we first perform simulations with different adhesion energies Φ_n and with fracture surface energy $G_c = 20$. In our simulations $\Phi_n w/(G_c t)$ ranges from 10 to 60. In Figure 3.9, we compare the simulation results with the theoretical predictions. We find a good agreement, in that the sine of the crack angle depends linearly with the square root of the adhesion energy, with a numerical factor η also needed to quantitatively explain experiments (Hamm et al., 2008). There is only a significant discrepancy for the lower value of Φ_n corresponding to $\Phi_n w/(G_c t) = 10$,
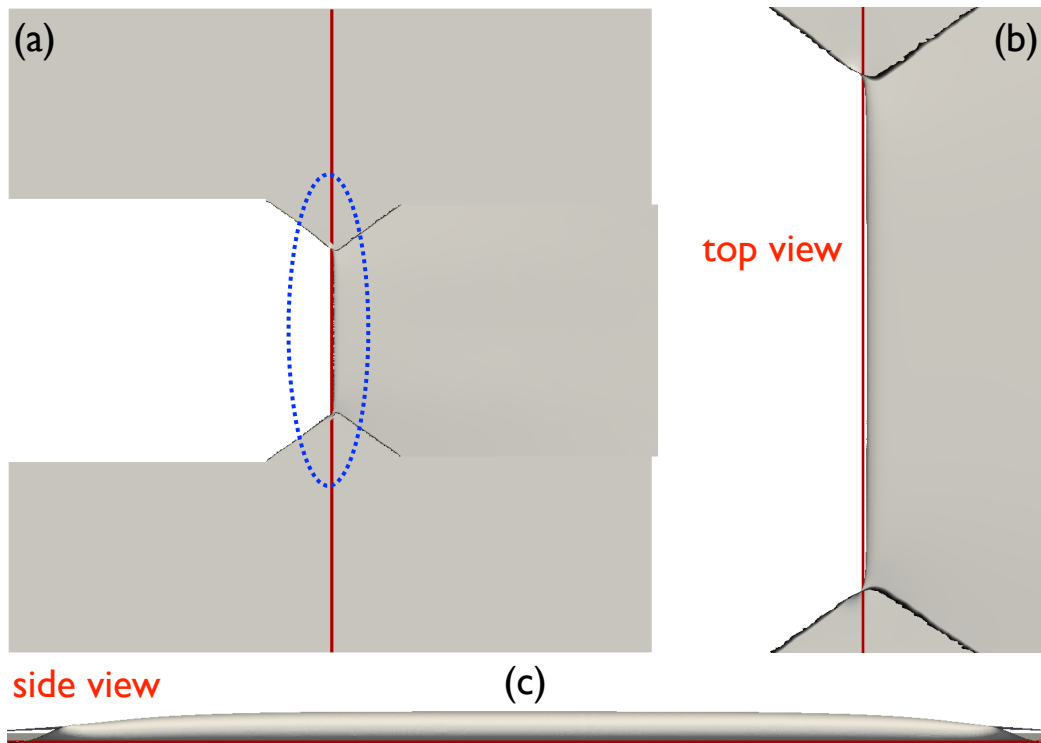
Figure 3.10: The connecting ridge shown for a peeling angle of $\varphi = 180°$ (a), top view of the connecting ridge (b), and side view of the connecting ridge (c). The double curvature of the ridge requires stretching. In this example, $\Phi_{\mathtt{n}} w/(G_c t) = 10$.
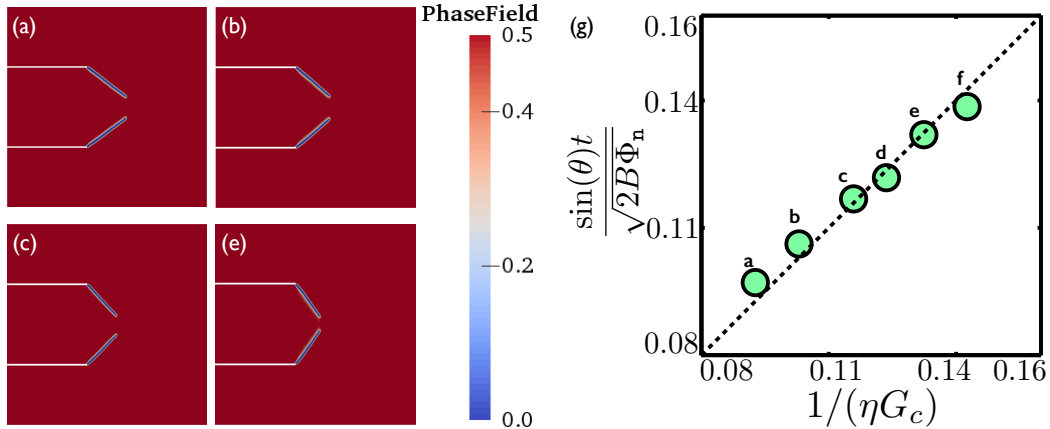
Figure 3.11: Crack paths for numerical experiments with different fracture energy: (a) $G_c = 20$, (b) $G_c = 18$, (c) $G_c = 16$, (d) $G_c = 15$, (e) $G_c = 14$, (f) $G_c = 13$. The crack angle $\sin(\theta)t/\sqrt{2B\Phi_\mathbf{n}}$ versus $1/(\eta G_c)$, with $\eta = 0.54$ (g).

which should be very large for Eq. (3.25) to be applicable. Indeed, as shown in Figure 3.10, in this case there is significant stretching in the connecting ridge, an effect not considered in the theory behind Eq. (3.25).

We perform next simulations with different fracture surface energy G_c and fixed $\Phi_\mathbf{n} = 1.0$. The simulation results show that the sine of the crack angle linearly depends on the reciprocal of fracture surface energy, as shown in the Figure 3.11. We also run the simulations with different peeling angles, fixing $\Phi_\mathbf{n} = 1.0$ and $G_c = 20$. The simulation results show that the sine of the crack angle linearly depends on $(1 - \cos(\varphi/2))/(\eta \sin(\varphi/2))$, as shown in the Figure 3.12. Here, the agreement is also good except for a peeling angle of $\varphi = 90°$. We hypothesize that a low peeling angles, the cohesive length-scale in Eq. (3.20) plays a significant role. In principle, this length-scale could be reduced even further, but at the cost of a finer mesh. In summary and despite these discrepancies, our simulation results show that the regularized variational model of fracture of thin elastic sheets essentially captures the behavior of teared thin sheet adhered on a flat substrate and is consistent with the theoretical expression in Eq. (3.25).

Experiments have shown that the geometry of the substrate can control the shape of the tears (Kruglova et al., 2011). The two crack paths in a pulled flap can either
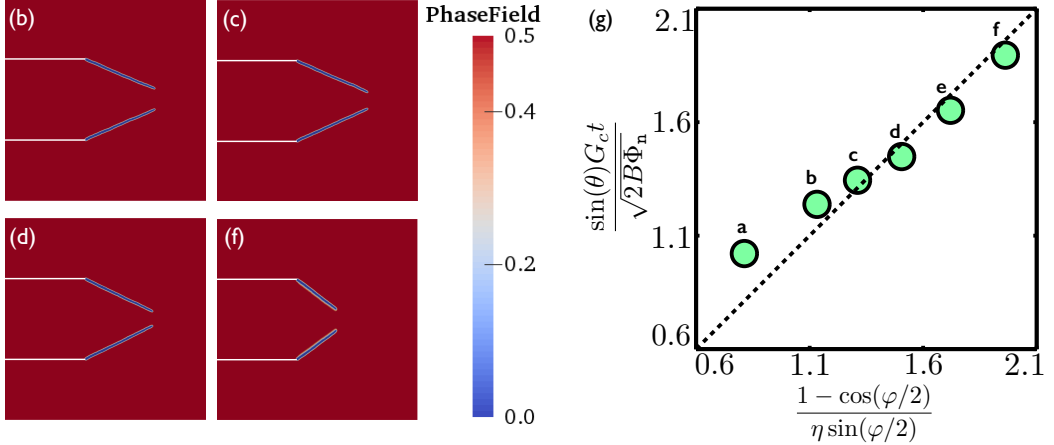
Figure 3.12: Crack paths for numerical experiments with different peeling angles: (a) $\varphi = 90°$, (b) $\varphi = 120°$, (c) $\varphi = 135°$, (d) $\varphi = 150°$, (e) $\varphi = 165°$, (f) $\varphi = 180°$,. The crack angle $\sin(\theta)G_c t/\sqrt{2B\Phi_{\mathrm{n}}}$ versus $(1 - \cos(\varphi/2))/(\eta\sin(\varphi/2))$, with $\eta = 0.51$ (g).

converge or diverge, depending on the curvature of a cylindrical substrate. We reproduce next the experiments of tearing thin sheets adhered on cylindrical substrates. The initial configurations used in the simulations are shown in Figure 3.13. Because these configurations necessarily involved stretching, the classical motifs of crumpling appear after relaxation, such as conical point features and stretching ridges. The flap is then pulled at constant peeling angle. The material and geometry parameters are chosen as $E = 4 \cdot 10^5$, $\nu = 0.3$, $G_c = 20$, $\Phi_{\mathrm{n}} = 1.0$, $t = 10^{-3}$, a cylinder radius of 0.29 and a width of the flap of $w = 0.2/w = 0.37$ for the negatively/positively curved substrate.

We first consider the negatively curved substrate an a peeling angle of $100°$. The simulation result shows that the initially parallel cracks converge and eventually the centre flap detaches from the substrate, as shown in the Figure 3.14. The positive curvature case with peeling angle of $70°$ leads to divergent cracks as shown in Figure 3.15. The convergent/divergent crack paths in the negatively/positively curved substrates observed in the simulations are in good agreement with the experimental observations by Kruglova et al. (2011). Furthermore, unlike the planar case, simulations and experiments show that the crack path significantly deviates from a straight path. To further examine the effect of substrate curvature on crack path, we performed simu-

57
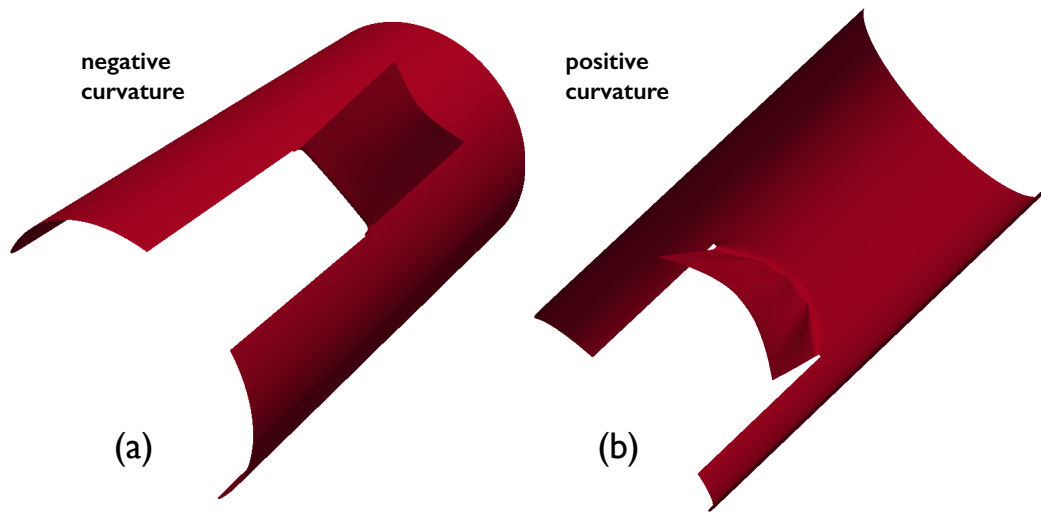
Figure 3.13: Tearing thin sheets adhered on cylinder substrate experiments. Tearing adhesive thin sheet on exterior side of a cylinder (negative curvature, a). Tearing adhesive thin sheet on the interior side of a cylinder (positive curvature, b).
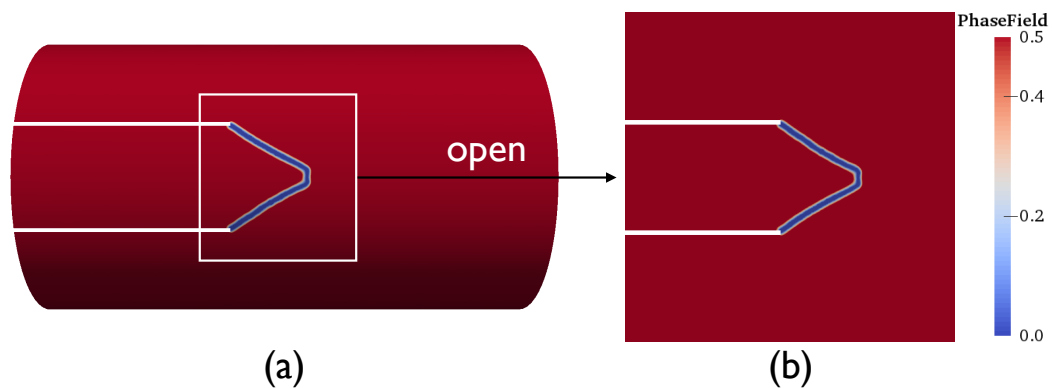
Figure 3.14: Tearing an adhesive thin sheet on the exterior side of a cylinder. Converging crack path on the undeformed cylindrical configuration (a) and on the "unrolled" undeformed configurations (b).
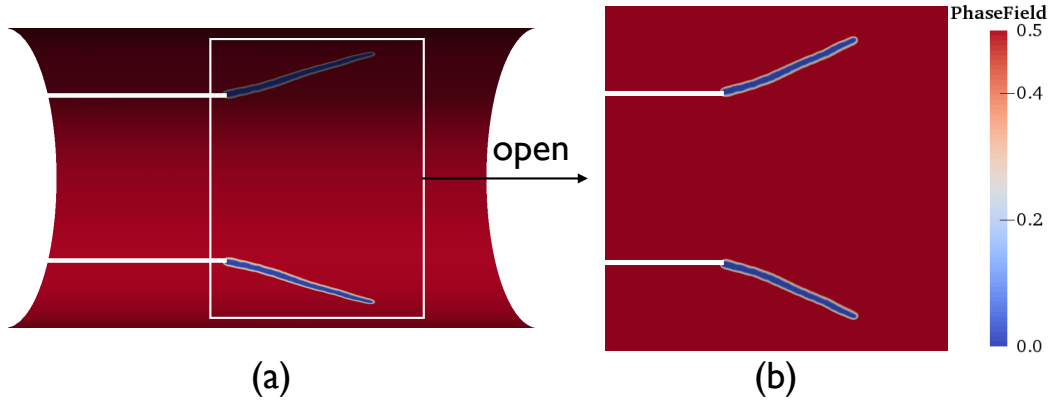
Figure 3.15: Tearing an adhesive thin sheet on the interior side of a cylinder. Diverging crack path on the undeformed cylindrical configuration (a) and on the "unrolled" undeformed configurations (b).

lations of spherical thin sheets adhered on spherical substrates, see Figure 3.16. We found that crack paths consistently followed "straight" paths, understood as geodesic curves of the sphere, suggesting that the deviations for cylindrical substrates could result from curvature anisotropy.

3.5   Conclusions

In this Chapter, we have developed a robust numerical strategy to simulate brittle fracture in thin elastic sheets accounting for geometric nonlinearity and adhesion to a substrate. We have simulated a wide variety of tearing experiments of thin sheets adhered to a substrate or not. Our simulations have reproduce the qualitative features of the crack paths, such as their power-law or logarithmic spiral geometry, as well as theoretical estimates for the crack path in adhered sheets. Taken together, our results show that the regularized variational approach to brittle fracture naturally generalizes to fracture in thin elastic sheets.

PhaseField
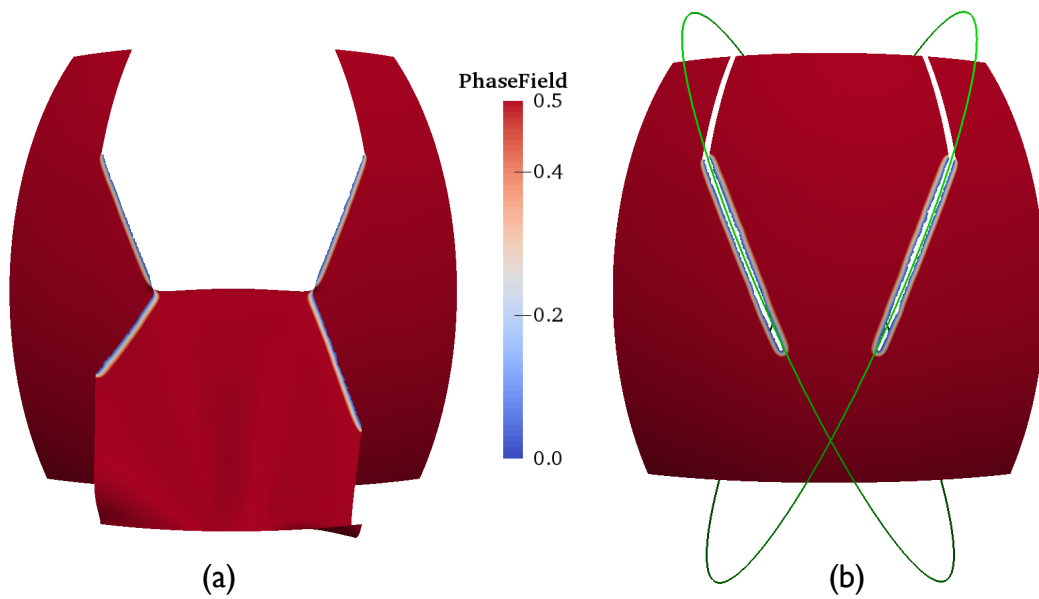
Figure 3.16: Tearing an adhesive thin sheet from the exterior side of a spherical substrate. Deformed configuration during tearing (a) and converging cracks closely following geodesic curves shown in green (b).

Chapter 4

Configurational forces for brittle thin shells

4.1 Introduction

Thin shells are ubiquitous in engineering structures, such as fuselages of airplanes, boat hulls, pressure vessels, or architectural domes. They are also prominent in biology. In most of these situations, shells are curved and fracture is a major failure mode. Fracture can also be a requirement for function, such as in packaging or for the ejection of seeds from seedpods (Deegan, 2012). In this chapter, we examine the influence of shell geometry on crack propagation.

Early theoretical studies on fracture in shallow thin shells showed that curvature reduced the resistance to fracture (Folias, 1969, 1970). In contrast, recent work has shown significantly enhanced effective toughness in sinusoidally corrugated graphene plates, where the out-of-plane shape disturbances were the result of patterned defects in the crystalline structure (Zhang et al., 2014). This work, however, could not discern the relative effect of geometry and defects on fracture.

Using the model and computational approach described in the previous chapter, we report in Figure 4.1 a selection of a phase-field simulations examining the effect on crack propagation of bump-like geometrical features in an otherwise planar plate with a pre-crack. In these simulations, the top and bottom boundaries of the plate

61
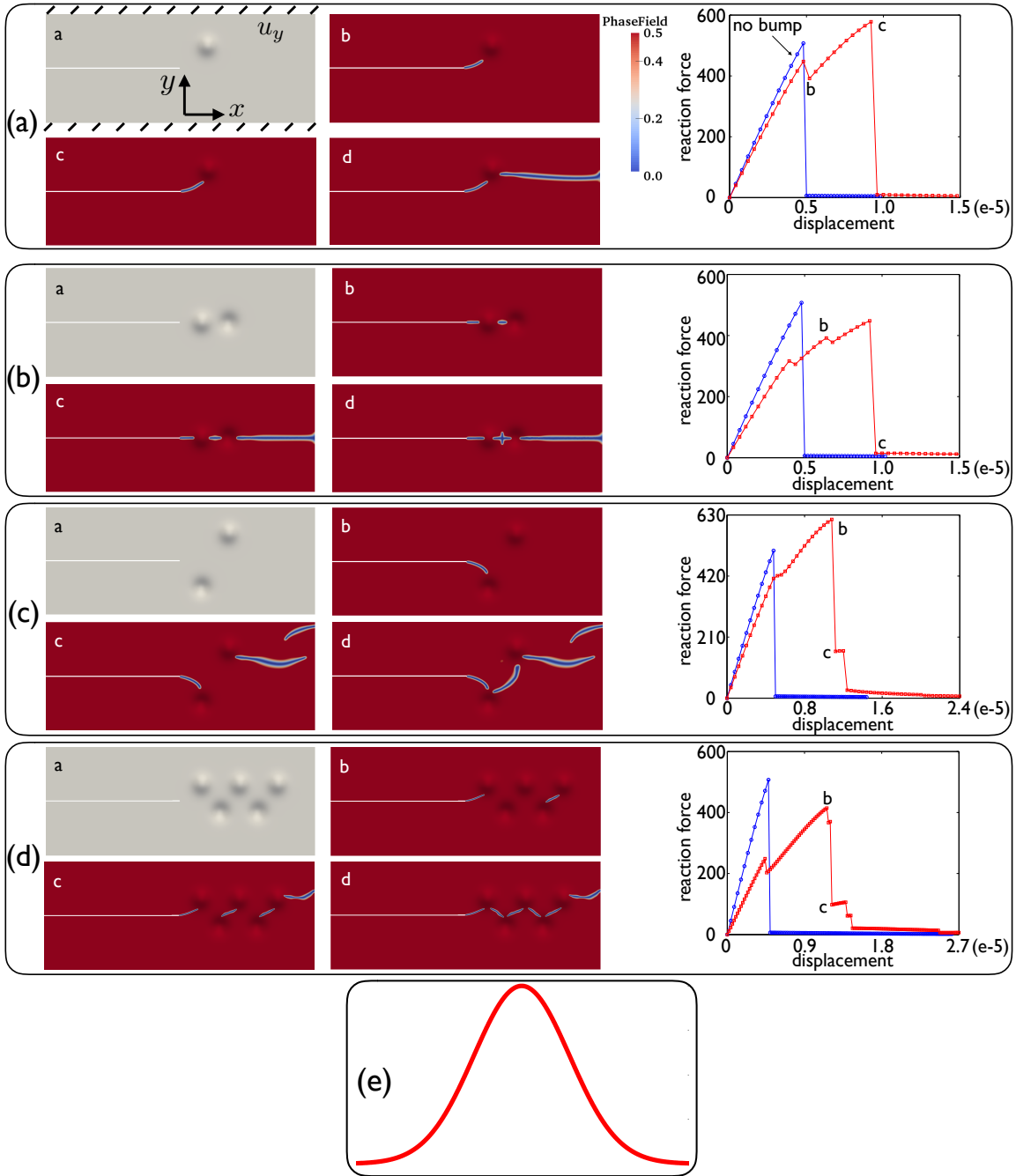
Figure 4.1: Phase-field simulations of crack propagation in linearly elastic thin Koiter plates containing a preexisting crack, in the presence of bump-like shape disturbances (left panels), and corresponding reaction force versus imposed displacement at the top and bottom boundaries (right panels). For reference, the force-displacement curve for a bump-free plate, where the crack propagates following a straight path, is shown in blue. The aspect ratio of the bumps is illustrated in (e).

are incrementally displaced in an opening mode. The figure shows that cracks are consistently attracted by bumps, but then arrested as they reach the periphery of the shape disturbance. The arrest can be physically understood because near a bump, the nominal in-plane tension can be locally relaxed by bending, which is energetically less costly, hence reducing the driving force for crack propagation (the energy release rate). In our simulations, subsequent crack propagation required nucleation of one or several new cracks, leading eventually to failure of the structure. Because the stress at which cracks nucleate increases as the phase-field parameter κ decreases (Borden et al., 2012), it is not clear if cracks could propagate through a bump if a smaller value of κ (requiring a finer mesh) was selected. In any case, simulations show that bumps first attract and then arrest cracks. At a structural level, the presence of the bumps slightly decreases the stiffness of the plate but considerably enhances the energy dissipation of failure (about three-fold) and even the ultimate load, as shown in the force-displacement curves. Furthermore, the arrangement of multiple upward or downward bumps significantly affects the crack patterns. Unlike circular perforations, bumps do not compromise the integrity of the shell as a barrier. Thus, these results suggest that the toughness and crack path in thin shells could be tuned by properly designed shape patterns.

Towards understanding the effect of geometry on fracture, we analyze in this chapter the energy release rate associated with crack extension, i.e. the driving force in brittle fracture. To compute this quantity, we resort to the method of configurational forces, interpreted as the relative variation of the total energy of a given system as some variable describing the configuration of that system changes (Gurtin, 2000; Kienzler and Herrmann, 2000). Physically, such variable could be the location of a dislocation or inclusion, the change in size or shape of a cavity, the extension of a crack or the change in location of a phase boundary in a material. The main advantage of the theory of configurational forces is that it provides a unified and systematic method to study microstructure evolution involving possibly multiple mechanisms. Configurational forces have been applied to fracture mechanics (Freund, 1972; Gurtin, 1979; Eischen and Herrmann, 1987; Gurtin and Podio-Guidugli, 1998; Gurtin, 2000; Kien-

63

zler and Herrmann, 2000), recovering the J-integral (Cherepanov, 1967; Rice, 1968) by which the energy release rate of a straight traction-free crack in an homogeneous material can be computed as a path-independent contour integral involving the Eshelby energy-momentum tensor. Recalling Noether's theorem, this path-independence is a consequence of translational symmetry. Because geometry breaks translation invariance (think of the bumps in the previous examples), we should not expect in general a path-independent J-integral in our setting. To our knowledge, the calculation of the energy release rate in general curved shells has not been fully addressed before, despite previous work such as Kienzler and Herrmann (2000) for Mindlin-Reissner linear thin shells.

We focus on the linear version of Koiter's theory of thin shells, which is briefly reviewed in Section 4.2. We then derive the configurational force field conjugate to a material rearrangement and identify the Eshelby tensor, as well as non-conservative contributions to the energy release rate associated with curvature in Section 4.3. Our approach is linear with respect to the shell deformation, but considers the full nonlinearity associated with shell geometry. Finally, in Section 4.4 we analyze with this theory the energy release rate of crack extension for a plate with a pre-crack and finite geometric disturbance, highlighting the new terms arising from the presence of the geometric feature.

4.2   The linear theory of Koiter thin shells

The Koiter thin shell model (Ciarlet, 2005; Chapelle and Bathe, 2010) is based on the Kirchhoff–Love kinematical assumption, which states that the material line orthogonal to the middle surface in the undeformed configuration remains straight, unstretched and always orthogonal to the middle surface during the deformations. We summarize next the formulation of this theory, focusing on its linearized version. For an asymptotic derivation of the theory, we refer readers to Ciarlet (2000).

As in the previous chapter, we denote the shell middle surface by Ω, which is parametrized by the mapping $\boldsymbol{\varphi} : \bar{\Omega} \longrightarrow \mathbb{R}^3$. We introduce the covariant basis vectors

tangent to the middle surface and the unit vector normal

$$\boldsymbol{a}_\alpha = \partial_\alpha \boldsymbol{\varphi} = \boldsymbol{\varphi}_{,\alpha}, \qquad \boldsymbol{a}_3 = \boldsymbol{n} = \frac{\boldsymbol{a}_1 \times \boldsymbol{a}_2}{|\boldsymbol{a}_1 \times \boldsymbol{a}_2|}, \tag{4.1}$$

where the comma in a subscript refers to partial differentiation. The "contravariant vectors" (one-forms) of the surface $\boldsymbol{a}^\alpha$ are defined by the duality relations $\boldsymbol{a}^\alpha \boldsymbol{a}_\beta = \delta_\beta^\alpha$. These bases allow us to express vector fields $\boldsymbol{v} = v^\alpha \boldsymbol{a}_\alpha$ and one-forms $\boldsymbol{f} = f_\alpha \boldsymbol{a}^\alpha$ in terms of their components.

The first and second fundamental forms of the middle surface are given by

$$a_{\alpha\beta} = \boldsymbol{a}_\alpha \cdot \boldsymbol{a}_\beta \quad \text{and} \quad b_{\alpha\beta} = \boldsymbol{n} \cdot \partial_\alpha \boldsymbol{a}_\beta = \boldsymbol{n} \cdot \boldsymbol{\varphi}_{,\alpha\beta}. \tag{4.2}$$

We denote the determinant of the coordinate expression of the metric tensor by $a = \det a_{\alpha\beta}$. The first fundamental form (the metric tensor of the surface) and its inverse $a^{\alpha\beta}$ satisfying $a^{\alpha\beta} a_{\beta\gamma} = \delta_\gamma^\alpha$ allow us to "lower indices" of a vector field $\boldsymbol{v}$ to get the components of a corresponding one-form $\boldsymbol{v}^\flat$, i.e. $v_\alpha = a_{\alpha\beta} v^\beta$, and also to "rise indices" of a one-form $\boldsymbol{f}$ to get the components of a corresponding vector field $\boldsymbol{f}^\sharp$, i.e. $f^\alpha = a^{\alpha\beta} f_\beta$.

The Christoffel symbols of the surface are denoted by $\Gamma_{\alpha\beta}^\sigma$, can be computed from the metric tensor as

$$\Gamma_{\alpha\beta}^\sigma = \frac{a^{\sigma\mu}}{2} \left(\frac{\partial a_{\alpha\mu}}{\partial \xi^\beta} + \frac{\partial a_{\beta\mu}}{\partial \xi^\alpha} - \frac{\partial a_{\alpha\beta}}{\partial \xi^\mu} \right), \tag{4.3}$$

and allow us to compute the partial derivatives of the basis vectors

$$\partial_\alpha \boldsymbol{a}_\beta = \Gamma_{\alpha\beta}^\sigma \boldsymbol{a}_\sigma + b_{\alpha\beta} \boldsymbol{n}, \quad \partial_\alpha \boldsymbol{a}^\beta = -\Gamma_{\alpha\sigma}^\beta \boldsymbol{a}^\sigma + b_\alpha^\beta \boldsymbol{n}, \quad \partial_\alpha \boldsymbol{n} = -b_\alpha^\sigma \boldsymbol{a}_\sigma. \tag{4.4}$$

and the covariant derivatives of vector fields and one-forms

$$v^\alpha{}_{|\beta} = v^\alpha{}_{,\beta} + \Gamma_{\beta\sigma}^\alpha v^\sigma, \qquad f_{\alpha|\beta} = f_{\alpha,\beta} - \Gamma_{\alpha\beta}^\sigma f_\sigma. \tag{4.5}$$

The linear Koiter theory is formulated in terms of the infinitesimal displacement field. This vector field over Ω can be described either extrinsically in terms of a Cartesian basis $\{\boldsymbol{e}_i\}$ of $\mathbb{R}^3$, or intrinsically

$$\boldsymbol{U} = U^i \boldsymbol{e}_i = u^\alpha \boldsymbol{a}_\alpha + w \boldsymbol{a}_3, \tag{4.6}$$

where $\boldsymbol{u} = u^\alpha \boldsymbol{a}_\alpha$ and w denote the in-plane and out-of-plane components of the displacement field. We formulate the theory intrinsically. However, because most numerical calculations are based on an extrinsic formulation, we need to connect both formulations, as further detailed in Appendix B. An important relation for this purpose, which follows from a direct calculation using Eq. (4.4), is

$$\partial_\beta \boldsymbol{U} = \partial_\beta U^i \boldsymbol{e}_i = \left(u^\alpha{}_{|\beta} - b^\alpha_\beta w \right) \boldsymbol{a}_\alpha + \left(w_{|\beta} + b_{\alpha\beta} u^\alpha \right) \boldsymbol{n}. \tag{4.7}$$

The strain measures in Koiter's linear thin shell theory are the membrane strain tensor $\varepsilon_{\alpha\beta}$ and bending strain tensor $\rho_{\alpha\beta}$, measuring the infinitesimal changes in metric and in curvature and given by

$$\varepsilon_{\alpha\beta} = \frac{1}{2} \left(u_{\alpha|\beta} + u_{\beta|\alpha} - 2\, b_{\alpha\beta} w \right), \tag{4.8}$$

$$\rho_{\alpha\beta} = w_{|\alpha\beta} - c_{\alpha\beta} w + b^\lambda_\alpha u_{\lambda|\beta} + b^\lambda_\beta u_{\lambda|\alpha} + b^\lambda_{\alpha|\beta} u_\lambda, \tag{4.9}$$

where $c_{\alpha\beta} = b^\lambda_\alpha b_{\lambda\beta}$ is the third fundamental form of the shell middle surface.

The strain energy density per unit area can then be written in terms of these strain measures, $W(\boldsymbol{\varepsilon}, \boldsymbol{\rho})$, which allows us to define the stress resultant and stress couple symmetric tensors

$$n^{\alpha\beta} = \frac{\partial W}{\partial \varepsilon_{\alpha\beta}}, \quad m^{\alpha\beta} = \frac{\partial W}{\partial \rho_{\alpha\beta}}. \tag{4.10}$$

For the sake of simplicity, we neglect external moments on the middle surface of shell, external loads at the shell edges, and consider only external body forces acting on the

middle surface, $\boldsymbol{p} = p^\alpha \boldsymbol{a}_\alpha + p^3 \boldsymbol{n}$. Thus, the external potential energy density $V(\boldsymbol{U})$ is

$$V(\boldsymbol{U}) = -\boldsymbol{p} \cdot \boldsymbol{U}, \tag{4.11}$$

and the total potential energy of the shell takes the form

$$\Pi[\boldsymbol{U}] = \int_\Omega \left[W(\boldsymbol{\varepsilon}, \boldsymbol{\rho}) + V(\boldsymbol{U}) \right] d\Omega = \int_{\bar{\Omega}} \left[W(\boldsymbol{\varepsilon}, \boldsymbol{\rho}) + V(\boldsymbol{U}) \right] \sqrt{a} \, d\bar{\Omega}. \tag{4.12}$$

Making the potential energy stationary with respect to arbitrary admissible variations and integrating by parts, we obtain the in-plane and out-of-plane equilibrium equations

$$- \left(n^{\alpha\beta} + b^\alpha_\lambda m^{\lambda\beta} \right)_{|\beta} - b^\alpha_\lambda m^{\lambda\beta}{}_{|\beta} = p^\alpha \quad \text{in} \quad \Omega, \tag{4.13}$$

$$m^{\alpha\beta}{}_{|\alpha\beta} - c_{\alpha\beta} m^{\alpha\beta} - b_{\alpha\beta} n^{\alpha\beta} = p^3 \quad \text{in} \quad \Omega. \tag{4.14}$$

The natural boundary conditions associated to in-plane equilibrium on the part of the boundary of Ω where displacements are free, γ_n, is

$$\left(n^{\alpha\beta} + 2 b^\alpha_\lambda m^{\lambda\beta} \right) \nu_\beta = 0, \tag{4.15}$$

where $\boldsymbol{\nu}$ is the outer normal to $\partial\Omega$ tangent to Ω. The natural boundary conditions associated to out-of-plane equilibrium can be weakly stated as

$$\int_{\gamma_n} \left(m^{\alpha\beta} \eta_{|\alpha} - m^{\alpha\beta}{}_{|\alpha} \eta \right) \nu_\beta \, d\ell = 0, \tag{4.16}$$

for all admissible variations η. Further manipulation leads to two additional natural boundary conditions on γ_n:

$$m^{\alpha\beta} \nu_\alpha \nu_\beta = 0, \quad \text{and} \quad m^{\alpha\beta}{}_{|\alpha} \nu_\beta + \partial_\tau \left(m^{\alpha\beta} \nu_\alpha \tau_\beta \right) = 0, \tag{4.17}$$

where $\boldsymbol{\tau}$ is tangential to $\partial\Omega$.

For homogeneous and isotropic shells of constant thickness t, the strain energy density can be written as

$$W\left(\boldsymbol{\varepsilon},\boldsymbol{\rho}\right) = \frac{1}{2}\mathbb{C}^{\alpha\beta\rho\lambda}\left(t\varepsilon_{\alpha\beta}\,\varepsilon_{\rho\lambda} + \frac{t^3}{12}\rho_{\alpha\beta}\,\rho_{\rho\lambda}\right),\tag{4.18}$$

with

$$\mathbb{C}^{\alpha\beta\rho\lambda} = \frac{E}{(1-\nu^2)}\left[\nu a^{\alpha\beta}\,a^{\rho\lambda} + \frac{1-\nu}{2}\left(a^{\alpha\rho}\,a^{\beta\lambda} + a^{\alpha\lambda}\,a^{\beta\rho}\right)\right].$$

where E is Young's modulus and ν is Poisson's ratio. The first term is the membrane strain energy density and the second term is the bending strain energy density.

4.3   Derivation of G using configurational forces

4.3.1   Material rearrangement

To analyze fracture in thin shells using the concepts of configurational forces, and recalling Eqs. (4.8,4.9), we write the potential energy density as

$$W\left(\boldsymbol{\varepsilon},\boldsymbol{\rho}\right) + V(\boldsymbol{u}) = \tilde{W}(\xi,\boldsymbol{b},\nabla\boldsymbol{b},\boldsymbol{u},\nabla\boldsymbol{u},w,\nabla^2 w),\tag{4.19}$$

where ξ are the coordinates of the referential domain $\bar{\Omega}$ and ∇ denotes the covariant derivative. The explicit dependence of $\tilde{W}$ on ξ emphasizes the possibly heterogeneous nature of the material, e.g. due to the presence of a defects or microstructure, treated distinctly from the dependence on shape through the second fundamental form. Thus, the total potential energy is written as

$$\Pi[\boldsymbol{u},w] = \int_{\bar{\Omega}} \tilde{W}(\xi,\boldsymbol{b},\nabla\boldsymbol{b},\boldsymbol{u},\nabla\boldsymbol{u},w,\nabla^2 w)\sqrt{a}\,d\bar{\Omega}.\tag{4.20}$$

With the goal of understanding the sensitivity of Π to rearrangements of the microstructure, we define a material rearrangement as a one-parameter family of one-to-one mappings $\Psi_\epsilon : \bar{\Omega} \longrightarrow \bar{\Omega}, \quad \epsilon \geq 0$, satisfying $\Psi_0 = Id$. Its infinitesimal generator, or "velocity of the microstructure", is

$$\boldsymbol{V} = \left.\frac{d\Psi_\epsilon}{d\epsilon}\right|_{\epsilon=0}. \tag{4.21}$$

For crack propagation, $\boldsymbol{V}$ should be tangential to the crack path and ϵ can be rescaled so that $|\boldsymbol{V}_{\text{tip}}| = 1$. A rearrangement induces a one-parameter family of energy functionals

$$\Pi_\epsilon[\boldsymbol{u}, w] = \int_{\bar{\Omega}} \tilde{W}(\Psi_\epsilon^{-1}(\xi), \boldsymbol{b}, \nabla\boldsymbol{b}, \boldsymbol{u}, \nabla\boldsymbol{u}, w, \nabla^2 w)\sqrt{a}\, d\bar{\Omega}, \tag{4.22}$$

whose minimizer is denoted by $(\boldsymbol{u}_\epsilon, w_\epsilon)$. Note carefully that, had we considered the family of functionals

$$\int_{\bar{\Omega}} \tilde{W}(\Psi_\epsilon^{-1}(\xi), \boldsymbol{b}(\Psi_\epsilon^{-1}(\xi)), \nabla\boldsymbol{b}(\Psi_\epsilon^{-1}(\xi)), \boldsymbol{u}, \nabla\boldsymbol{u}, w, \nabla^2 w)\sqrt{a}\, d\bar{\Omega}, \tag{4.23}$$

instead, we would be "moving" both the microstructure and the heterogeneity induced by curvature. Because shape (in the reference configuration) is viewed here as an intrinsic property of the shell, the definition in Eq. (4.22) is the right choice to examine crack propagation past a fixed geometry.

4.3.2 Configurational force field

The energy release rate is defined as (Ortiz, 2004)

$$\begin{aligned} G &= -\left.\frac{d}{d\epsilon}\right|_{\epsilon=0} \Pi_\epsilon[\boldsymbol{u}_\epsilon, w_\epsilon] \\ &= -\left.\frac{d}{d\epsilon}\right|_{\epsilon=0} \int_{\bar{\Omega}} \tilde{W}(\Psi_\epsilon^{-1}(\xi), \boldsymbol{b}, \nabla\boldsymbol{b}, \boldsymbol{u}_\epsilon, \nabla\boldsymbol{u}_\epsilon, w_\epsilon, \nabla^2 w_\epsilon)\sqrt{a}\, d\bar{\Omega}. \end{aligned} \tag{4.24}$$

Because $(\boldsymbol{u}_\epsilon, w_\epsilon)$ satisfies the essential boundary conditions for all ϵ, its derivative with respect to ϵ is an admissible variation, which, together the fact that $(\boldsymbol{u}_\epsilon, w_\epsilon)$ is an equilibrium solution, leads to

$$G = -\int_{\bar{\Omega}} \left(\frac{\partial \tilde{W}}{\partial \xi} \right)_{\text{expl}} \cdot \left. \frac{d\Psi_\epsilon^{-1}}{d\epsilon} \right|_{\epsilon=0} \sqrt{a} \, d\bar{\Omega} = \int_{\bar{\Omega}} \left(\frac{\partial \tilde{W}}{\partial \xi} \right)_{\text{expl}} \cdot \boldsymbol{V} \sqrt{a} \, d\bar{\Omega}, \qquad (4.25)$$

where in writing the last expression we have used the identity

$$\left. \frac{d\Psi_\epsilon(\xi)}{d\epsilon} \right|_{\epsilon=0} + \left. \frac{d\Psi_\epsilon^{-1}(\xi)}{d\epsilon} \right|_{\epsilon=0} = 0, \qquad (4.26)$$

which follows from $\left(\Psi_\epsilon \circ \Psi_\epsilon^{-1} \right)(\xi) = \xi$. Equation (4.25) allows us to identify the configurational force field, or driving force for microstructure rearrangement, as the field being conjugate to the microstructure velocity:

$$J_\gamma = \left(\frac{\partial \tilde{W}}{\partial \xi^\gamma} \right)_{\text{expl}} \qquad (4.27)$$

where the notation emphasizes that the partial derivative is taken with respect to the first argument of $\tilde{W}$, see Eq. (4.19).

4.3.3   Eshelby energy-momentum tensor and non-conservative contributions to the configurational force field

Because the energy density $\tilde{W}$ exhibits position dependence through the second fundamental form, even in the absence of defects we cannot expect a conserved quantity associated to an "explicit" translational symmetry of $\tilde{W}$ invoking Noether's theorem. Consequently, in general J_α will not admit an expression as the divergence of an Eshelby tensor for a curved shell. Here, we wish to identify the Eshelby part and the non-conservative parts of the configurational force field.

As commonly done, we compute the configurational force field introducing the

70

total derivative of $\tilde{W}$ with respect to ξ^γ:

$$J_\gamma = \left(\frac{\partial \tilde{W}}{\partial \xi^\gamma}\right)_{\text{expl}} = \left(\frac{\partial \tilde{W}}{\partial \xi^\gamma}\right)_{\text{total}} - \frac{\partial \tilde{W}}{\partial b_{\alpha\beta}} b_{\alpha\beta|\gamma} - \frac{\partial \tilde{W}}{\partial b_{\alpha\beta|\nu}} b_{\alpha\beta|\nu\gamma} \tag{4.28}$$

$$- \frac{\partial \tilde{W}}{\partial u_\alpha} u_{\alpha|\gamma} - \frac{\partial \tilde{W}}{\partial u_{\alpha|\beta}} u_{\alpha|\beta\gamma} \tag{4.29}$$

$$- \frac{\partial \tilde{W}}{\partial w} w_{|\gamma} - \frac{\partial \tilde{W}}{\partial w_{|\alpha\beta}} w_{|\alpha\beta\gamma}. \tag{4.30}$$

Recalling Eqs. (4.8,4.9) and using the chain rule, we have

$$\frac{\partial \tilde{W}}{\partial b_{\alpha\beta}} = n^{\lambda\mu} \frac{\partial \varepsilon_{\lambda\mu}}{\partial b_{\alpha\beta}} + m^{\lambda\mu} \frac{\partial \rho_{\lambda\mu}}{\partial b_{\alpha\beta}}$$
$$= -n^{\alpha\beta} w - m^{\alpha\mu} b_\mu^\beta w - m^{\beta\mu} b_\mu^\alpha w + m^{\alpha\mu} u^\beta{}_{|\mu} + m^{\beta\mu} u^\alpha{}_{|\mu}, \tag{4.31}$$

and thus

$$\frac{\partial \tilde{W}}{\partial b_{\alpha\beta}} b_{\alpha\beta|\gamma} = \left[- \left(n^{\alpha\beta} + 2m^{\alpha\mu} b_\mu^\beta \right) w + 2m^{\alpha\mu} u^\beta{}_{|\mu} \right] b_{\alpha\beta|\gamma}. \tag{4.32}$$

Similarly,

$$\frac{\partial \tilde{W}}{\partial b_{\alpha\beta|\nu}} = m^{\lambda\mu} \frac{\partial \rho_{\lambda\mu}}{\partial b_{\alpha\beta|\nu}} = \frac{1}{2} m^{\beta\nu} u^\alpha + \frac{1}{2} m^{\alpha\nu} u^\beta, \tag{4.33}$$

and thus

$$\frac{\partial \tilde{W}}{\partial b_{\alpha\beta|\nu}} b_{\alpha\beta|\nu\gamma} = m^{\alpha\nu} u^\beta b_{\alpha\beta|\nu\gamma}. \tag{4.34}$$

Focusing now on Eq. (4.29), we have

$$\frac{\partial \tilde{W}}{\partial u_\alpha} = -p^\alpha + m^{\lambda\mu} b^\alpha_{\lambda|\mu}, \qquad \frac{\partial \tilde{W}}{\partial u_{\alpha|\beta}} = l^{\alpha\beta}. \tag{4.35}$$

71

where

$$l^{\alpha\beta} = n^{\alpha\beta} + 2b^{\alpha}_{\lambda}m^{\lambda\beta} \tag{4.36}$$

is in general a non-symmetric tensor. Thus,

$$\frac{\partial\tilde{W}}{\partial u_{\alpha}}u_{\alpha|\gamma} + \frac{\partial\tilde{W}}{\partial u_{\alpha|\beta}}u_{\alpha|\beta\gamma} = \left(-p^{\alpha} + m^{\lambda\mu}b^{\alpha}_{\lambda|\mu}\right)u_{\alpha|\gamma} + l^{\alpha\beta}u_{\alpha|\beta\gamma}. \tag{4.37}$$

To cast part of this expression in divergence form, we recall that second covariant derivatives do not commute (Flügge, 1972). Instead,

$$u_{\alpha|\beta\gamma} = u_{\alpha|\gamma\beta} + K\left(a_{\alpha\gamma}u_{\beta} - a_{\alpha\beta}u_{\gamma}\right), \tag{4.38}$$

where K is the Gaussian curvature of the shell middle surface. Combining the two equations above, we obtain

$$\begin{aligned}
\frac{\partial\tilde{W}}{\partial u_{\alpha}}u_{\alpha|\gamma} + \frac{\partial\tilde{W}}{\partial u_{\alpha|\beta}}u_{\alpha|\beta\gamma} &= \left(l^{\alpha\beta}u_{\alpha|\gamma}\right)_{|\beta} + K\left(l_{\gamma}{}^{\beta}u_{\beta} - \mathrm{tr}\boldsymbol{l}\,u_{\gamma}\right) \\
&\quad + \left(-l^{\alpha\beta}{}_{|\beta} + m^{\lambda\mu}b^{\alpha}_{\lambda|\mu} - p^{\alpha}\right)u_{\alpha|\gamma}.
\end{aligned} \tag{4.39}$$

Close examination of the last term shows that it vanishes invoking tangential mechanical equilibrium in Eq. (4.13).

We focus now on Eq. (4.30). Direct calculations show that

$$\frac{\partial\tilde{W}}{\partial w} = -p^{3} - n^{\alpha\beta}b_{\alpha\beta} - m^{\alpha\beta}c_{\alpha\beta} = -m^{\alpha\beta}{}_{|\alpha\beta}, \qquad \frac{\partial\tilde{W}}{\partial w_{|\alpha\beta}} = m^{\alpha\beta}, \tag{4.40}$$

where in the last step in the first equation we have used normal mechanical equilibrium in Eq. (4.14). Again because of the non-commutativity of the second covariant

derivative, as have

$$w_{|\alpha\beta\gamma} = w_{|\alpha\gamma\beta} + K\left(a_{\alpha\gamma}w_{|\beta} - a_{\alpha\beta}w_{|\gamma}\right), \tag{4.41}$$

which leads to

$$\frac{\partial\tilde{W}}{\partial w}w_{|\gamma} + \frac{\partial\tilde{W}}{\partial w_{|\alpha\beta}}w_{|\alpha\beta\gamma} = -m^{\alpha\beta}{}_{|\alpha\beta}w_{|\gamma} + m^{\alpha\beta}w_{|\alpha\gamma\beta} + K\left(m^{\beta}_{\gamma}w_{|\beta} - \operatorname{tr}\boldsymbol{m}\,w_{|\gamma}\right)$$
$$= \left(-m^{\alpha\beta}{}_{|\alpha}w_{|\gamma} + m^{\alpha\beta}w_{|\alpha\gamma}\right)_{|\beta} + K\left(m^{\beta}_{\gamma}w_{|\beta} - \operatorname{tr}\boldsymbol{m}\,w_{|\gamma}\right). \tag{4.42}$$

Thus, defining the Eshelby tensor as

$$\boxed{M^{\beta}_{\gamma} = \tilde{W}\delta^{\beta}_{\gamma} - l^{\alpha\beta}u_{\alpha|\gamma} - m^{\alpha\beta}w_{|\alpha\gamma} + m^{\alpha\beta}{}_{|\alpha}w_{|\gamma}}, \tag{4.43}$$

and defining

$$\boxed{\hat{J}_{\gamma} = \operatorname{tr}\boldsymbol{l}\,u_{\gamma} - l^{\beta}_{\gamma}u_{\beta} + \operatorname{tr}\boldsymbol{m}\,w_{|\gamma} - m^{\beta}_{\gamma}w_{|\beta}}, \tag{4.44}$$

and

$$\boxed{\tilde{J}_{\gamma} = \left(l^{\alpha\beta}w - 2m^{\alpha\mu}u^{\beta}{}_{|\mu}\right)b_{\alpha\beta|\gamma} - m^{\alpha\nu}u^{\beta}b_{\alpha\beta|\nu\gamma}}, \tag{4.45}$$

we can express the configurational force field as

$$\boxed{J_{\gamma} = M^{\beta}_{\gamma|\beta} + K\hat{J}_{\gamma} + \tilde{J}_{\gamma}}. \tag{4.46}$$

All terms participating in J_{γ}, except for the first one in Eq. (4.43), have the structure of a stress multiplied by a displacement, possibly affected by covariant derivatives and multiplied by a quantity involving curvature. The first term is conservative (in divergence form) and does not involve curvature. The second embodies the lack of translational symmetry due to the mere presence of Gaussian curvature, even if it is
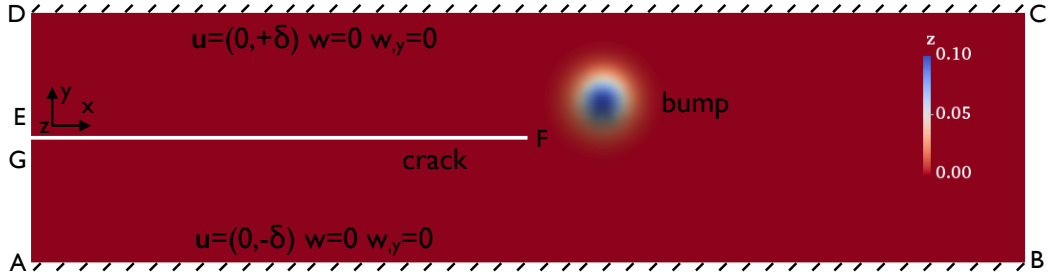
Figure 4.2: Long plate with a pre-crack and a finite shape disturbance, here a bump. The boundaries AB and CD are fully clamped with imposed constant opening displacements, i.e, $\boldsymbol{u}(x, \pm H/2) = (0, \pm\delta), w(x, \pm H/2) = 0, \partial_y w(x, \pm H/2) = 0$. All boundaries including the crack faces are traction-free.

constant. The last term emerges as a result of the non-uniformity of curvature, and would vanish for instance for a spherical shell. We note that for a cylindrical shell, $J_\gamma = M^\beta_{\gamma|\beta}$ consistent with the translational symmetry in this geometry.

4.4 Energy release rate in a plate with a pre-crack and a bump

We examine now a simple shell configuration where the energy release rate can be computed with the results of the previous section. We consider a long plate with a pre-crack and a finite geometric disturbance, such as a bump. We assume that this disturbance is away from the external boundary of the plate defined by $AB \cup BC \cup CD \cup DE \cup GA$, see Figure 4.2. We assume that the plate, except for the bump, lies on the $x - y$ plane and we take this plane as the parametric domain, $\xi = (x, y)$. We consider a Monge parametrization of the shell geometry as $\boldsymbol{\varphi}(x, y) = (x, y, h(x, y))$ for $(x, y) \in \bar{\Omega} = [0, L] \times [-H/2, H/2]$. We consider the one-parameter family of cracks defined by $\mathscr{C} = \{x \in [0, d], y = 0\}$, i.e. cracks whose projection onto the $x - y$ plane lies on the x axis.

In the Monge parametrization, the covariant basis vectors are

$$\boldsymbol{a}_1 = \boldsymbol{e}_1 + \partial_x h(x, y)\boldsymbol{e}_3, \quad \boldsymbol{a}_2 = \boldsymbol{e}_2 + \partial_y h(x, y)\boldsymbol{e}_3. \tag{4.47}$$

The basis vector $\boldsymbol{a}_1$ is tangental to the crack even if $\mathrm{supp}(h) \cap \mathscr{C} \neq \varnothing$. The boundary conditions are shown in Figure 4.2.

To extend infinitesimally the crack towards the right, we need to define an appropriate "velocity of the microstructure" $\boldsymbol{V} = V^1 \boldsymbol{a}_1 + V^2 \boldsymbol{a}_2$, see Eq. (4.21), a tangential velocity field resulting in a rightwards motion of material particles so that the crack tip advances at unit speed. Thus, its components can be obtained by solving the system of equations

$$\begin{cases} \boldsymbol{V} \cdot \boldsymbol{e}_1 = V^1 \boldsymbol{a}_1 \cdot \boldsymbol{e}_1 + V^2 \boldsymbol{a}_2 \cdot \boldsymbol{e}_1 = 1 \\ \boldsymbol{V} \cdot \boldsymbol{e}_2 = V^1 \boldsymbol{a}_1 \cdot \boldsymbol{e}_2 + V^2 \boldsymbol{a}_2 \cdot \boldsymbol{e}_2 = 0 \end{cases}, \tag{4.48}$$

which leads to $\boldsymbol{V} = \boldsymbol{a}_1$. In fact, this choice results in a projected motion of the crack tip at unit speed, but in an actual extension of the crack length at a rate of $\|\boldsymbol{a}_1\|_{\mathrm{tip}} = \sqrt{1 + [\partial_x h(x_{\mathrm{tip}}, y_{\mathrm{tip}})]^2}$. These two speeds coincide if the crack tip is away from the bump. Therefore, we re-define the "velocity of the microstructure" as

$$\boldsymbol{V} = \frac{1}{\|\boldsymbol{a}_1\|_{\mathrm{tip}}} \boldsymbol{a}_1. \tag{4.49}$$

Recalling Eq. (4.25), the energy release rate per unit actual crack length G is then given by

$$G = \int_\Omega J_\gamma V^\gamma \, d\Omega = \underbrace{\int_\Omega M^\beta_{\gamma|\beta} V^\gamma \, d\Omega}_{G_{\mathrm{cons}}} + \underbrace{\int_\Omega K \hat{J}_\gamma V^\gamma \, d\Omega}_{G_K} + \underbrace{\int_\Omega \tilde{J}_\gamma V^\gamma \, d\Omega}_{G_{\boldsymbol{b}}}, \tag{4.50}$$

where G_{cons} stands for the conservative part of the energy release rate expressed in terms of Eshelby's tensor, G_K denotes the contribution arising from the Gaussian

75

curvature, and $G_{\boldsymbol{b}}$ the contribution arising from the explicit dependence of the energy density on the second fundamental form, which involves derivatives of $\boldsymbol{b}$.

In the present setting, because the domain is a curved manifold rather than Euclidean space, $\nabla \boldsymbol{V}$ is not zero in general and consequently even the Eshelby contribution to G involves a domain integral in addition to a contour integral. Indeed, invoking the divergence theorem and the product rule, we have

$$
\begin{aligned}
G_{\text{cons}} &= \int_\Omega \left(M_\gamma^\beta \, V^\gamma \right)_{|\beta} \, d\Omega - \int_\Omega M_\gamma^\beta \, V^\gamma{}_{|\beta} \, d\Omega \\
&= \int_{\partial\Omega} M_\gamma^\beta \, V^\gamma \, \nu_\beta \, d\ell - \int_\Omega M_\gamma^\beta \, V^\gamma{}_{|\beta} \, d\Omega.
\end{aligned}
\tag{4.51}
$$

Thus,

$$
G = \int_{\partial\Omega} M_\gamma^\beta \, V^\gamma \, \nu_\beta \, d\ell - \int_\Omega M_\gamma^\beta \, V_{|\beta}^\gamma \, d\Omega + \int_\Omega K \hat{J}_\gamma \, V^\gamma \, d\Omega + \int_\Omega \tilde{J}_\gamma \, V^\gamma \, d\Omega, \, .
\tag{4.52}
$$

Focusing on the boundary integral and recalling Eq. (4.43), we have

$$
\int_{\partial\Omega} M_\gamma^\beta \, V^\gamma \, \nu_\beta \, d\ell = \underbrace{\int_{\partial\Omega} \tilde{W} V^\gamma \nu_\gamma \, d\ell}_{\text{①}} - \underbrace{\int_{\partial\Omega} l^{\alpha\beta} u_{\alpha|\gamma} V^\gamma \nu_\beta \, d\ell}_{\text{②}}
$$
$$
- \underbrace{\int_{\partial\Omega} \left(m^{\alpha\beta} w_{|\alpha\gamma} V^\gamma - m^{\alpha\beta}{}_{|\alpha} w_{|\gamma} \, V^\gamma \right) \nu_\beta \, d\ell}_{\text{③}},
\tag{4.53}
$$

where $\partial\Omega = AB \cup BC \cup CD \cup DE \cup EF \cup FG \cup GA$. The parts of the boundary aligned with the x axis (AB, CD, EF, FG) do not contribute to ① since there $\boldsymbol{V}$ is perpendicular to $\boldsymbol{\nu}$. Thus, because the bump is away from the outer part of the boundary, we have

$$
\text{①} = \frac{1}{\|\boldsymbol{a}_1\|_{\text{tip}}} \left(\int_{BC} \tilde{W} \, d\ell - \int_{DE} \tilde{W} \, d\ell - \int_{GA} \tilde{W} \, d\ell \right).
\tag{4.54}
$$

76

On AB and CD, the clamped parts of the boundary, $u_{\alpha|\gamma}V^\gamma = 0$ since $\boldsymbol{u}$ is constant along these segments and $\boldsymbol{V}$ is parallel to them. All other parts of the boundary are traction-free and hence do not contribute to ② neither, see Eq. (4.15). Consequently, ② $= 0$.

On AB and CD $w_{|\gamma}V^\gamma = 0$ and $w_{|\alpha\gamma}V^\gamma = 0$ because there $w = 0$, $w_{,y} = w_{|y} = 0$ (the bump is away from the boundary), and $\boldsymbol{V}$ is parallel to these segments. Therefore, these two segments do not contribute to ③. All other parts of the boundary are traction-free, which therefore recalling Eq. (4.55) and taking as a test function $\eta = w_{|\gamma}V^\gamma$, leads to

$$\int_{\partial\Omega\backslash(AB\cup CD)} \left[m^{\alpha\beta}\left(w_{|\alpha\gamma}V^\gamma + w_{|\gamma}V^\gamma{}_{|\alpha}\right) - m^{\alpha\beta}{}_{|\alpha}w_{|\gamma}V^\gamma \right] \nu_\beta\, d\ell = 0, \qquad (4.55)$$

where we have used the fact that $w_{|\alpha\gamma} = w_{|\gamma\alpha}$. Comparing this expression with Eq. (4.53) leads to

$$③ = -\int_{\partial\Omega\backslash(AB\cup CD)} m^{\alpha\beta}w_{|\gamma}V^\gamma{}_{|\alpha}\nu_\beta\, d\ell. \qquad (4.56)$$

Because we have assumed that the bump is away from the outer part of boundary, $\nabla\boldsymbol{V}$ can only be non-zero along the crack when it intersects with the bump. Thus, the boundary contribution to G is

$$
\begin{aligned}
\int_{\partial\Omega} M^\beta_\gamma V^\gamma \nu_\beta\, d\ell ={}& \frac{1}{\|\boldsymbol{a}_1\|_{\text{tip}}} \left(\int_{BC} \tilde{W}\, d\ell - \int_{DE} \tilde{W}\, d\ell - \int_{GA} \tilde{W}\, d\ell \right) \\
&+ \int_{EF\cup FG} m^{\alpha\beta}w_{|\gamma}V^\gamma{}_{|\alpha}\nu_\beta\, d\ell,
\end{aligned}
\qquad (4.57)
$$

where the last terms is non-zero only when $\operatorname{supp}(h) \cap \mathscr{C} \neq \varnothing$.

Consider now for simplicity the case of a very long strip, so that the effect of the bump is negligible on the lateral sides of the plate, the material is fully relaxed on a vertical boundary far away on the left, and uniformly strained ($\varepsilon_{xx} = \varepsilon_{xy} = 0$, $\varepsilon_{yy} = 2\delta/H$) on a vertical boundary far away on the right. Then, the first line in Eq. (4.57)

can be evaluated considering a planar plate under plane stress conditions, obtaining

$$\int_{BC} \tilde{W}\, d\ell - \int_{DE} \tilde{W}\, d\ell - \int_{GA} \tilde{W}\, d\ell = \frac{E}{1-\nu^2}\frac{2\delta^2}{H} = G_{\text{no bump}}. \tag{4.58}$$

In summary, we can express the energy release rate of a plate with a pre-crack and a bump in terms of the energy release rate of a plate without bump as

$$\boxed{G = \frac{1}{\|\boldsymbol{a}_1\|_{\text{tip}}} G_{\text{no bump}} + G_K + G_{\boldsymbol{b}} - \int_{\Omega} M^{\beta}_{\gamma} V^{\gamma}{}_{|\beta}\, d\Omega + \int_{EF\cup FG} m^{\alpha\beta} w_{|\gamma} V^{\gamma}{}_{|\alpha} \nu_{\beta}\, d\ell}, \tag{4.59}$$

where the correction involving $\|\boldsymbol{a}_1\|_{\text{tip}}$ accounts for the difference between projected at actual crack extension when the crack tip lies within $\text{supp}(h)$,

$$G_K = \int_{\Omega} K \hat{J}_{\gamma} V^{\gamma}\, d\Omega \tag{4.60}$$

accounts for the lack of translational symmetry in the presence of Gaussian curvature,

$$G_{\boldsymbol{b}} = \int_{\Omega} \tilde{J}_{\gamma} V^{\gamma}\, d\Omega \tag{4.61}$$

accounts for the non-uniformity of curvature, and the last two terms account for the fact that, for a curved shell, the "velocity of the microstructure" field cannot be made uniform in general.

The contribution $G_{\boldsymbol{b}}$ involves a term with second derivatives of the curvature, hence fourth derivatives of the parametrization of the middle surface, which can be difficult to evaluate numerically. Indeed, substituting Eq. (4.45) into Eq. (4.61), we have

$$G_{\boldsymbol{b}} = \ldots - \int_{\Omega} m^{\alpha\nu} u^{\beta} b_{\alpha\beta|\nu\gamma} V^{\gamma}\, d\Omega. \tag{4.62}$$

However, by integration by parts, we have

$$\int_\Omega m^{\alpha\nu} u^\beta b_{\alpha\beta|\nu\gamma} V^\gamma \, d\Omega = \int_{\partial\Omega} m^{\alpha\nu} u^\beta b_{\alpha\beta|\nu} V^\gamma \nu_\gamma \, d\ell - \int_\Omega \left(m^{\alpha\nu} u^\beta V^\gamma\right)_{|\gamma} b_{\alpha\beta|\nu} \, d\Omega, \quad (4.63)$$

where $\partial\Omega = AB \cup BC \cup CD \cup DE \cup EF \cup FG \cup GA$. The parts of the boundary aligned with the x axis (AB, CD, EF, FG) do not contribute to the boundary integral since there $\boldsymbol{V}$ is perpendicular to the outer normal $\boldsymbol{\nu}$. Furthermore, the bump being away from the outer part of the boundary, we have $b_{\alpha\beta|\nu} = 0$ on BC, DE, GA. Thus, the boundary integral vanishes and we have the alternative expression

$$G_{\boldsymbol{b}} = \ldots + \int_\Omega \left(m^{\alpha\nu} u^\beta V^\gamma\right)_{|\gamma} b_{\alpha\beta|\nu} \, d\Omega. \qquad (4.64)$$

Appendix B presents the connection between the intrinsic formulation given here and an extrinsic formulation. The extrinsic formulation being the basis of finite element calculations, this Appendix provides a practical method to evaluate G computationally.

4.5   Conclusions

We have derived a general expression for the configurational force field on the linear Koiter theory of thin shells accounting for the effect of geometry, see Eq. (4.46). Not surprisingly, this field cannot be fully expressed as the divergence of an Eshelby tensor because of the lack of translational symmetry in the presence of curvature. The configurational force field is found to be the sum of a conservative Eshelby-like contribution, a contribution proportional to the Gaussian curvature, and a contribution accounting for non-uniformity of curvature.

We have used the general expression of the configurational force field to compute the energy release rate associated with crack extension for a plate with a pre-crack and finite a geometric disturbance, only requiring that this disturbance is away from the external boundaries of the plate. Our final expression shows explicitly the corrections

with respect to the standard planar plate case that arise from curvature.

Our results could be used to model brittle fracture in thin shells in general, and to understand the effect of geometry on crack propagation in situations such as that examined in Figure 4.1.

Chapter 5

Conclusions and future directions

5.1 Conclusions

The main contributions of this dissertation are summarized below:

- In Chapter 2, we propose a variational phase-field model for strongly anisotropic fracture, which resorts to the extended Cahn-Hilliard framework proposed in the context of crystal growth. Previous phase-field models for anisotropic fracture were formulated in a framework only allowing for weak anisotropy. We implement numerically our higher-order phase-field model with smooth local maximum entropy approximants in a direct Galerkin method. The numerical results exhibit all the features of strongly anisotropic fracture, and reproduce strikingly well recent experimental observations.

- In Chapter 3, we develop a variational phase-field model and a computational framework for fracture in thin elastic sheets accounting for geometric nonlinearity and adhesion to a substrate. We directly discretize the displacements and phase-field by C^1 continuous subdivision surface finite element method. The simulations remarkably reproduce the crack patterns observed in tearing experiments and are in good agreement with the theoretical results.

- Motivated by simulations with our phase-field model of fracture in this shells, in

Chapter 4, focusing on the linear Koiter thin shell theory, we obtain expressions for the configurational force-field and for the energy release rate of a plate with a pre-crack and a finite shape disturbance. Because of the curvature of the shell middle surface, the configurational force is path-dependent except for shells which have a constant curvature and zero Gaussian curvature.

Taken together, our results show that the regularized variational approach to brittle fracture constitutes a general framework that naturally generalizes to non-trivial situations such as fracture in materials with strongly anisotropic surface energy or fracture in thin elastic sheets.

5.2   Future Directions

This work also identifies a number of future research directions.

Regarding **Chapter 2**, our work is only a first step in the modeling and simulation of strongly anisotropic fracture using phase-field models, and many questions arise. From a theoretical viewpoint, we would like to understand the relation between our proposed model and a sharp-interface model to predict the direction of cracks. We also plan to investigate the energetic penalty for crack bending implicit in the phase-field model, which presumably imposes an energy cost to crack kinking. It is not clear at this point how this contribution depends on the tensors α_{ijkl}, β_{ijkl} and γ_{ijkl} of the ECH framework, and more importantly it is not clear either if such a penalty has a physical meaning.

Another set of interesting questions revolves around the modeling capabilities of the extended Cahn-Hilliard framework, including the symmetries that can be described with such models, or the kinds of angle dependence of $G_c(\theta)$ that can be achieved, also including the tensors α_{ijkl} and β_{ijkl} neglected here. A very simple motivation for this are geological materials, which typically exhibit two-fold strong anisotropy. These tensors in the ECH model could be made dependent on the phase-field, and the surface energy may depend on the form of the dissipation function $f_0(\phi)$. All these extra features in the model introduce further nonlinearity in the equations,

and may require different numerical solution methods. It is also interesting to examine if one can model surface energies such that the polar plot of $1/G_c(\theta)$ exhibits cusps, as one expects in brittle crystals with cleavage planes. Here, we have expanded the local free energy density $f\left(\phi, \nabla\phi, \nabla^2\phi, \dots\right)$ up to fourth order tensors that can only capture anisotropic surface energy with up to cubic symmetry. However, a large class of materials are in the hexagonal crystal system. The hexagonal symmetry in the anisotropic surface energy could be incorporated into the phase-field fracture model by including an expansion of the free energy involving up to sixth-order tensors. The number of non-zero and independent components of these sixth-order tensors and the constraints imposed on them can be determined following the aruguments used in the context of phase-field models for crystal growth/solidification (Nani and Gururajan, 2014). Finally, the extension of our modeling framework to 3D is open.

The computational approach proposed **Chapter 3** could help us examine in detail the hypotheses underlying current theoretical models of thin sheet tearing, as well as explore other parameter regimes where simple models are not available. This tool could also shed light into ways to control the effective fracture toughness or the crack path of thin shell structures using their overall shape or small shape disturbances, as illustrated in Figure 4.1. On a different note, the computational cost associated to phase-field simulations is one of the difficulties to reproduce experimental configurations. Small shell thickness, narrow numerical cracks or small cohesive lengths require very thin meshes. An adaptive mesh refinement algorithm guided by the phase-field or a distributed memory parallel implementation would allow us to reach more easily interesting parameter ranges.

Finally, the results in **Chapter 4** open many new research directions. We could consider simple examples where our expression for G could be easily evaluated, and the effect of curvature on crack propagation compared with experiments. One such example could be that of ring defined by the region between to parallel circles on a sphere with an equatorial segment crack. The expressions obtained could also be tested numerically and compared to phase-field simulations. Close examination of our expressions for concrete examples could bring insight into the relative importance of

the different terms, and possibly provide an understanding of the influence of geometry on crack propagation in simple terms. This understanding could guide the design of new thin objects with optimized fracture behavior.

Appendix to Chapter 2

Rotation of material orientation relative to the sample

For cubic symmetry and centrosymmetric materials, the fourth-rank tensors α_{ijkl}, β_{ijkl} and γ_{ijkl} have the same major and minor symmetries as the anisotropic elastic stiffness tensor. We summarize next how to transform these tensors to a coordinate system that does not coincide with the principal material axes. The basis change formulae for fourth-rank tensors in Voigt notation are not straightforward. Suppose that the components of the fourth-rank tensor are given in basis E, and we want to determine its components in a second basis $\tilde{E}$. The change of basis formula for the tensor expressed as a matrix in Voigt notation $\mathbf{C}$ can be expressed in matrix form as

$$\mathbf{C}^{\tilde{E}} = \mathbf{K}\mathbf{C}^{E}\mathbf{K}^{T}, \qquad (A.1)$$

where $\mathbf{K}$ is a transformation matrix (Ting, 1996). In 3D, when we rotate the material about the third coordinate vector by an angle Θ, the transformation matrix reduces

to

$$\mathbf{K} = \begin{bmatrix} c^2 & s^2 & 0 & 0 & 0 & 2cs \\ s^2 & c^2 & 0 & 0 & 0 & -2cs \\ 0 & 0 & 1 & 0 & 0 & 0 \\ 0 & 0 & 0 & c & -s & 0 \\ 0 & 0 & 0 & s & c & 0 \\ -cs & cs & 0 & 0 & 0 & c^2 - s^2 \end{bmatrix},$$

where $c = \cos \Theta, s = \sin \Theta$. Consequently, in 2D, the transformation matrix for the 3×3 Voigt representation of the fourth-order tensor, see Eq. (2.16) is just

$$\mathbf{K} = \begin{bmatrix} c^2 & s^2 & 2cs \\ s^2 & c^2 & -2cs \\ -cs & cs & c^2 - s^2 \end{bmatrix}.$$

B

Appendix

Appendix to Chapter 4

Calculation of G using an extrinsic shell formulation

In the finite element solution of mechanical equilibrium of a thin shell, the displacement field of shell middle surface is described in terms of Cartesian components U^i, $i = 1, 2, 3$

$$\boldsymbol{U} = U^i \boldsymbol{e}_i = u^\alpha \boldsymbol{a}_\alpha + w \boldsymbol{n}, \tag{B.1}$$

yet the formulation in Chapter 4 is given in terms of the intrinsic or Gaussian components u^α, $\alpha = 1, 2$ and w. In the equation above, the natural basis vectors are computed from the parametrization of the middle surface as $\boldsymbol{a}_\alpha = \boldsymbol{\varphi}_{,\alpha}$. From the relation above we can obtain the intrinsic components from the Cartesian ones as $u_\alpha = \boldsymbol{U} \cdot \boldsymbol{a}_\alpha$ and $w = \boldsymbol{U} \cdot \boldsymbol{n}$.

The membrane and bending strain tensors of the linear Koiter's theory can be computed in terms of Cartesian components as

$$\varepsilon_{\alpha\beta} = \frac{1}{2} \left(\boldsymbol{\varphi}_{,\alpha} \cdot \boldsymbol{U}_{,\beta} + \boldsymbol{\varphi}_{,\beta} \cdot \boldsymbol{U}_{,\alpha} \right), \tag{B.2}$$

$$\rho_{\alpha\beta} = \boldsymbol{n} \cdot \boldsymbol{U}_{,\alpha\beta} - \left[(\boldsymbol{\varphi}_{,\alpha\beta} \times \boldsymbol{\varphi}_{,2}) \cdot \boldsymbol{U}_{,1} + (\boldsymbol{\varphi}_{,1} \times \boldsymbol{\varphi}_{,\alpha\beta}) \cdot \boldsymbol{U}_{,2} \right] / \sqrt{a}$$
$$- \left(\boldsymbol{n} \cdot \boldsymbol{\varphi}_{,\alpha\beta} \right) \left[(\boldsymbol{\varphi}_{,2} \times \boldsymbol{n}) \cdot \boldsymbol{U}_{,1} + (\boldsymbol{n} \times \boldsymbol{\varphi}_{,1}) \cdot \boldsymbol{U}_{,2} \right] / \sqrt{a}, \tag{B.3}$$

which are alternative expressions to the intrinsic expressions in Eqs. (4.8,4.9). See Millán et al. (2011) for a detailed derivation. The first and second fundamental forms can be computed as $a_{\alpha\beta} = \boldsymbol{a}_\alpha \cdot \boldsymbol{a}_\beta$ and

$$b_{\alpha\beta} = \boldsymbol{n} \cdot \frac{\partial^2 \boldsymbol{\varphi}}{\partial \xi^\alpha \xi^\beta}. \tag{B.4}$$

We focus now on the terms in Eqs. (4.43,4.44,4.45) that can not be directly calculated. Recalling Eq. (4.7) and multiplying this equation by $\boldsymbol{a}_\alpha$, the covariant derivative $u_{\alpha|\gamma}$ can be computed as

$$u_{\alpha|\gamma} = \partial_\gamma \boldsymbol{U} \cdot \boldsymbol{a}_\alpha + b_{\alpha\gamma} w, \tag{B.5}$$

and $w_{|\gamma}$ as

$$w_{|\gamma} = \partial_\gamma \boldsymbol{U} \cdot \boldsymbol{n} - b_{\alpha\gamma} u^\alpha. \tag{B.6}$$

The second covariant derivative $w_{|\alpha\gamma}$ can be computed invoking Eq. (4.9) as

$$w_{|\alpha\gamma} = \rho_{\alpha\gamma} + c_{\alpha\gamma} w - b_\alpha^\lambda u_{\lambda|\gamma} - b_\gamma^\lambda u_{\lambda|\alpha} - b_{\alpha|\gamma}^\lambda u_\lambda. \tag{B.7}$$

In this expression, $b_{\alpha|\gamma}^\lambda$ is computed from the definition of the covariant derivative of a second-order tensor

$$b_{\alpha|\gamma}^\lambda = a^{\lambda\mu} b_{\mu\alpha|\gamma} = a^{\lambda\mu} \left(\frac{\partial b_{\mu\alpha}}{\partial \xi^\gamma} - b_{\beta\alpha} \Gamma_{\mu\gamma}^\beta - b_{\mu\beta} \Gamma_{\alpha\gamma}^\beta \right), \tag{B.8}$$

and noting that from Eqs. (4.4,B.4) we have

$$\frac{\partial b_{\mu\alpha}}{\partial \xi^\gamma} = -b_\gamma^\lambda \boldsymbol{a}_\lambda \cdot \frac{\partial^2 \boldsymbol{\varphi}}{\partial \xi^\mu \xi^\alpha} + \boldsymbol{n} \cdot \frac{\partial^3 \boldsymbol{\varphi}}{\partial \xi^\mu \xi^\alpha \xi^\gamma}. \tag{B.9}$$

The term $m^{\alpha\beta}|_\alpha$ is computed as

$$m^{\alpha\beta}|_\alpha = \frac{Eh^3}{12\left(1-\nu^2\right)}\,H^{\alpha\beta\mu\gamma}\rho_{\mu\gamma|\alpha}, \tag{B.10}$$

$$= \frac{Eh^3}{12\left(1-\nu^2\right)}\,H^{\alpha\beta\mu\gamma}\left(\frac{\partial\rho_{\mu\gamma}}{\partial\xi^\alpha} - \rho_{\lambda\gamma}\Gamma^\lambda_{\mu\alpha} - \rho_{\mu\lambda}\Gamma^\lambda_{\gamma\alpha}\right), \tag{B.11}$$

where in writing Eq. (B.10) we have used the fact that the covariant derivative of the first fundamental form vanishes. A direct calculation shows that

$$\frac{\partial\rho_{\mu\gamma}}{\partial\xi^\alpha} = \boldsymbol{n}_{,\alpha}\cdot\ \boldsymbol{U}_{,\mu\gamma} + \boldsymbol{n}\cdot\ \boldsymbol{U}_{,\mu\gamma\alpha} - A_\alpha\left(B_{\mu\gamma} + B_{\mu\gamma}\right) - \left(B_{\mu\gamma,\alpha} + C_{\mu\gamma,\alpha}\right)/\sqrt{a}, \tag{B.12}$$

where

$$A_\alpha = \partial_\alpha(1/\sqrt{a}) = \left(\boldsymbol{\varphi}_{,1\alpha}\times\boldsymbol{\varphi}_{,2} + \boldsymbol{\varphi}_{,1}\times\boldsymbol{\varphi}_{,2\alpha}\right)\cdot\boldsymbol{n}\,, \tag{B.13}$$

$$\boldsymbol{n}_{,\alpha} = \left(\boldsymbol{\varphi}_{,1\alpha}\times\boldsymbol{\varphi}_{,2} + \boldsymbol{\varphi}_{,1}\times\boldsymbol{\varphi}_{,2\alpha}\right)/\sqrt{a} - \left(A_\alpha/\sqrt{a}\right)\boldsymbol{n}\,, \tag{B.14}$$

$$B_{\mu\gamma} = \left(\boldsymbol{\varphi}_{,\mu\gamma}\times\boldsymbol{\varphi}_{,2}\right)\cdot\boldsymbol{U}_{,1} + \left(\boldsymbol{\varphi}_{,1}\times\boldsymbol{\varphi}_{,\mu\gamma}\right)\cdot\boldsymbol{U}_{,2}\,, \tag{B.15}$$

$$C_{\mu\gamma} = \left(\boldsymbol{n}\cdot\boldsymbol{\varphi}_{,\mu\gamma}\right)\left[\left(\boldsymbol{\varphi}_{,2}\times\boldsymbol{n}\right)\cdot\boldsymbol{U}_{,1} + \left(\boldsymbol{n}\times\boldsymbol{\varphi}_{,1}\right)\cdot\boldsymbol{U}_{,2}\right]\,, \tag{B.16}$$

$$B_{\mu\gamma,\alpha} = \left(\boldsymbol{\varphi}_{,\mu\gamma\alpha}\times\boldsymbol{\varphi}_{,2}\right)\cdot\boldsymbol{U}_{,1} + \left(\boldsymbol{\varphi}_{,1\alpha}\times\boldsymbol{\varphi}_{,\mu\gamma}\right)\cdot\boldsymbol{U}_{,2} + \left(\boldsymbol{\varphi}_{,\mu\gamma}\times\boldsymbol{\varphi}_{,2\alpha}\right)\cdot\boldsymbol{U}_{,1}$$
$$+ \left(\boldsymbol{\varphi}_{,1}\times\boldsymbol{\varphi}_{,\mu\gamma\alpha}\right)\cdot\boldsymbol{U}_{,2} + \left(\boldsymbol{\varphi}_{,\mu\gamma}\times\boldsymbol{\varphi}_{,2}\right)\cdot\boldsymbol{U}_{,1\alpha} + \left(\boldsymbol{\varphi}_{,1}\times\boldsymbol{\varphi}_{,\mu\gamma}\right)\cdot\boldsymbol{U}_{,2\alpha}\,, \tag{B.17}$$

$$C_{\mu\gamma,\alpha} = \left(\boldsymbol{n}_{,\alpha}\cdot\boldsymbol{\varphi}_{,\mu\gamma} + \boldsymbol{n}\cdot\boldsymbol{\varphi}_{,\mu\gamma\alpha}\right)\left[\left(\boldsymbol{\varphi}_{,2}\times\boldsymbol{n}\right)\cdot\boldsymbol{U}_{,1} + \left(\boldsymbol{n}\times\boldsymbol{\varphi}_{,1}\right)\cdot\boldsymbol{U}_{,2}\right]$$
$$+ \left(\boldsymbol{n}\cdot\boldsymbol{\varphi}_{,\mu\gamma}\right)\left[\left(\boldsymbol{\varphi}_{,2\alpha}\times\boldsymbol{n}\right)\cdot\boldsymbol{U}_{,1} + \left(\boldsymbol{n}_{,\alpha}\times\boldsymbol{\varphi}_{,1}\right)\cdot\boldsymbol{U}_{,2}\right]$$
$$+ \left(\boldsymbol{n}\cdot\boldsymbol{\varphi}_{,\mu\gamma}\right)\left[\left(\boldsymbol{\varphi}_{,2}\times\boldsymbol{n}_{,\alpha}\right)\cdot\boldsymbol{U}_{,1} + \left(\boldsymbol{n}\times\boldsymbol{\varphi}_{,1\alpha}\right)\cdot\boldsymbol{U}_{,2}\right]$$
$$+ \left(\boldsymbol{n}\cdot\boldsymbol{\varphi}_{,\mu\gamma}\right)\left[\left(\boldsymbol{\varphi}_{,2}\times\boldsymbol{n}\right)\cdot\boldsymbol{U}_{,1\alpha} + \left(\boldsymbol{n}\times\boldsymbol{\varphi}_{,1}\right)\cdot\boldsymbol{U}_{,2\alpha}\right]. \tag{B.18}$$

Bibliography

A. Abdollahi and I. Arias. Phase-field modeling of crack propagation in piezoelectric and ferroelectric materials with different electromechanical crack conditions. *Journal of the Mechanics and Physics of Solids*, 60(12):2100–2126, 2012.

T. A. Abinandanan and F. Haider. An extended Cahn-Hilliard model for interfaces with cubic anisotropy. *Philosophical Magazine A*, 81(10):2457–2479, 2001.

M. Amestoy and J. B. Leblond. Crack paths in plane situations-II. detailed form of the expansion of the stress intensity factors. *International Journal of Solids and Structures*, 29(4):465–501, 1992.

F. Amiri, D. Millán, Y.X. Shen, T. Rabczuk, and M. Arroyo. Phase-field modeling of fracture in linear thin shells. *Theoretical and Applied Fracture Mechanics*, 69: 102–109, 2014.

F. Amiri, M. Arroyo, D. Millán, M. Silani, and T. Rabczuk. Fourth order phase-field model for local max-ent approximants applied to crack propagation. Under Review, 2015.

T. L. Anderson. *Fracture mechanics: fundamentals and applications*. CRC press, 2005.

I.S. Aranson, V.A. Kalatsky, and V.M. Vinokur. Continuum field description of crack propagation. *Physical Review Letters*, 85(1):118, 2000.

A. S. Argon and Y. Qiao. Cleavage cracking resistance of large-angle grain boundaries in Fe-3 wt% Si alloy. *Philosophical Magazine A*, 82(17-18):3333–3347, 2002.

M. Arroyo and M. Ortiz. Local maximum-entropy approximation schemes: a seamless bridge between finite elements and meshfree methods. *International Journal for Numerical Methods in Engineering*, 65(13):2167–2202, 2006.

A. Azhdari, S. Nemat-Nasser, and J. Rome. Experimental observations and computational modeling of fracturing in an anisotropic brittle crystal (sapphire). *International Journal of Fracture*, 94(3):251–266, 1998.

A.A. L. Baldelli, J.F. Babadjian, B. Bourdin, D. Henao, and C. Maurini. A variational model for fracture and debonding of thin films under in-plane loadings. *Journal of the Mechanics and Physics of Solids*, 70:320–348, 2014.

A.A.L. Baldelli, B. Bourdin, J.J. Marigo, and C. Maurini. Fracture and debonding of a thin film on a stiff substrate: analytical and numerical solutions of a one-dimensional variational model. *Continuum Mechanics and Thermodynamics*, 25 (2-4):243–268, 2013.

D. M. Barnett and R. J. Asaro. The fracture mechanics of slit-like cracks in anisotropic elastic media. *Journal of the Mechanics and Physics of Solids*, 20(6):353–366, 1972.

E. Bayart, A. Boudaoud, and M. Adda-Bedia. On the tearing of thin sheets. *Engineering Fracture Mechanics*, 77(11):1849–1856, 2010.

E. Bayart, A. Boudaoud, and M. Adda-Bedia. Finite-distance singularities in the tearing of thin sheets. *Physical Review Letters*, 106(19):194301, 2011.

M. J. Borden. *Isogeometric analysis of phase-field models for dynamic brittle and ductile fracture*. PhD thesis, Computational Science, Engineering, and Mathematics, University of Texas at Austin, Austin, USA, Aug 2012.

M. J. Borden, T. J. R. Hughes, C. M. Landis, and C. V. Verhoosel. A higher-order phase-field model for brittle fracture: Formulation and analysis within the isogeometric analysis framework. *Computer Methods in Applied Mechanics and Engineering*, 273:100–118, 2014.

M.J. Borden, C.V. Verhoosel, M. A. Scott, T.J.R. Hughes, and C.M. Landis. A phase-field description of dynamic brittle fracture. *Computer Methods in Applied Mechanics and Engineering*, 217:77–95, 2012.

B. Bourdin. Numerical implementation of the variational formulation for quasi-static brittle fracture. *Interfaces and Free Boundaries*, 9(3):411–430, 2007.

B. Bourdin, G. A. Francfort, and J. J. Marigo. Numerical experiments in revisited brittle fracture. *Journal of the Mechanics and Physics of Solids*, 48(4):797–826, 2000.

B. Bourdin, G. A. Francfort, and J. J. Marigo. The variational approach to fracture. *Journal of Elasticity*, 91(1-3):5–148, 2008.

B. Bourdin, C. J. Larsen, and C. L. Richardson. A time-discrete model for dynamic fracture based on crack regularization. *International Journal of Fracture*, 168(2): 133–143, 2011.

B. Bourdin, J.J. Marigo, C. Maurini, and P. Sicsic. Morphogenesis and propagation of complex cracks induced by thermal shocks. *Physical Review Letters*, 112(1):014301, 2014.

A. Braides. *Approximation of free-discontinuity problems*. Springer, Berlin, 1998.

F. Brau. Tearing of thin sheets: Cracks interacting through an elastic ridge. *Physical Review E*, 90(6):062406, 2014.

J. W. Cahn and J. E. Hilliard. Free energy of a nonuniform system. I: Interfacial free energy. *The Journal of Chemical Physics*, 28(2):258–267, 1958.

F. Cazes and N. Moës. Comparison of a phase-field model and of a thick level set model for brittle and quasi-brittle fracture. *International Journal for Numerical Methods in Engineering*, 103(2):114–143, 2015.

A. Chambolle, G. A. Francfort, and J. J Marigo. When and how do cracks propagate? *Journal of the Mechanics and Physics of Solids*, 57(9):1614–1622, 2009.

D. Chapelle and K.J. Bathe. *The finite element analysis of shells-Fundamentals*. Springer Science & Business Media, 2010.

G. P. Cherepanov. *Mechanics of brittle fracture*. Mcgraw-Hill College, 1979.

G.P. Cherepanov. The propagation of cracks in a continuous medium. *Journal of Applied Mathematics and Mechanics*, 31(3):503–512, 1967.

P. G. Ciarlet. *Mathematical elasticity: theory of shells*. Elsevier, North-Holland, 2000.

P. G. Ciarlet. An introduction to differential geometry with applications to elasticity. *Journal of Elasticity*, 78(1-3):1–215, 2005.

F. Cirak and Q. Long. Subdivision shells with exact boundary control and non-manifold geometry. *International Journal for Numerical Methods in Engineering*, 88(9):897–923, 2011.

F. Cirak and M. Ortiz. Fully C^1-conforming subdivision elements for finite deformation thin-shell analysis. *International Journal for Numerical Methods in Engineering*, 51(7):813–833, 2001.

F. Cirak, M. Ortiz, and P. Schroder. Subdivision surfaces: a new paradigm for thin-shell finite-element analysis. *International Journal for Numerical Methods in Engineering*, 47(12):2039–2072, 2000.

Y. Cohen and I. Procaccia. Dynamics of cracks in torn thin sheets. *Physical Review E*, 81(6):066103, 2010.

F. Corson, M. Adda-Bedia, H. Henry, and E. Katzav. Thermal fracture as a framework for quasi-static crack propagation. *International Journal of Fracture*, 158(1):1–14, 2009.

B. Cotterell. On brittle fracture paths. *International Journal of Fracture Mechanics*, 1(2):96–103, 1965.

R. D. Deegan. Finessing the fracture energy barrier in ballistic seed dispersal. *Proceedings of the National Academy of Sciences*, 109(14):5166–5169, 2012.

M.P. Do Carmo. *Differential geometry of curves and surfaces*, volume 2. Prentice-Hall, 1976.

F. A. Donath. Experimental study of shear failure in anisotropic rocks. *Geological Society of America Bulletin*, 72(6):985–989, 1961.

D. S. Dugdale. Yielding of steel sheets containing slits. *Journal of the Mechanics and Physics of Solids*, 8(2):100–104, 1960.

G. Duveau, J. F. Shao, and J. P. Henry. Assessment of some failure criteria for strongly anisotropic geomaterials. *Mechanics of Cohesive-frictional Materials*, 3 (1):1–26, 1998.

L. O. Eastgate, J. P. Sethna, M. Rauscher, T. Cretegny, C. S. Chen, and C. R. Myers. Fracture in mode I using a conserved phase-field model. *Physical Review E*, 65(3): 036117, 2002.

J. J. Eggleston, G. B. McFadden, and P. W. Voorhees. A phase-field model for highly anisotropic interfacial energy. *Physica D: Nonlinear Phenomena*, 150(1):91–103, 2001.

J.W. Eischen and G. Herrmann. Energy release rates and related balance laws in linear elastic defect mechanics. *Journal of Applied Mechanics*, 54(2):388–392, 1987.

F. Erdogan and G. C. Sih. On the crack extension in plates under plane loading and transverse shear. *Journal of Basic Engineering*, 85:519–525, 1963.

W. Flügge. *Tensor analysis and continuum mechanics*. Springer-Verlag, Berlin, 1972.

E.S. Folias. On the effect of initial curvature on cracked flat sheets. *International Journal of Fracture Mechanics*, 5(4):327–346, 1969.

E.S. Folias. On the theory of fracture of curved sheets. *Engineering fracture mechanics*, 2(2):151–164, 1970.

E.S. Folias. Asymptotic approximations to crack problems in shells. In *Plates and shells with cracks*, pages 117–160. Springer, 1977.

G. A. Francfort and J. J. Marigo. Revisiting brittle fracture as an energy minimization problem. *Journal of the Mechanics and Physics of Solids*, 46(8):1319–1342, 1998.

L. B. Freund. *Dynamic fracture mechanics*. Cambridge University Press, Cambridge, 1998.

L.B. Freund. Energy flux into the tip of an extending crack in an elastic solid. *Journal of Elasticity*, 2(4):341–349, 1972.

H. J. Gao and C. H. Chiu. Slightly curved or kinked cracks in anisotropic elastic solids. *International Journal of Solids and Structures*, 29(8):947–972, 1992.

R. V. Goldstein and R. L. Salganik. Brittle fracture of solids with arbitrary cracks. *International Journal of Fracture*, 10(4):507–523, 1974.

A. A. Griffith. The phenomena of rupture and flow in solids. *Philosophical Transactions of the Royal Society of London. Series A, Containing Papers of a Mathematical or Physical Character*, 221(582-593):163–198, 1921.

M. E. Gurtin. On the energy release rate in quasi-static elastic crack propagation. *Journal of Elasticity*, 9(2):187–195, 1979.

M. E. Gurtin. *Configurational Forces as Basic Concepts of Continuum Physics*. Springer Science & Business Media, 2000.

M. E. Gurtin and P. Podio-Guidugli. Configurational forces and the basic laws for crack propagation. *Journal of the Mechanics and Physics of Solids*, 44(6):905–927, 1996.

M. E. Gurtin and P. Podio-Guidugli. Configurational forces and a constitutive theory for crack propagation that allows for kinking and curving. *Journal of the Mechanics and Physics of Solids*, 46(8):1343–1378, 1998.

V. Hakim and A. Karma. Crack path prediction in anisotropic brittle materials. *Physical Review Letters*, 95(23):235501, 2005.

V. Hakim and A. Karma. Laws of crack motion and phase-field models of fracture. *Journal of the Mechanics and Physics of Solids*, 57(2):342–368, 2009.

E. Hamm, P. Reis, M. LeBlanc, B. Roman, and E. Cerda. Tearing as a test for mechanical characterization of thin adhesive films. *Nature Materials*, 7(5):386–390, 2008.

H. Henry and H. Levine. Dynamic instabilities of fracture under biaxial strain using a phase field model. *Physical Review Letters*, 93(10):105504, 2004.

C. Herring. Some theorems on the free energies of crystal surfaces. *Physical Review*, 82(1):87, 1951.

K. Huang. *Lectures on statistical physics and protein folding*. World Scientific, Singapore, 2005.

C.Y. Hui and A.T. Zehnder. A theory for the fracture of thin plates subjected to bending and twisting moments. *International Journal of Fracture*, 61(3):211–229, 1993.

C.Y. Hui, A.T. Zehnder, and Y.K. Potdar. Williams meets von karman: Mode coupling and nonlinearity in the fracture of thin plates. *International journal of fracture*, 93(1-4):409–429, 1998.

A.R. Ingraffea and V. Saouma. Numerical modeling of discrete crack propagation in reinforced and plain concrete. In *Fracture mechanics of concrete: structural application and numerical calculation*, pages 171–225. Springer, 1985.

G. R. Irwin. Analysis of stresses and strains near the end of a crack traversing a plate. *Journal of Applied Mechanics*, 24(79):361–364, 1957.

A. Karma and A. E. Lobkovsky. Unsteady crack motion and branching in a phase-field model of brittle fracture. *Physical Review Letters*, 92(24):245510, 2004.

A. Karma, D. A. Kessler, and H. Levine. Phase-field model of mode III dynamic fracture. *Physical Review Letters*, 87(4):045501, 2001.

A. A. Khan and J. F. V. Vincent. Anisotropy in the fracture properties of apple flesh as investigated by crack-opening tests. *Journal of Materials Science*, 28(1):45–51, 1993.

R. Kienzler and G. Herrmann. *Mechanics in material space: with applications to defect and fracture mechanics*. Springer Science & Business Media, 2000.

R. Kobayashi. Modeling and numerical simulations of dendritic crystal growth. *Physica D: Nonlinear Phenomena*, 63(3):410–423, 1993.

O. Kruglova, F. Brau, D. Villers, and P. Damman. How geometry controls the tearing of adhesive thin films on curved surfaces. *Physical Review Letters*, 107(16):164303, 2011.

C. Kuhn and R. Müller. A continuum phase field model for fracture. *Engineering Fracture Mechanics*, 77(18):3625–3634, 2010.

M. Kuna. *Finite Elements in Fracture Mechanics: Theory-Numerics-Applications*, volume 201. Springer Science & Business Media, 2013.

B. Li, C. Peco, D. Millán, I. Arias, and M. Arroyo. Phase-field modeling and simulation of fracture in brittle materials with strongly anisotropic surface energy. *International Journal for Numerical Methods in Engineering*, 102(3-4):711–727, 2015.

V.I. Marconi and E.A. Jagla. Diffuse interface approach to brittle fracture. *Physical Review E*, 71(3):036110, 2005.

M. Marder. Cracks cleave crystals. *EPL (Europhysics Letters)*, 66(3):364, 2004.

J. Marsden and T. J. R. Hughes. *Mathematical foundations of elasticity*. Dover Publications, Inc., New York, USA, 1983.

C. Maurini, B. Bourdin, G. Gauthier, and V. Lazarus. Crack patterns obtained by unidirectional drying of a colloidal suspension in a capillary tube: experiments and numerical simulations using a two-dimensional variational approach. *International Journal of Fracture*, 1(184):75–91, 2013.

I. M. McKenna, M. P. Gururajan, and P. W. Voorhees. Phase field modeling of grain growth: effect of boundary thickness, triple junctions, misorientation, and anisotropy. *Journal of Materials Science*, 44(9):2206–2217, 2009.

A. Mesgarnejad, B. Bourdin, and M.M. Khonsari. A variational approach to the fracture of brittle thin films subject to out-of-plane loading. *Journal of the Mechanics and Physics of Solids*, 61(11):2360–2379, 2013.

C. Miehe and L.M. Schänzel. Phase field modeling of fracture in rubbery polymers. part I: Finite elasticity coupled with brittle failure. *Journal of the Mechanics and Physics of Solids*, 65:93–113, 2014.

C. Miehe, M. Hofacker, and F. Welschinger. A phase field model for rate-independent crack propagation: Robust algorithmic implementation based on operator splits. *Computer Methods in Applied Mechanics and Engineering*, 199(45):2765–2778, 2010a.

C. Miehe, F. Welschinger, and M. Hofacker. Thermodynamically consistent phase-field models of fracture: Variational principles and multi-field FE implementations. *International Journal for Numerical Methods in Engineering*, 83(10):1273–1311, 2010b.

D. Millán, A. Rosolen, and M. Arroyo. Thin shell analysis from scattered points with maximum-entropy approximants. *International Journal for Numerical Methods in Engineering*, 85(6):723–751, 2011.

D. Millán, A. Rosolen, and M. Arroyo. Nonlinear manifold learning for meshfree finite deformations thin shell analysis. *International Journal for Numerical Methods in Engineering*, 93(7):685–713, 2013.

N. Moës, J. Dolbow, and T. Belytschko. A finite element method for crack growth without remeshing. *International Journal for Numerical Methods in Engineering*, 46(1):131–150, 1999.

P. Müller and J. J. Métois. Anisotropy of the surface thermodynamic properties of silicon. *Thin Solid Films*, 517(1):65–68, 2008.

E.S. Nani and M.P. Gururajan. On the incorporation of cubic and hexagonal interfacial energy anisotropy in phase field models using higher order tensor terms. *Philosophical Magazine*, 94(29), 2014.

M. H. B. Nasseri and B. Mohanty. Fracture toughness anisotropy in granitic rocks. *International Journal of Rock Mechanics and Mining Sciences*, 45(2):167–193, 2008.

H. Niandou, J. F. Shao, J. P. Henry, and D. Fourmaintraux. Laboratory investigation of the mechanical behaviour of tournemire shale. *International Journal of Rock Mechanics and Mining Sciences*, 34(1):3–16, 1997.

M. Ortiz. Continuum mechanics. Lecture notes, 2004.

K. Palaniswamy and W. G. Knauss. On the problem of crack extension in brittle solids under general loading. In S. Nemat-Nasser, editor, *Mechanics Today*, volume 4, pages 87–184. Pergamon Press, 1978.

C. Peco, A. Rosolen, and M. Arroyo. An adaptive meshfree method for phase-field models of biomembranes. Part II: a Lagrangian approach for membranes in viscous fluids. *Journal of Computational Physics*, 249:320–336, 2013.

R. Pérez and P. Gumbsch. Directional anisotropy in the cleavage fracture of silicon. *Physical Review Letters*, 84(23):5347, 2000.

K. Pham and J. J. Marigo. From the onset of damage to rupture: construction of responses with damage localization for a general class of gradient damage models. *Continuum Mechanics and Thermodynamics*, 25(2-4):147–171, 2013.

K. Pham, H. Amor, J. J. Marigo, and C. Maurini. Gradient damage models and their use to approximate brittle fracture. *International Journal of Damage Mechanics*, 20(4):618–652, 2011.

A. J. Pons and A. Karma. Helical crack-front instability in mixed-mode fracture. *Nature*, 464(7285):85–89, 2010.

R. Rangarajan, M. M. Chiaramonte, M. J. Hunsweck, Y.X. Shen, and A. J. Lew. Simulating curvilinear crack propagation in two dimensions with universal meshes. *International Journal for Numerical Methods in Engineering*, 102(3-4):632–670, 2015.

J. R. Rice. A path independent integral and the approximate analysis of strain concentration by notches and cracks. *Journal of Applied Mechanics*, 35(2):379–386, 1968.

J. Riedle, P. Gumbsch, and H. F. Fischmeister. Cleavage anisotropy in tungsten single crystals. *Physical Review Letters*, 76(19):3594, 1996.

B. Roman. Fracture path in brittle thin sheets: a unifying review on tearing. *International Journal of Fracture*, 182(2):209–237, 2013.

V. Romero, B. Roman, E. Hamm, and E. Cerda. Spiral tearing of thin films. *Soft Matter*, 9(34):8282–8288, 2013.

A. Rosolen and M. Arroyo. Blending isogeometric analysis and local maximum entropy meshfree approximants. *Computer Methods in Applied Mechanics and Engineering*, 264:95–107, 2013.

A. Rosolen, D. Millán, and M. Arroyo. On the optimum support size in meshfree methods: a variational adaptivity approach with maximum entropy approximants. *International Journal for Numerical Methods in Engineering*, 82(7):868–895, 2010.

A. Rosolen, D. Millán, and M. Arroyo. Second order convex *maximum entropy* approximants with applications to high order PDE. *International Journal for Numerical Methods in Engineering*, 94(2):150–182, 2013a.

A. Rosolen, C. Peco, and M. Arroyo. An adaptive meshfree method for phase-field models of biomembranes. Part I: approximation with maximum-entropy approximants. *Journal of Computational Physics*, 249:303–319, 2013b.

M. A. Scott, X. Li, T. W. Sederberg, and T. J. R. Hughes. Local refinement of analysis-suitable T-splines. *Computer Methods in Applied Mechanics and Engineering*, 213–216:206–222, 2012.

R. F. Sekerka. Analytical criteria for missing orientations on three-dimensional equilibrium shapes. *Journal of Crystal Growth*, 275(1):77–82, 2005.

D. Sen, K. S. Novoselov, P. M Reis, and M. J. Buehler. Tearing graphene sheets from adhesive substrates produces tapered nanoribbons. *Small*, 6(10):1108–1116, 2010.

P. Sicsic, J.J. Marigo, and C. Maurini. Initiation of a periodic array of cracks in the thermal shock problem: a gradient damage modeling. *Journal of the Mechanics and Physics of Solids*, 63:256–284, 2014.

G. C. Sih. Strain-energy-density factor applied to mixed mode crack problems. *International Journal of Fracture*, 10(3):305–321, 1974.

G.C. Sih, P.C. Paris, and F. Erdogan. Crack-tip, stress-intensity factors for plane extension and plate bending problems. *Journal of Applied Mechanics*, 29(2):306–312, 1962.

R. Spatschek, M. Hartmann, E. Brener, H. Müller-Krumbhaar, and K. Kassner. Phase field modeling of fast crack propagation. *Physical Review Letters*, 96(1):015502, 2006.

A.N. Stroh. Dislocations and cracks in anisotropic elasticity. *Philosophical Magazine*, 3(30):625–646, 1958.

A. Takei, B. Roman, J. Bico, E. Hamm, and F. Melo. Forbidden directions for the fracture of thin anisotropic sheets: An analogy with the wulff plot. *Physical Review Letters*, 110:144301, 2013.

E. Tamayo-Mas and A. Rodríguez-Ferran. A medial-axis-based model for propagating cracks in a regularised bulk. *International Journal for Numerical Methods in Engineering*, 101(7):489–520, 2015.

J.E. Taylor and J.W. Cahn. Diffuse interfaces with sharp corners and facets: Phase field models with strongly anisotropic surfaces. *Physica D: Nonlinear Phenomena*, 112(3):381–411, 1998.

T. C. T. Ting. *Anisotropic Elasticity: Theory and Applications*. Oxford University Press, New York, 1996.

S. Torabi and J. Lowengrub. Simulating interfacial anisotropy in thin-film growth using an extended Cahn-Hilliard model. *Physical Review E*, 85(4):041603, 2012.

S. Torabi, J. Lowengrub, A. Voigt, and S. Wise. A new phase-field model for strongly anisotropic systems. *Proceedings of the Royal Society A: Mathematical, Physical and Engineering Science*, 465(2105):1337–1359, 2009.

A.V. Vuong, C. Giannelli, B. Jüttler, and B. Simeon. A hierarchical approach to adaptive local refinement in isogeometric analysis. *Computer Methods in Applied Mechanics and Engineering*, 200(49–52):3554–3567, 2011.

W. Wang, Y. Zhang, L. Liu, and T. J. R. Hughes. Trivariate solid t-spline construction from boundary triangulations with arbitrary genus topology. *Computer-Aided Design*, 45(2):351–360, 2013.

M.F. Wheeler, T. Wick, and W. Wollner. An augmented-lagrangian method for the phase-field approach for pressurized fractures. *Computer Methods in Applied Mechanics and Engineering*, 271:69–85, 2014.

M.L. Williams. The bending stress distribution at the base of a stationary crack. *Journal of Applied Mechanics*, 28(1):78–82, 1961.

T.A. Witten. Stress focusing in elastic sheets. *Reviews of Modern Physics*, 79(2):643, 2007.

C. C. M. Wu, K. R. McKinney, and R. W. Rice. Zig-zag crack propagation in $MgAl_2O_4$ crystals. *Journal of Materials Science Letters*, 14(7):474–477, 1995.

C. W. Wu. Maximum-energy-release-rate criterion applied to a tension-compression specimen with crack. *Journal of Elasticity*, 8(2):235–257, 1978.

X. P. Xu and A. Needleman. Numerical simulations of fast crack growth in brittle solids. *Journal of the Mechanics and Physics of Solids*, 42(9):1397–1434, 1994.

A.T. Zehnder. *Fracture Mechanics (Lecture Notes in Applied and Computational Mechanics)*. Springer, London, 2012.

A.T. Zehnder and M. J. Viz. Fracture mechanics of thin plates and shells under combined membrane, bending, and twisting loads. *Applied Mechanics Reviews*, 58 (1):37–48, 2005.

T. Zhang, X.Y. Li, and H.J. Gao. Designing graphene structures with controlled distributions of topological defects: A case study of toughness enhancement in graphene ruga. *Extreme Mechanics Letters*, 1:3–8, 2014.